METAL ION BINDING STRUCTURES IN A LARGE AND A SMALL RIBOZYME

DISSERTATION
zur Erlangung der
naturwissenschaftlichen Doktorwürde
(Dr. sc. nat.)

vorgelegt der
Mathematisch-naturwissenschaftlichen Fakultät
der
Universität Zürich

von

MIRIAM SKILANDAT
aus
Deutschland

Promotionskomitee:
Prof. Dr. Roland K. O. Sigel (Vorsitz und Leitung der Dissertation)
Prof. Dr. Nathan W. Luedtke
Prof. Dr. Roland Riek

Zürich, 2014

Acknowledgement

First and foremost, I would like to thank my supervisor, Prof. Dr. Roland Sigel, for giving me the opportunity to work on two fascinating and challenging projects in his group. I am grateful for the support and confidence and for being allowed to work in my own way.

The helpful advice and suggestions of my thesis committee members, Prof. Dr. Nathan Luedtke and Prof. Dr. Roland Riek, were greatly appreciated.

My sincere thanks goes to the subgroup leaders of the Sigel lab, Daniela Donghi, Silke Johannsen, Sofia Gallo, Danny Kowerko and Richard Börner, for constant advice and guidance and for their daily efforts to prevent the lab from plunging into chaos.

I have to thank especially Maria Pechlaner, who answered my numerous questions on NMR, structure calculations and Linux with superhuman patience. Moreover, with her independent way of working and scientific rigor, she was a role model for me as a junior PhD.

I am very grateful to Magda Rowińska-Żyrek for taking on the CPEB3 project with me. Her dedication and persistence made our achievements possible and her cheerful ways made our setbacks more bearable.

The work done by Daniela Kruschel on d3'EBS1·IBS1 and her excellent record-keeping during her PhD was an invaluable help for me to start my project on d3'EBS1·dIBS1.

Thanks to Maximiliane Korth for introducing me to many new techniques in the lab and for guiding my steps during the first weeks of my PhD.

Special thanks goes to Nadja Bross, Simon Jurt, Prof. Dr. Oliver Zerbe and his group for the maintenance of the NMR facilities and for the prompt problem-solving at many occasions.

I am very grateful for the expert help with the setup and evaluation of the SPR experiments provided by Dr. Stefan Schauer and Dr. Jens Sobek from the functional genomics center Zurich.

Administrative help by Natalie Melunsky-Fichter and Ramona Erni is very much appreciated as well as Manfred Jöhri's help with the computer hardware.

I am obliged to Richard Börner, Daniela Donghi, Helena Guiset Miserachs, Silke Johannsen, Sebastian König and Magda Rowińska-Żyrek for reading and correcting the chapters of this thesis.

Many thanks to my office mates during the last year, Maria Pechlaner, Magda Rowińska-Żyrek, Marianthi Zampakou and Alicia Domínguez-Martín for bearing my occasionally horrible moods and for brightening each working day.

I would like to thank my parents, Hans and Ursula Skilandat, and my brother, Gunnar Skilandat, for their constant support and encouragement. It was their examples that taught me to take pleasure in learning and to form and defend my own opinions.
My love goes to my boyfriend, Georg Mühlbeier. Thank you for always inspiring me to be my best.
Thanks to all my friends in the Sigel and Freisinger labs for the good times!

Finally, I would like to thank all my teachers of science in school and university, who have sparked my scientific curiosity and shared their knowledge and passion to satisfy it.

Contents

Abbreviations & Symbols

Abbreviations

A	adenine
AAS	atomic absorption spectroscopy
ATP	adenosine 5’-triphosphate
BB	bromophenol blue
BMRB	biological magnetic resonance bank
bp	base pair
cDNA	complementary DNA
CPEB3	cytoplasmic polyadenylation binding element 3
COSY	correlated spectroscopy
C	cytosine
CTP	cytidine 5’-triphosphate
D	domain
DNA	deoxyribonucleic acid
DOSY	diffusion-ordered spectroscopy
DTT	dithiothreitol
EBS	exon binding site
Ec	*Escherichia coli*
EDTA	N,N,N’,N’-ethylenediaminetetraacetic acid
EPR	electron paramagnetic resonance
EST	expressed sequence tag
G	guanine
GTP	guanosine 5’-triphosphate
HDV	hepatitis delta virus
HEPES	4-(2-hydroxyethyl)-1-piperazineethanesulfonic acid
HMBC	heteronuclear multiple bond correlation
HPLC	high performance liquid chromatography
HQS	8-hydroxyqinoline-5-sulfonic acid
HSQC	heteronuclear single quantum coherence
IBS	intron binding site
IEP	intron encoded protein
Ll	*Lactococcus lactis*
LTR	long terminal repeat
MD	molecular dynamics
mRNA	messenger RNA
miRNA	microRNA

MOPS	3-(N-morpholino)propanesulfonic acid
MWCO	molecular weight cut-off
NAIM	nucleotide analogue interference mapping
NIR	near infrared
NMR	nuclear magnetic resonance
NOE	nuclear overhauser effect
NOESY	nuclear overhauser effect spectroscopy
nt	nucleotide(s)
O	*Oceanobacillus*
OT	oligonucleotide template strand
PAGE	polyacryamide gel electrophoresis
PDB	protein data bank
PEG	polyethylene glycol
Pl	*Pylaiella littoralis*
RDC	residual dipolar coupling
RNA	ribonucleic acid
RI	refractive index
Rm	*Sinorhizobium meliloti*
rMD	restrained molecular dynamics
RMSD	root mean square deviation
rRNA	ribosomal RNA
RT	room temperature
RU	response unit
Sc	*Saccharomyces cerevisiae*
siRNA	small interfering RNA
SNP	single nucleotide polymorphism
So	*Spinacia oleracea*
SPR	surface plasmon resonance
T	thymine
TBE	tris/borate/EDTA
TOCSY	total correlation spectroscopy
Tris	Tris(hydroxymethyl)aminomethane
tRNA	transfer RNA
TROSY	transverse-relaxation optimized spectroscopy
TS	top strand
TSAP	thermosensitive shrimp alkaline phosphatase
U	uracil
UTP	uridine 5’-triphosphate
UTR	untranslated region
UV	ultraviolet
Vis	visible
VS	varkud satellite
wt	wild type
XC	xylene cyanol

Symbols

A	area
c	concentration
δ	chemical shift
D	diffusion coefficient
ϵ	molar extinction coefficient
I	fluorescence intensity
J	J-coupling
η	viscosity
k_B	Boltzmann constant
K_D	dissociation constant
k_off	dissociation rate constant
k_on	association rate constant
r_H	hydrodynamic radius
t	time
T	temperature

1 Summary

Ribozymes are assumed to be remnants of the earliest biological systems, in which RNA was both information storage and catalyst. In recent organisms, they catalyze few, albeit most vital processes, such as protein synthesis, RNA splicing or single steps in virus replication. As in any catalyst, structure and function of a ribozyme are inseparable and, due to RNA's polyanionic nature, intimately linked to the positively charged metal ions present in the cell. In this thesis, two examples of the tight correlation between ribozyme structure and Mg^{2+} binding are investigated.

The first part of the thesis deals with the recognition of DNA cleavage sites in group II introns. These large ribozymes catalyze their own splicing, that is, their self-excision from an RNA transcript and the ligation of the two adjacent exons. By reversing this reaction, they are able to cleave DNA and RNA with high specificity and to reinsert at the site of cleavage. This ability accounts for the genomic mobility of group II introns and for their potential exploitation in gene therapy. The focus of this part of the thesis is on the first step in any DNA cleavage or reinsertion event; that is the formation of a short duplex between the exon binding site (EBS)1 of the intron and the intron binding site (dIBS)1 of the target DNA. The 7 bp EBS1·(d)IBS1 helix is formed directly at the 5' side of the scissile bond and is the longest of three base paired sequences, which position the two exons for either a splicing or a reinsertion event.

By determining the solution structure of the EBS1·(d)IBS1 complex, the kinetics of its formation and the location of metal ion binding sites, we investigated how the cleavage site is recognized by the intron and which is the role of metal ions in the recognition.

The construct used is derived from the *S. cerevisiae* ai5γ group IIB intron. It is a hairpin with an 11 nt loop, which contains EBS1 hybridized with the dIBS1 DNA 7mer. The NMR structure reveals the following main features: the hairpin stem is a regular A-form helix, the unpaired loop nucleotides are well-ordered and thereby allow partial stacking of the EBS1·dIBS1 helix on the stem, the loop backbone is strongly kinked opposite the cleavage site, and, the EBS1·dIBS1 helix is asymmetric and has a tunnel-shaped major groove with a highly negative electrostatic surface potential.

Using SPR, we could show that the EBS1·dIBS1 helix is marginally stable, but also that physiological concentrations of Mg^{2+} strongly increase the affinity between EBS1 and dIBS1. This stabilizing effect is also observed in EBS1·IBS1 RNA recognition site and in slightly different sequences of EBS1·(d)IBS1 and demonstrates the crucial importance of Mg^{2+} for a stable binding of the exon. By measuring Mg^{2+}-induced chemical shift perturbations, paramagnetic line broadening by Mn^{2+} and NOE correlations between the hybrid and $[Co(NH_3)_6]^{3+}$, two metal ion binding sites were characterized in EBS1·dIBS1. Metal ions bind near each end of the major groove of EBS1·dIBS1. Neither site is specific for inner- or outer-sphere contacts of the metal ion.

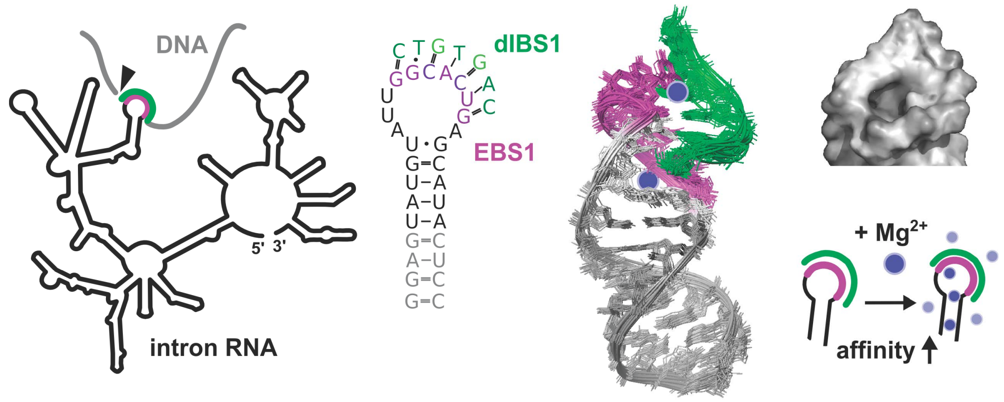

Part 1: EBS1·dIBS1 of a group IIB intron

Comparison of our construct to the corresponding RNA recognition site previously investigated by our group, reveals that, despite different helical geometries and a much lower stability of the hybrid, the main structural features and the location of metal ion binding sites of the RNA- and DNA recognition sites are the same. This suggests that the overall fold and electrostatic features of EBS1·dIBS1 are more relevant for cleavage site recognition than a specific helical conformation. One exception seems to be the sugar pucker at the cleavage site. It is C3'-*endo* in both the RNA and DNA target, suggesting that this conformation is required for the alignment of the scissile bond for catalysis.

We suppose that the kinked structure at the EBS1 5'-end is important for adjusting the scissile bond in the active site of the intron. This assumption is supported by a previously published crystal structure of a group IIC intron, which contains a similar kink. The tunnel-shape and negative potential of the EBS1·(d)IBS1 major groove are probably required to attract and harbor stabilizing metal ions. Both structural features mainly arise from the conformational limitation on EBS1·(d)IBS1 by being formed in a hairpin loop, while the negative potential in the major groove is due to two G·U/T wobble pairs, which are found in EBS1·(d)IBS1 of several group II introns. d3'EBS1·(d)IBS1 is thus an example of a structure that has evolved in group II introns to unspecifically attract metal ions to regions, whose stability is crucial for catalysis to proceed.

The small self-cleaving CPEB3 ribozyme is the subject of the second part of this thesis. It resides in the *cpeb3* gene of mammals and has a highly conserved sequence. The cellular function of the ribozyme is so far not clear but it probably regulates CPEB3 protein levels via its self-cleavage. The CPEB3 ribozyme is hypothesized to be the ancestor of the HDV ribozyme, as the characteristics of their cleavage reactions and their (proposed) secondary structures strongly resemble each other. This rather exceptional secondary structure contains two pseudoknots. The inner pseudoknot, formed by the P3 domain and the P1.1 minihelix, is embedded in an outer, larger one, which consists of the P1 and P2 helices. The P4 hairpin completes the ribozyme structure and is the only domain not involved in a pseudoknot. Both the CPEB3 and the HDV ribozyme are metalloenzymes that use Mg^{2+}

as a cofactor.

In order to gain insight into the solution structure of the CPEB3 ribozyme and into how it is shaped by metal ions, we used NMR spectroscopy to probe the secondary and tertiary structure of the ribozyme and to identify metal ion binding sites. A partial NMR assignment of the CPEB3 ribozyme was achieved with the help of three small hairpin constructs, which represent the P1, P2 and P4 domain, respectively. Based on this assignment, we localized binding sites of Mg^{2+} and $[Co(NH_3)_6]^{3+}$. The data were complemented by Tb^{3+}-induced hydrolytic cleavage experiments. In addition, the influence of different K^+ and Mg^{2+} concentrations on the hydrodynamic radius of the ribozyme, and the number of Mg^{2+} ions bound to one CPEB3 molecule were investigated.

Our data prove that the larger pseudoknot and P4 are stably formed in the absence of divalent metal ions. Addition of near physiological Mg^{2+} concentrations induces a compaction of the ribozyme, and results in the appearance of new NOE correlations indicative of the formation of extra base pairs in P3 and P1.1. There is evidence of a G·U wobble base pair being formed in P3, which is thought to bind and adjust the Mg^{2+} ion that participates in catalysis. Ion counting experiments determined four Mg^{2+} ions bound to one ribozyme while the NMR data and Tb^{3+}-induced cleavage experiments indicate up to eight binding sites. Both site-bound and diffuse Mg^{2+} ions interact with the ribozyme and mainly cluster in the smaller pseudoknot and the catalytic core of the ribozyme.

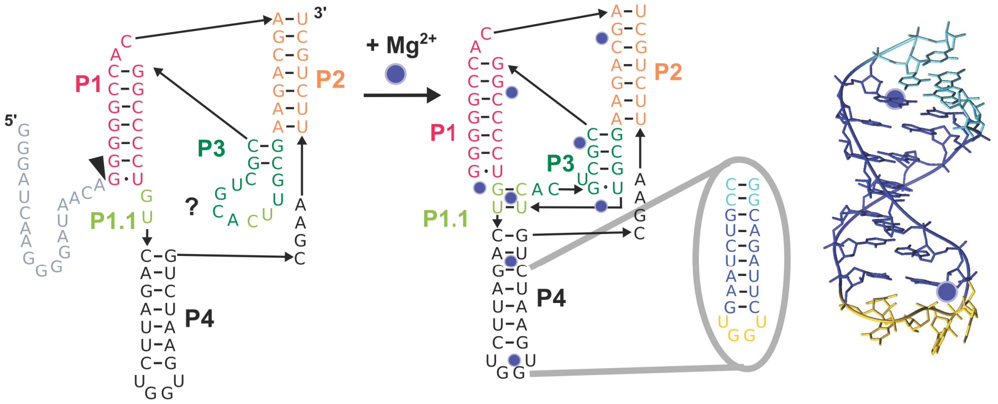

Part 2: the CPEB3 ribozyme

The results we obtained strongly support the proposition that the CPEB3 ribozyme adopts an HDV-ribozyme-like secondary structure in solution. They also point out the crucial importance of Mg^{2+} for a compact fold, in general, and for the formation of the smaller pseudoknot and of the catalytic center of the ribozyme, in particular. The formation of the Mg^{2+} binding G·U wobble was first suggested based on the HDV ribozyme crystal structure. The observation of an analogous interaction in the CPEB3 ribozyme suggests that both ribozymes use the same key metal ion binding motifs. It therefore corroborates the notion of a common structure and mechanism of both ribozymes in spite of their dissimilar sequences.

The NMR solution structure of the P4 domain was determined. The P4 construct has very similar NMR signals to those of the P4 domain within the CPEB3 ribozyme, indicating alike structures. P4 is a hairpin capped by a UGGU tetraloop, which is structurally well defined due to stacking of the first two nucleotides on the adjacent stem base pair and a hydrogen bond between a non-bridging phosphate oxygen of the second last, and the OH2' of the last loop nucleotide. This new tetraloop structure features two *syn* guanines. It thus resembles the characteristic structure of several AGNN tetraloops, which serve as endonuclease binding sites. This finding prompts the hypothesis that P4 might be a protein interaction site of the CPEB3 ribozyme, and might thereby mediate regulation of the self-cleavage activity.

This thesis illustrates two principal ways of how ribozymes engage Mg^{2+} ions to support their function. The EBS1·dIBS1 recognition site is a defined structure, which is optimized for positioning the scissile bond and for recruiting metal ions that stabilize the exon-intron contact during catalysis. The CPEB3 ribozyme relies on Mg^{2+} ions to adopt its native fold in the first place, which combines the stable frame formed by the outer pseudoknot with specific Mg^{2+} binding motifs in a flexible catalytic core. The investigation of the combinations of RNA structures with the different modes of metal ion-nucleic acid interactions is the key to understand how the diverse structures and functions of RNA could arise from the limited chemical repertoire of the four RNA bases.

2 Zusammenfassung

Es wird angenommen, dass Ribozyme Überbleibsel der frühesten biologischen Systeme sind, in denen RNA sowohl als Informationsspeicher als auch als Katalysator diente. In heutigen Organismen katalysieren Ribozyme nur wenige, aber dafür lebenswichtige Prozesse, wie zum Beispiel die Proteinsynthese, das Spleissen oder einzelne Schritte in der Replikation von Viren. Wie bei jedem Katalysator sind die Struktur und die Funktion von Ribozymen untrennbar miteinander verbunden, wie auch, aufgrund der vielfach-negativen Ladung von RNA, mit den positiv geladenen Metallionen in der Zelle. In der vorliegenden Dissertation werden zwei Beispiele dieser engen Verbindung zwischen Ribozym-Struktur und Mg^{2+}-Bindung untersucht.

Der erste Teil dieser Arbeit behandelt die Erkennung der DNA-Spaltstelle durch Gruppe II Introns. Diese grossen Ribozyme katalysieren ihr eigenes Spleissen, das heisst, sie schneiden sich selbst aus einem RNA-Transkript aus und ligieren die zwei angrenzenden Exons. Indem sie diese Reaktion umkehren, können die Introns RNA und DNA an spezifischen Stellen spalten und sich selbst an der Spaltstelle einfügen. Diese Fähigkeit macht ihre Beweglichkeit im Genom und ihr Potential für die Gentherapie aus. In diesem Teil der Arbeit liegt der Fokus auf dem ersten Schritt des Spleiss- oder Insertionsvorgangs: die Ausbildung einer kurzen Helix zwischen der Exonbindestelle (EBS)1 des Introns und der Intronbindestelle (dIBS)1 des DNA Substrates. Die 7 Basenpaare lange EBS1·dIBS1 Helix bildet sich direkt auf der 5'-Seite der zu spaltenden Bindung und ist die längste von drei basen-gepaarten Sequenzen, die die zwei Exons für das Spleissen beziehungsweise die Insertion ausrichten.

Um zu erforschen, wie die Spaltstelle vom Intron erkannt wird und welche Rolle Metallionen für die Erkennung spielen, klärten wir die Struktur des EBS1·dIBS1 Komplexes in Lösung auf, bestimmten die Kinetik seiner Bildung und die Anzahl und Position seiner Metallionenbindestellen.

Das verwendete Konstrukt stammt vom Gruppe IIB Intron ai5γ aus *S. cerevisiae*. Es handelt sich um eine Haarnadelstruktur mit einem Loop von 11 Nukleotiden, der das mit dIBS1 hybridisierte EBS1 beinhaltet. Die NMR-Struktur weist folgende Besonderheiten auf: der Stamm der Haarnadelstruktur ist eine reguläre A-Form Helix; die ungepaarten Nukleotide im Loop haben eine geordnete Struktur, die eine teilweise Stapelung der EBS1·dIBS1 Helix auf den Stamm erlaubt; das RNA-Rückgrat im Loop ist gegenüber der Spaltstelle stark abgeknickt; die EBS1·dIBS1 Helix ist asymmetrisch mit einer tunnelförmigen grossen Furche, die ein stark negatives Oberflächenpotential aufweist.

Mit Hilfe von SPR Messungen konnten wir zeigen, dass die EBS1·dIBS1 Helix nur gering stabil ist und, dass physiologische Mg^{2+}-Konzentrationen die Affinität von dIBS1 für EBS1 stark erhöhen. Dieser Stabilisierungseffekt ist auch bei leicht anderen EBS1·dIBS1 Sequenzen sowie bei dem EBS1·IBS1 RNA-RNA Komplex beobachtbar. Dies zeigt, wie wichtig

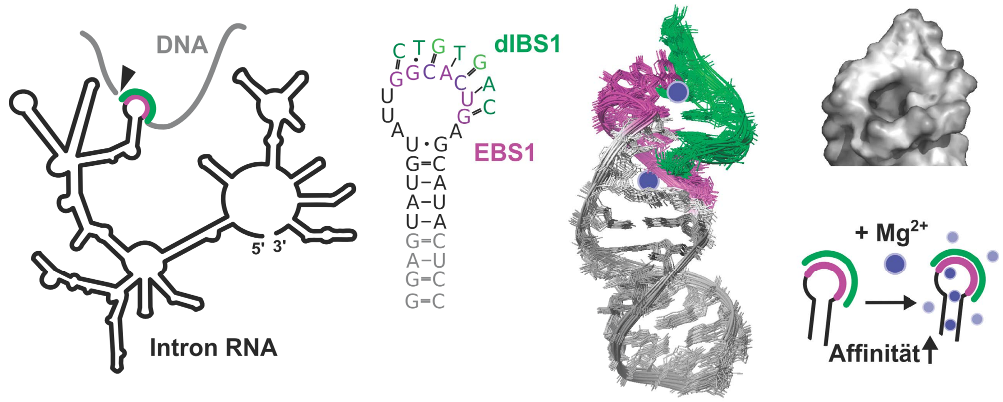

Teil 1: EBS1·dIBS1 eines Gruppe IIB Introns

Mg^{2+} für eine stabile Bindung von Exon und Intron ist. Mittels Messungen der durch Mg^{2+} verursachten Änderungen der chemischen Verschiebung, der paramagnetischen Linienverbreiterungen durch Mn^{2+} und von NOEs zwischen den Protonen von $[Co(NH_3)_6]^{3+}$ und dem Hybrid, charakterisierten wir zwei Metallionenbindestellen in EBS1·dIBS1. Diese liegen an den beiden Enden der EBS1·dIBS1 Helix und sind nicht spezifisch für eine direkte oder über H_2O-vermittelte Koordination von Mg^{2+}.

Der Vergleich unserer Ergebnisse mit dem zuvor in unserer Arbeitsgruppe erforschten EBS1·IBS1 RNA-RNA Komplex zeigt, dass trotz Unterschieden in der Helix-Geometrie und einer geringeren Stabilität des Hybrids, die strukturellen Hauptmerkmale und die Position der Metallionenbindestellen der RNA- und DNA-Erkennungskomplexe gleich sind. Dies legt den Schluss nahe, dass für die Erkennung der Spaltstelle die generelle Form und die elektrostatischen Eigenschaften von EBS1·(d)IBS1 wichtiger sind als eine spezielle Konformation der Helix. Eine Ausnahme stellt der *pucker* der Ribose an der Spaltstelle dar. Dieser ist sowohl im DNA- als auch im RNA-Substrat C3'-*endo*, vermutlich, weil dies für die Ausrichtung der zu spaltenden Bindung für die Katalyse wichtig ist.

Wir nehmen an, dass das abgeknickte Rückgrat notwendig ist, um die zu spaltende Bindung korrekt im aktiven Zentrum des Introns zu platzieren. Diese Annahme wird durch die zuvor publizierten Kristallstrukturen eines Gruppe IIC Introns gestützt, die einen ähnlichen Knick aufweisen. Das negative Potential und die Tunnelform der grossen Furche von EBS1·dIBS1 dienen wahrscheinlich dazu, stabilisierende Metallionen anzuziehen und zu beherbergen. Beide strukturellen Merkmale kommen vor allem dadurch zustande, dass EBS1·dIBS1 sich innerhalb des Haarnadel-Loops bildet, was seine möglichen Konformationen stark eingeschränkt. Das Oberflächenpotential wird vor allem durch die negative grosse Furche der G·U/T *wobble* Basenpaare bestimmt, welche sich in den EBS1·dIBS1 Helices verschiedener Gruppe II Introns finden. EBS1·dIBS1 ist somit ein Beispiel dafür, wie Gruppe II Intron Strukturen sich dahin entwickelt haben, unspezifisch Metallionen in Regionen zu binden, deren Stabilität unabdingbar für den katalytischen Mechanismus ist.

Das kleine selbstspaltende CPEB3 Ribozym ist Thema des zweiten Teils dieser Dissertation. Es kommt im *cpeb3* Gen von Säugetieren vor und hat eine hochkonservierte Sequenz. Die Funktion des Ribozyms in der Zelle ist bisher nicht geklärt aber wahrscheinlich reguliert seine Selbstspaltung die Konzentration des CPEB3 Proteins. Man nimmt an, dass das HDV Ribozym vom CPEB3 Ribozym abstammt, da sich ihre Spaltungsreaktion und ihre (vorgeschlagene) Sekundärstruktur stark ähneln. Diese Sekundärstruktur ist insofern aussergewönlich, als dass sie zwei Pseudoknoten umfasst. Der innere Pseudoknoten, der von der P3 Domäne und der P1.1 Minihelix gebildet wird, ist in den äusseren Pseudoknoten eingebettet, der aus den P1 und P2 Helices besteht. Die P4 Helix vervollständigt die Struktur und ist die einzige Domäne, die keinen Pseudoknoten bildet. Sowohl das HDV~ als auch das CPEB3 Ribozym sind Metallenzyme, die Mg^{2+} als Kofaktor verwenden.

Um zu untersuchen, ob das CPEB3 Ribozym in Lösung die vorgeschlagene Struktur aufweist, wurden die Sekundär- und Tertiärstruktur des Ribozyms mittels NMR-Spektroskopie charakterisiert. Eine teilweise Zuordnung der NMR Signale wurde unter Zuhilfenahme von drei kleinen Haarnadelkonstrukten erreicht, welche die P1, P2 und P4 Domäne darstellen. Anhand dieser Zuordnung, lokalisierten wir die Bindestellen von Mg^{2+} und $[Co(NH_3)_6]^{3+}$. Die Ergebnisse wurden durch Experimente der Tb^{3+}-induzierten hydrolytischen Spaltung ergänzt. Zusätzlich wurde der hydrodynamische Radius des Ribozyms in Abhängigkeit von der K^+ und Mg^{2+} Konzentration untersucht, sowie die Anzahl der an das Ribozym gebundenen Mg^{2+} Ionen bestimmt. Die Kombination dieser Methoden half zu verstehen, welche Rolle Metallionen für die Ausbildung der Ribozymstruktur spielen.

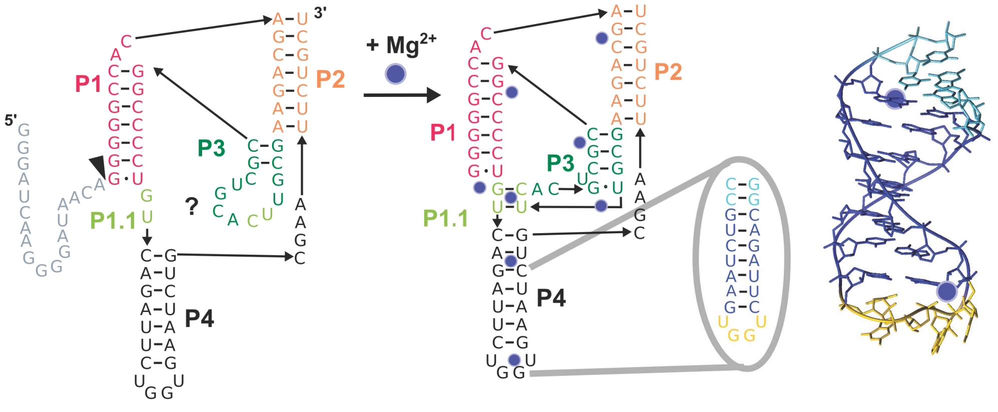

Teil 2: das CPEB3 Ribozym

Unsere Ergebnisse beweisen, dass der äussere Pseudoknoten und P4 sich auch in Abwesenheit von divalenten Metallionen stabil ausbilden. Die Zugabe nahe-physiologischer Konzentrationen von Mg^{2+} bewirkt eine Kompaktierung des Ribozyms, sowie das Auftauchen neuer NOE-Korrelationen, die auf die Ausbildung von Basenpaaren in P1.1 und P3 hindeuten. Zum Beispiel scheint sich ein G·U *wobble* Basenpaar in P3 zu bilden, von welchem man annimmt, dass es das katalytische Mg^{2+} Ion im aktiven Zentrum positioniert. Stöchiometrie-Bestimmungen ergaben, dass 4 Mg^{2+} Ionen an das Ribozym gebunden

sind, wohingegen die NMR Daten und die Tb^{3+}-induzierte-Spaltungsexperimente auf bis zu acht Mg^{2+}-Bindestellen hinweisen. Sowohl diffuse als auch chelierte Mg^{2+} Ionen interagieren mit dem Ribozym und reichern sich vornehmlich im kleinen Pseudoknoten und im katalytischen Zentrum an.
Die von uns gesammelten Daten liefern starke Argumente dafür, dass das CPEB3 Ribozym in Lösung die vorgeschlagene, dem HDV Ribozym ähnliche Sekunsdärstruktur einnimmt. Sie zeigen auch die kritische Rolle auf, die Mg^{2+} für eine kompakte Faltung des Ribozyms im Allgemeinen, und für die Struktur des inneren Pseudoknotens und des katalytischen Zentrums, im Speziellen, spielt. Die Bildung des Mg^{2+}-bindenden G·U *wobble* Basenpaares wurde auf Grund der Kristallstruktur des HDV Ribozyms vorgeschlagen. Die Beobachtung eines entsprechenden G·U-Paares im CPEB3 Ribozym zeigt, dass beide Ribozyme gleiche, katalytisch wichtige Metallionen- bindende Motife verwenden. Dies untermauert die Ansicht, dass sich das CPEB3- und das HDV Ribozym, trotz ihrer verschiedenen Sequenzen, in Struktur und Mechanismus gleichen.
Die NMR Struktur der P4 Domäne in Lösung wurde aufgeklärt. Das P4 Modellkonstrukt weist sehr ähnliche NMR-Signale wie die P4 Domäne innerhalb des CPEB3 Ribozyms auf, was auf identische Strukturen schliessen lässt. P4 ist eine Haarnadelstruktur, die durch einen UGGU Tetraloop abgeschlossen wird. Durch Stapelung der ersten zwei Loop-Nucleotide auf das angrenzende Basenpaar sowie durch eine Wasserstoffbrücke zwischen einem freien Phosphatsauerstoff des vorletzen Nucleotids und einer OH2'-Gruppe des letzten Loop-Nucleotids erhält der Loop eine gut definierte Struktur. Diese neue Tetraloopstruktur beinhaltet zwei Guanine in *syn*-Konformation. Sie erinnert dadurch an die charakteristische Konformation verschiedener AGNN Tetraloops, die als Endonuklease-Bindestellen fungieren. Diese Ähnlichkeit legt den Schluss nahe, dass es sich bei P4 um eine Protein-Interaktionsdomäne des CPEB3 Ribozyms handeln könnte, über die womöglich eine Regulation der Selbstspaltung erfolgt.

Diese Dissertation verdeutlicht zwei prinzipielle Möglichkeiten der Einbindung von Mg^{2+} Ionen in die Funktion von Ribozymen. Die EBS1·dIBS1 Erkennungs-Helix ist eine definierte Struktur, die einerseits für das Ausrichten der zu spaltenden Bindung, und andererseits für die Rekrutierung von Metallionen zur Stabilisierung des, während der Katalyse ans Intron gebundenen Exons, optimiert ist. Das CPEB3 Ribozym benötigt von vornherein Mg^{2+} Ionen, um seine native Faltung zu erreichen. Diese kombiniert den stabilen Rahmen, den der äussere Pseudoknoten bildet, mit spezifischen Mg^{2+}-Bindestellen in einem flexiblen katalytischen Kern. Die Erforschung solcher Verbindungen von RNA-Strukturen mit den unterschiedlichen Interaktionsmodi von Metallionen und Nukleinsäuren ist der Schlüssel zum Verständnis davon, wie das beschränkte chemische Repertoire der vier RNA Basen so diverse Strukturen und Funktionen hervorbringen konnte.

3 Introduction

3.1 RNA functions in a nutshell

In the past 60 years RNA research has made extraordinary conquests of novel topics, as RNA became implicated in more and more cellular processes and qualified itself as a new tool in therapy and research application. Landmark discoveries regarding RNA function were those of the role of mRNA and tRNA in translation of the genetic code, of RNA viruses, of catalytically active RNA and the first insights into the plethora of regulatory functions performed by RNA, such as RNAinterference.

Already in the 1950s, it was well established that RNA acts as an information shuttle between DNA, which stores the hereditary information and proteins, which execute this information in the cell [1]. This is the function of mRNAs, transcripts of DNA sequences that are exported from the nucleus and processed to be templates for protein translation, and tRNAs, which act as adapters between mRNA codons and the corresponding amino acids in protein synthesis [2]. Although hypotheses on the potential catalytic role of RNA were expressed early by Crick, Woese and Orgel [3–5] experimental evidence was lacking until the late 1970s. In 1978, Sidney Altman obtained first prove that the RNA moiety of the RNA-cleaving RNA-protein complex RNase P from *Escherichia coli* is essential for catalysis [6], and later demonstrated that the protein moiety is dispensable [7]. Thomas Cech showed that in the protozoan *Tetrahymena thermophila* an RNA catalyzes its own splicing reaction in the absence of any protein [8, 9]. In 1989, Cech and Altman were awarded the Nobel prize in chemistry for their discovery of the catalytic properties of RNA. Such RNA enzymes (short: ribozymes) as RNase P and the self-splicing introns are examples of RNA function that relies on an intricate 3D structure of the RNA molecule. Another example of a structure-function relationship in RNA are riboswitches [10–12], which were discovered two decades after the first ribozymes. These regulatory RNA sequences form highly specific binding platforms for small ligands in the 5'-UTR of certain genes. Upon binding or release of their specific ligand, riboswitches change their conformation, thereby adapting gene expression to the availability of a certain metabolite (their ligand) in the cell. The arsenal of functional RNA extends further: in RNA viruses RNA itself serves as the genetic material; RNA mediates genomic mobility of certain transposable DNA sequences; small nuclear RNAs act in splicing and ribosomal RNAs in protein translation; and small nucleolar RNAs process tRNA, rRNA and snRNA during their biogenesis.

The discovery of antisense RNA [13] and RNAinterference (RNAi) [14] brought to light the immense regulatory importance of non-coding RNAs. Both mechanisms regulate gene expression on the mRNA level using complementary ncRNAs, which either block the complementary mRNA from being translated (antisense) or promote its degradation (RNAi).

Today we know that the influence of RNA in the cellular information flow is omnipresent. RNA's many roles, extending from acting as the hereditary substance to catalyzing different crucial reactions in a self-replicating system, have inspired the idea of a primordial RNA world, in which RNA had dual function of being both information storage and the catalyst of its own replication [15, 16]. This idea is supported by *in vitro* evolution techniques [17] that have been used to select RNA sequences catalyzing a variety of other reactions, which widely extend the catalytic repertoire of the current natural ribozymes. Today's naturally occurring ribozymes have gained a lot of attention for potentially being active fossils of such an RNA world and thus for their enormous potential to teach us about molecular evolution. However, ribozyme research is far from looking solely into the past. Several ribozymes as well as artificial DNAzymes [18] are being developed for molecular medicine [19], for synthetic biology applications [20] and as biosensors [21]. For example, phase II clinical trials have successfully been completed for a chemically stabilized ribozyme, which was designed to cleave a certain cancer-related mRNA for tumor therapy [22].

Research on catalytic RNA and DNA has become a vibrant field and a detailed insight into how their native structures are shaped will help to understand and exploit their catalytic and regulatory functions.

3.2 Thesis outline and aims

This thesis is concerned with the investigation of ribozyme structure and how it is shaped by metal ions. It comprises two independent research projects on two metal-dependent ribozymes. Each project is comprehensively treated in a separate chapter, which includes the introduction to the particular subject as well as the aims and results of the project and their discussion. The methods and material used for both projects is described in the experimental section.

The first project (Chapter 4) investigates the structure and affinity of a hybrid intron-exon recognition site of a group II intron. At this site, the intron forms a short duplex with an RNA or DNA exon and cleaves this exon 3' to the recognition sequence, which the first step of any cleavage, self-splicing or reinsertion event of a group II intron. We studied the structural requirements for making the scissile bond recognizable for the catalytically active domains of the intron and the role that Mg^{2+} plays for the structure and stability of the hybrid duplex. Also, we aimed to extrapolate common principles for the structure and metal ion binding of the exon-intron recognition complexes of other group II introns. These problems were addressed by determining the NMR structure and the metal ion binding sites of the complex, by using SPR for studying the kinetics of the interaction, and by comparing our results to those of the RNA-RNA exon-intron recognition site [23].

In the second project (Chapter 5) the small self-cleaving CPEB3 ribozyme was investigated. There is multiple evidence that the CPEB3 ribozyme folds into a similar intricate double-pseudoknot topology and cleaves in the same Mg^{2+}-dependent way as the HDV ribozyme. We provided NMR-spectroscopic proof of the proposed structural similarity and investigated in how far Mg^{2+} is required for pseudoknot formation. Using NMR in combination with biochemical assays, we analyzed the number, location and nature of metal ion binding sites of CPEB3 in detail and drew parallels to the binding sites observed in the

HDV ribozyme. We demonstrated the importance of Mg^{2+} for a compact fold of CPEB3 and gained evidence for an example of a Mg^{2+} binding site being both structurally and catalytically relevant, which appears to be common to the HDV-like ribozymes.

3.3 Statement on published contents

Parts of this thesis have been published, such as the majority of Section 3.6 of the introduction in [24], the entire Chapter 4 (text, tables and figures) and Sections 6.5 and 6.6 of the Experimental Section in [25] and Sections 5.5, 5.6.2 and 5.7.3 of Chapter 5 in [26]. All citations (except for Chapter 4) are included as direct quotations. Part of the unpublished work presented in Chapter 5 was done in collaboration with Dr. Magdalena Rowińska-Żyrek, University of Zurich. This concerns: the production and NMR data acquisition of the mutant CPEB3 constructs (Section 5.2), the Mg^{2+}-titration of the P1 model construct, the assignment of the nonexchangeable CPEB3 protons (Section 5.4.3) in the spectra of the full-length construct as well as the stoichiometry measurements (Section 5.6.5).

3.4 Nucleic acid structure

3.4.1 Primary structure

There are two types of nucleic acids: deoxyribonucleic acid (DNA) and ribonucleic acid (RNA). Both are strictly linear polymers assembled from four different building blocks called nucleotides. Each nucleotide consists of a ribose or 2'-deoxyribose moiety (in RNA or DNA, respectively), that carries a phosphate group at the C5' position and one of four nucleobases at the C1' position (Figure 3.1a). The four nucleobases are adenine, cytosine, guanine and thymine in DNA and adenine, cytosine, guanine and uracil in RNA (Figure 3.1b). The nucleotides of one RNA or DNA strand are all linked in the same way, that is by a phosphodiester bridge between the 3'-OH group of one nucleotide to the phosphate of the following nucleotide (Figure 3.1a). Accordingly, each DNA or RNA strand has one 5'-end and one 3'-end; this chemical directionality is essential for any process that involves read-out or synthesis of DNA or RNA.

Although the chemical difference between the RNA and DNA sugar-phosphate backbones is small, its impact on structure, structural diversity, stability and function of the two nu-

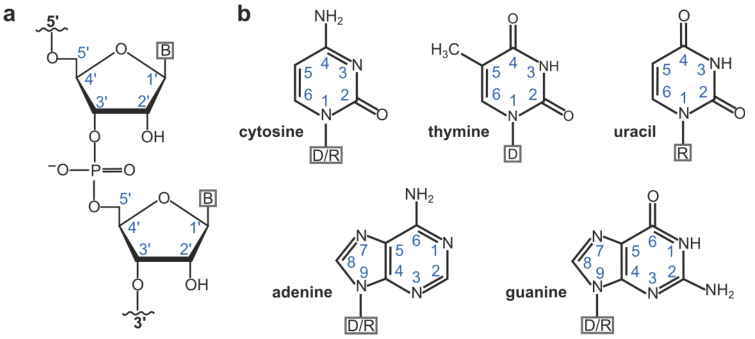

Figure 3.1: The basic building blocks of nucleic acids. a) the sugar-phosphate backbone of RNA. B stands for any RNA base A, G, C or U b) the five bases. D and R stand for one DNA or RNA sugar-phosphate unit, respectively.

cleic acids is paramount. DNA, having two protons attached to C2', is remarkably stable, permitting analysis of genome fragments from long extinct species. The 2'-OH group of RNA endows it with a much higher reactivity than DNA at the cost of a markedly decreased stability. It is this "dagger pointing at its own heart" (Prof. David M.J. Lilley), which allows RNA to catalyze a set of chemical reactions (Section 3.6).

3.4.2 Secondary and tertiary structure

Under physiological conditions DNA is always double stranded, unless it is being replicated, read out for RNA transcription or repaired. This means a helix is formed with the bases pointing inwards, forming pairs via hydrogen bonds, and with the phosphates running along the outside in a spiral shape (Figure 3.2). The main determinant of helix stability are π-stacking interactions between the nucleobases [27]. Two grooves can be discriminated along a helix that are defined by which edge of the base pairs they contain (Figure 3.3a-c). The predominant geometry of DNA is the right-handed B-form helix (Figure 3.2). This helical conformation is characterized by a wide and shallow major groove and narrow minor groove, a C2'-*endo* type sugar puckers, a diameter of 2 nm and a pitch[1] of 3.32 nm [28].

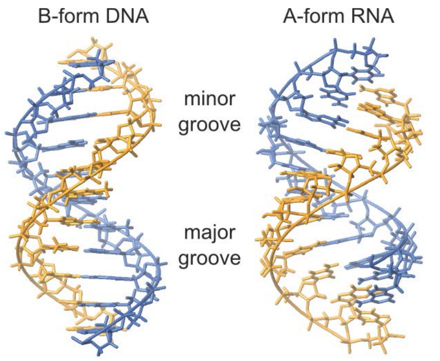

Figure 3.2: Comparison of A-RNA and B-DNA conformation. The groove indicated is the one facing the front. The figure was prepared from pdb files of idealized A-RNA and B-DNA (http://www.biochem.umd.edu/-biochem/kahn/teach_res/dna_tutorial/).

Depending on salt concentrations and water content, also A-DNA and the the rare, left-handed Z-DNA [29, 30] helices are observed. RNA helices occur only in A-form. A-RNA is wider but more compact than B-form DNA (Figure 3.2), with a diameter of 2.4 nm and a pitch of 2.46 nm. Its major groove is deep and narrow and the sugar conformation is C3'-*endo* [28]. Beyond A-RNA double strands, RNA is free to assume a variety of secondary structures through base pairing interactions. The most common motifs are shown in (Figure 3.3d-j). Apart from the Watson-Crick base pairs (Figure 3.3a and b), also G·U (Figure 3.3c), G·T and A·C wobble base pairs can be formed. Unusual base pairs, such as reverse base pairs, where the two glycosidic bonds are in opposite directions and Hoogsteen base pairs that involve purine N7 as a hydrogen bond acceptor are also observed [31, 32]. Such unusual base pairs are often relevant for the formation of tertiary structure or in the formation of continuous triplexes and G-quadruplexes.

Building on this variety of secondary structure elements, diverse tertiary structures can be formed by RNA, the most frequent elements being coaxially stacked helices, kissing

---

[1] the height of one complete turn as measured parallel to the helix axis

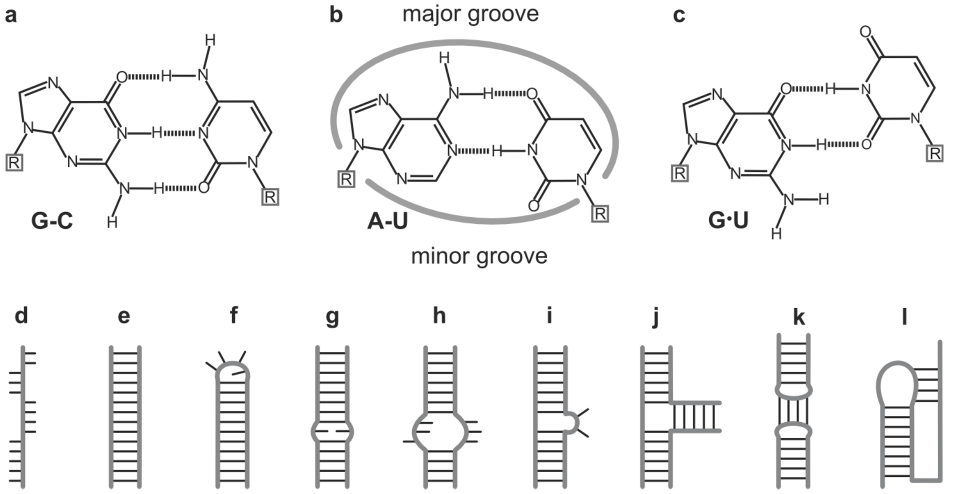

Figure 3.3: RNA structural elements. (a-c) Three common base pairs formed in RNA: the Watson-Crick base pairs A-U and G-C and the G·U wobble; (d-l) secondary structure motifs occurring in RNA: (d) single-strand (e) double helix (f) hairpin (stem-loop) (g) mismatch (h) internal loop (i) bulge (j) three-way junction (k) kissing loops (l) pseudoknot.

loops/hairpins [33, 34] (Figure 3.3k), pseudoknots (Figure 3.3l), tetraloop-receptor complexes, A-minor interactions and ribose zippers.

The simplest example of tertiary structure are stacking interactions. Coaxial stacking between two helices frequently occurs in large RNAs such as the group I and II introns [35,36] and tRNA [37] but is also found in smaller RNAs, for example between the helices of a pseudoknot [38]. Another common motif is the tetraloop-receptor interaction between GNRA tetraloops and tetraloop receptors [39–42], which consists of an A-rich bulge and the adjacent base pairs. The tetraloop and the receptor interact via a distinct combination of stacking interactions and hydrogen bonds, and thereby enable a compaction of sequentially distant domains as for example in the group I and group II introns [40, 41]. Another important feature is the A-minor interaction, where the minor groove edge of adenine is inserted into the minor groove of another helix forming hydrogen bonds to the 2'-OH of the helical base pairs [43]. This type of interaction was first found to occur frequently in the ribosomal subunits. Hydrogen bond formation between 2'-OH groups of neighboring strands are also responsible for the formation of so-called ribose-zippers [39, 44, 45]. Finally, an interaction between two loops based on mutually intercalating bases has been characterized in tRNA [46].

Just like protein folding, RNA folding, meaning the formation of the native ensemble of all secondary and tertiary structure elements, is a complex and diverse process, whose outcome cannot yet be predicted from the primary sequence. Large RNAs fold into their native 3D structures in a hierarchical fashion [47]. This means that secondary structure elements are formed first and then collapse to form tertiary contacts, which usually entails a significant compaction of the molecule. While some large RNAs as RNase P and the group I intron have a rugged energy landscape featuring long-lived intermediate states and alternative pathways, group II introns fold directly to the native state via on-pathway intermediates [48,49]. Several proteins have been implicated in guiding the folding process of RNA [50]. Examples are RNA helicases and RNA chaperones, such as Hfq that mediates the annealing of small regulatory RNAs with their target mRNAs [51], and the ribosomal proteins tightly associated with the ribosomal RNA. In some cases, substantial refolding is an intrinsic part of RNA function as in the case of riboswitches, in which the structural switch is triggered by metabolite binding.

RNA folding on any level is intimately related to the presence of cations, usually the mono- and divalent metal ions in the cell.

3.5 Metal ion interactions with nucleic acids

3.5.1 Modes of interaction

As both RNA and DNA are polyanions, formation of any secondary or tertiary structure relies on the presence of positive counterions. These counterions can be divided in two classes: the diffuse and the site-bound ions. The diffuse cations are the vast majority; they form a cloud around the nucleic acid while remaining fully solvated and mobile. This provides charge screening to the polyanionic sugar-phosphate backbones, so they can approach each other during the formation of secondary and tertiary structure. Site-bound ions engage in short-range interactions with the nucleic acid and thus remain in place. Such ions are attracted to regions of condensed negative surface potential with special geometries (Section 3.5.2) and normally have two or more inner-sphere RNA or DNA ligands. The energetic contributions of a site-bound interaction are more complicated than the simple electrostatic interaction of diffuse ions with RNA. For site-bound ions, also the energies of (partial) dehydration of the RNA and the metal ion as well as charge-transfer and polarization must be considered [52]. The diffuse ions, due to their sheer excess, are by far more important for the overall thermodynamic stability of a folded RNA than the site-bound ions. In contrast to this, complex tertiary structures, namely those of large RNAs usually require binding of di- or multivalent cations to distinct sites.

The discrimination of diffuse and site-bound ions [53] has been challenged for being too simplistic [54, 55]. Indeed, there is a continuum of metal ion-nucleic acid interactions, which fall in between the two classes. Some authors distinguish three classes of metal ions (chelated, water-positioned and diffuse ions [54]) or even four (chelated/coordinated, glassy/restricted, condensed/associated and free/bulk solution ions [55]). All three formalisms have in common that from one class to the next, the number of ions, the relevance for thermodynamic stability and the mobility of the ions increase, while the significance for the tertiary structure decreases. Inner-sphere interactions between the nucleic acid and the metal ion occur only in the first class. However, matters are more complicated than the number of inner-sphere RNA ligands generally being proportional to the structural relevance of a metal ion. RNA tertiary structures can provide a wealth of different binding pockets with high negative charge density, many of which are not selective for a specific ion or binding mode but nonetheless structurally or even catalytically relevant [56–59].

3.5.2 Mg^{2+} plays a pivotal role in RNA structure formation

The interaction of a metal ion with a nucleic acid depends on the ionic radius and the charge, which in turn define the charge density, hydration energy and the coordination preferences of the metal ion.

K^+ and Mg^{2+} are the most abundant mono- and divalent metal ion in the cytosol, which attributes special significance to their interaction with nucleic acids. In the case of RNA, the paramount importance of Mg^{2+} for folding has been demonstrated in many studies (for example [49, 60–64]) on a variety of differently complex RNAs. It is thus not surprising that any larger RNA investigated so far harbors several structurally relevant Mg^{2+} binding sites; see for example the discussions of Mg^{2+} binding sites in tRNA [65], the ribosome [66], RNase P [67], the group I intron [68], group II intron [58] and the preQ1 riboswitch [69]. How exactly Mg^{2+} acts in the the folding process of RNA is not yet understood. Recent studies have put forward the idea that Mg^{2+} reduces the activation entropy and overall entropy by binding preferentially to unstructured regions, thereby reducing the conformational space [70, 71].

The ability of Mg^{2+} to stimulate compact folds in RNA stems from its high charge density; it has a charge of +2 and a radius of 0.65 Å compared to K^+, that has a +1 charge and a radius of 1.3 Å. This allows Mg^{2+} to pack six oxygen ligands (for example of water or phosphate oxygens) in a dense octahedral arrangement of high stability, which is reflected by the slow ligand-exchange rate [72] and by the much larger hydration energy of Mg^{2+} (-455 kcal/mol [73]) compared to the one of other relevant cations in the cytosol such as Na^+ (-100 kcal/mol [74]) or K^+ (-80 kcal/mol [54]). This tightly packed geometry is thus not accessible for RNA in monovalent ions alone due to the strong repulsion of the phosphate oxygens.

On the side of the nucleic acid, the nonbridging phosphate oxygens make excellent inner-sphere ligands for Mg^{2+}. Binding to the exocyclic nucleobase oxygens GO6, T/UO4 and T/UO2, the endocyclic nucleobase nitrogens (A/GN7, CN3), to the bridging phosphate oxygens and to the 2'-OH is also observed [75–77]. The main determinants for a suitable Mg^{2+} binding site are thus the type of ligands being available, their geometry, and the local flexibility of the RNA. Two quite different examples of Mg^{2+} binding sites in RNA are shown in Figure 3.4.

The affinity of Mg^{2+} binding to nucleic acids is rather low in most sites, with K_D values in the low millimolar range [80–83]. However, Mg^{2+} ions with a high number of inner-sphere RNA ligands can bind with K_D of 2 µM [84], provided the binding site is buried within a globular or quasi-globular RNA structure and therefore shielded from the solvent water.

Apart from the structural significance of Mg^{2+} ions, they are also specific cofactors in the catalytic mechanism of many ribozymes (Figure 3.7b). Mg^{2+} can participate in catalysis through activation of the attacking nucleophile by proton abstraction, via stabilization of the leaving group or of the transition state [85], or indirectly by facilitating binding of the substrate or cofactor such as in the *glmS* ribozyme [86]. It must be borne in mind that ribozyme folding and activity are inextricably linked as in any enzyme. It is thus rarely possible (or sensible) to strictly discriminate between catalytic and structural Mg^{2+} ions.

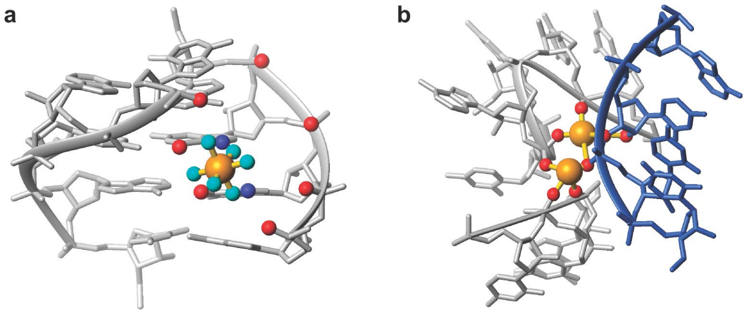

Figure 3.4: Two examples of Mg^{2+} bound to RNA. (a) A glassy Mg^{2+} ion in a group I intron (pdb ID: 1HR2 [78], MG: 6766). The ion (gold) is coordinated by water molecules (cyan) and binds to a major-groove site offering a number of suitable second-shell ligands, marked as blue (N) and red (O) spheres, such as guanine O6 and N7 of two consecutive guanines and nonbridging phosphate oxygens. (b) Two site-bound/chelated Mg^{2+} ions in a group II intron active site (pdb ID: 3G78 [79] MG:8548,8549). The ions are coordinated between the backbones of the substrate strand (blue) and the catalytically active domain of the intron (grey). The bulge in the upper strand is critical for arranging the phosphate oxygens in a suitable geometry for coordinating the two ions.

It is assumed that RNA tertiary architectures have evolved in an intimate relation with magnesium [87], which is one of the most abundant metals of the earth crust and in sea water. One argument for this theory comes from the Mg^{2+} density in the ribosome. Ribosomal RNA is thought to be evolutionary ancient and likely obtained its present form before the last universal ancestor of all existing species [88]. The Mg^{2+} density in the centre of rRNA is very high and decreases towards the outer parts [89], where the ribosomal proteins have possibly taken over and refined the structure-forming and -stabilizing role of Mg^{2+} in the course of evolution [89].

Despite the outstanding relevance of Mg^{2+} for RNA structure, there is evidence for appreciable plasticity in metal-nucleic acid relationships. Most small ribozymes are able to use different metal ions for catalysis [90–93] and *in vitro* selection strategies have yielded different ribozymes and even DNAzymes that are very specific for metal ion cofactors such as Pb^{2+} [94] and Zn^{2+} [95].

3.6 Ribozymes

3.6.1 Small ribozymes

All ribozymes can be divided into the large ribozymes (Section 3.6.2) and the small or 'small self-cleaving' ribozymes. The five small ribozymes are the hammerhead, the hairpin, the HDV, the VS and the *glmS* ribozyme [96]; they "catalyze intramolecular cleavage reactions in RNA. These self-cleaving ribozymes cleave their substrate at specific sites, which is achieved by Watson-Crick base-pairing of adjacent sequences with the substrate. The hammerhead, hairpin, HDV and VS ribozymes are located in RNA satellites of mainly plant viruses, but they also occur in the genomes of various species such as fungi, worms

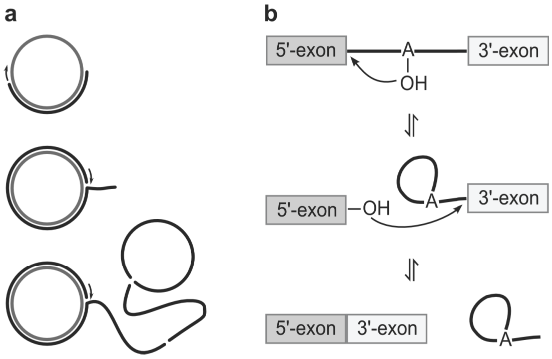

Figure 3.5: a) Rolling circle replication of the satellite genome. A host RNA polymerase continuously transcribes from the circularized genomic strand (grey) creating a linear series of antigenomic strands (black). A small ribozyme encoded in each of these copies self cleaves to generate single copies of the genome. These again circularize being ligated by the same ribozyme and serve as templates for transcription of the genomic strand in the second half of the replication process. b) The splicing reaction of the group II intron and the eukaryotic spliceosome (see text for description).

and fish. All four ribozymes are required to separate genome copies of these satellites [97–101] created by rolling circle replication [102], (Figure 3.5a) and thus catalyze both strand cleavage and the reverse strand ligation.

Both hammerhead and hairpin ribozyme were discovered in 1986 in the tobacco-ringspot virus satellite on opposite strands of the genome [103,104]. With only about 40 nucleotides in length, the hammerhead ribozyme is the smallest natural ribozyme. Its name refers to the secondary structure that comprises three helices with one common junction at which all nucleotides relevant for catalysis are clustered [105] (Figure 3.6a).

The HDV ribozyme [106] is located in the genome of the Hepatitis delta virus, a human pathogen that can superinfect patients already infected with Hepatitis B. Its structure consists of five helices forming a double pseudoknot [107], which makes it extremely stable to heat and denaturing agents. This ribozyme is located on both the sense and the antisense (genomic and antigenomic) strand of the virus with different sequences, but corresponding three-dimensional structures." [24][2] Both the hammerhead and the HDV motifs have later been discovered in many genomes throughout the kingdoms of life [108, 109]; the evolutionary connections behind this observations are, however, not clear to date.

The hairpin ribozyme consists of two connected helices with large internal loops (Figure 3.6b). The minor grooves of the helices are facing each other and thereby form the active site [110]. Most remarkable about the hairpin ribozyme is that the reactive group arrangement in its catalytic center is highly similar to that of the protein enzyme RNase A, proving that nucleobases can do acid-base chemistry analogous to amino acid side-chains.

"The VS ribozyme was discovered in 1990 in a transcript of the mitochondrial genome of the mould *Neurospora crassa* [111]. With an average length of 150 nucleotides it is rather large for a small ribozyme. Five helices organized by two three-way junctions form the structure of this ribozyme [112][, whose 3D structure is yet to be determined].

The *glmS* ribozyme was discovered in 2004 in *Bacillus subtilis* and other gram-positive bacteria [113,114]. It is the only small ribozyme, which requires a cofactor for catalysis and the only one that is known to act as a riboswitch. It regulates expression of certain genes responsible for the production of its own cofactor, glucosamine-6-phosphate (GlcN6P).

---

[2] References to the original literature were not part of the source [24] but added for this thesis.

Cleavage of the mRNA only takes place when GlcN6P is bound to the ribozyme, thus halting the production of GlcN6P." [24]

The family of small ribozymes keeps growing and likely has more undiscovered members. The CoTC motif, found in the 3'-UTR of primate β-globin genes [115] is one example as well as the twister ribozyme recently discovered in the genomes of various organisms [116]. With the now available sophisticated *in vitro* selection techniques [117–121] and new bioinformatic tools that allow searching the genome for (nonconserved) sequences able to fold into a certain structure [113, 122–124], we expect to see more candidates any time.

3.6.2 Large ribozymes

"The large ribozymes comprise group I and II introns as well as the ribosome, the spliceosome and RNase P, the latter three being all large ribonucleoprotein complexes [6]. These ribonucleoprotein ribozymes are true catalysts that catalyze multiple reaction turnovers without being altered in the process. Instead, all other ribozymes catalyze only one cleavage or splicing event. RNase P works like protein RNases but has a catalytic core comprised solely of RNA [7]. It catalyzes the removal of the 5'-leader sequence from precursor tRNA [125]. Generally, RNase P is found in archea, bacteria, eukarya, as well as mitochondria and chloroplasts. [*In vivo*, only] bacterial RNase P has been shown to function also in the absence of its protein unit, whereas in all other kingdoms of life, the protein is essential [126].

Group I and II introns are self-splicing ribozymes that excise themselves from precursor RNAs and ligate the flanking exons to yield mature RNAs. Group I introns reside in pre-mRNAs, rRNAs and tRNAs of a great diversity of organisms. They have an average length of 400 nt and share a characteristic secondary structure (Figure 3.6c). The splicing reaction requires an exogenous GTP and Mg^{2+} and proceeds in two steps [8, 9]. First, the intron binds the 5'-exon and the GTP containing the nucleophilic 3'-OH group. The activated 3'-OH attacks the phosphodiester between the 5'-exon and the intron, cleaving this bond and releasing the 5'-exon. In the second step, the liberated 3'-OH of the 5'-exon attacks the phosphodiester bridge linking the 3'-terminal guanosine of the intron with the 3'-exon: The two exons are joined and the intron is released in a linear form [with an additional G at the 5'-end].

Group II introns (Figure 3.6d, see also Chapter 4) are found in bacterial DNA and in the genomes of eukaryotic organelles. Their splicing mechanism [128–130] (Figure 3.5b) differs from group I introns as they do not require an exogenous GTP as cofactor. The 2'-OH of a conserved so-called branch point adenosine within the intron provides the attacking nucleophile for the first step of splicing. Consequently, upon joining the flanking exons, the intron is released as a lariat. Both group I and II introns can contain sequences encoding proteins that enable them to reinsert into RNA or DNA [131]. This allows them to change their location and spread in the genome as mobile genetic elements; a process that normally is neither harmful nor beneficial to the host organism. The removal of non-self-splicing introns from precursor-mRNAs is catalyzed by the spliceosome in eukaryotes. The spliceosome is a huge and complex assembly of five RNAs and dozens of

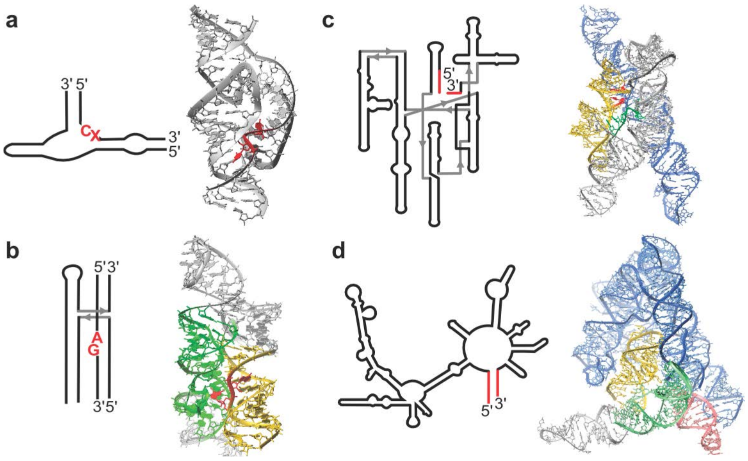

Figure 3.6: Secondary and 3D structure of two small and two large ribozymes. (a) the hammerhead ribozyme (pdb ID: 2GOZ [105]) (b) the hairpin ribozyme (pdb ID: 1M5K [110]) (c) the group I intron (pdb ID: 3BO2, [127]) (d) the group II intron (pdb ID: 3BWP [36]) In (a) and (b) the nucleotides, which are disjoined during self-cleavage, are colored red; in (b) and (d) the exons are colored red (see also Figure 3.5).

proteins. The details of its structure and catalytic mechanism remain largely obscure. The spliceosomal RNA U6 resembles the catalytically active moiety of group II introns in structure and sequence. In addition, the splicing in both ribozymes proceeds in a very similar manner [132–134] (Figure 3.5b). Hence, the spliceosome is considered an evolutionary descendant of group II introns with splicing being indeed RNA-catalyzed [135–138].

Another large cellular machinery, the ribosome, is a peptidyl transferase. This large ribonucleoprotein complex catalyzes the formation of peptide bonds during protein translation. Although the exact catalytic mechanism of the ribosome is not yet fully characterized, the fact that the active site consists of RNA exclusively and is located at a distance of 18 Å from any of the ribosomal proteins [139] strongly suggests that the ribosome is indeed a ribozyme [140, 141]." [24]

3.6.3 Reactions catalyzed by ribozymes

"Apart from the ribosome all natural ribozymes catalyze phosphoryltransfer reactions, which means that one phosphodiester bond is broken to form another one by a nucleophilic substitution. Small ribozymes are 5'-OH displacement ribozymes, whereas group I and II introns, RNase P and the spliceosome are classified as 3'-OH displacement ribozymes (Figure 3.7). In the small ribozymes, the phosphodiester bond is cleaved by nucleophilic attack from the 2'-OH of the adjacent upstream nucleotide. Large ribozymes form complex active sites and use an exogenous group for the nucleophilic attack. These exogenous groups can be water (RNase P [142, 143], group II introns [144]), an OH group of a mononucleotide or of an internal nucleotide sequentially distant from the cleavage site (group I [8]

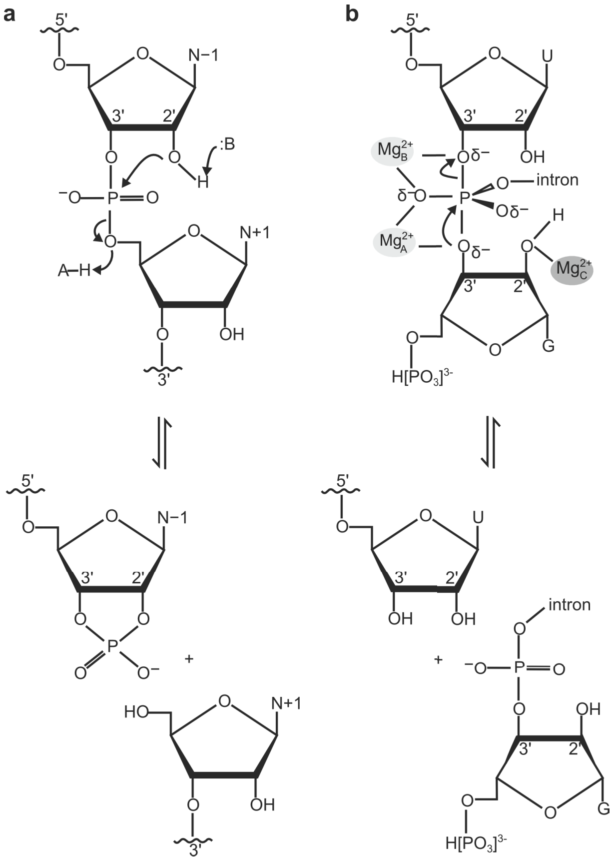

Figure 3.7: Mechanisms of ribozyme catalysis. (a) Acid-base catalysis as observed in the hairpin ribozyme: :B is a general base that abstracts a proton from the 3'-OH group to activate it as a nucleophile. A—H is a general acid that stabilizes the leaving group by donating a proton. As a consequence of the 2'-OH attack on the adjacent phosphodiester, a 2',3'-cyclic phosphate and a 5'-hydroxyl terminus are formed. (b) Metal ion-assisted catalysis. A typical two-metal-ion mechanism using the example of the first step of group I intron splicing is shown. In this case all metal ions are Mg^{2+}. The two metal ions that directly participate in catalysis are Mg_A^{2+}, which can bind OH^- ions in solution accepting the proton from the OH nucleophile as a general base and Mg_B^{2+}, accepting electrons from the 3'-oxyanion of the intron thereby stabilizing the same as a leaving group. A third metal ion Mg_C^{2+} additionally stabilizes the transition state by coordinating the 2'-OH of GTP. Strand cleavage results in a free 3'-hydroxyl group and a new phosphodiester bridge (group I and II introns, spliceosome) or a free phosphate in the case of RNase P. The figure and legend were taken from [24].

& II [128, 129] introns, spliceosome [145, 146]), or the amine of the amino acid to be added to a growing peptide chain (ribosome [147])." [24]
By *in vitro* selection techniques, artificial ribozymes and also DNAzymes have been developed for acylation and alkylation reactions as well as for the formation of carbon-carbon and glycosidic bonds [148]. This proves that the catalytic repertoire of nucleic acids is in principle much wider than suggested by the naturally existing ribozymes.

3.7 Toolbox - studying ribozyme structures and metal ion binding sites

3.7.1 NMR-based structure determination of nucleic acids

NMR and crystallography are the principal techniques for biomolecular structure determination at the atomic level. NMR has some advantages over crystallography: as the molecule of interest only needs to be dissolved in a salt or buffer solution, the experimental conditions are much closer to the physiological situation than in crystallography. Furthermore, NMR makes it possible to study both structure and dynamics in one sample. The main disadvantage of NMR is the molecular size limit, up to which the technique can be applied. This is due to the line width of the NMR signal being proportional to the rotational correlation time. Although various technical advances such as three (or higher)-dimensional NMR spectroscopy [149]; transverse relaxation optimized spectroscopy [150–152] used to obtain sharper lines in heteronuclear correlation spectra; and the use of residual dipolar couplings (RDCs) [153, 154] for structure calculation (see below) have pushed the size boundary, nucleic acid NMR is still tied to a rather narrow size range. The vast majority of RNA structures solved contain no more than 50 nt.

The reasons for this are the low overall proton density in nucleic acids and the limited chemical variation among their building blocks (Figure 3.1b). Compared to proteins, which consist of 20 chemically diverse amino acids, nucleic acids are permutations of only 4 nucleotides being rather similar to each other. The chemical similarity of the nucleotides confines the chemical shifts of their protons to rather narrow spectral ranges of 3-9 ppm in RNA and 1-9 ppm in DNA for the nonexchangeable protons and 6-15 ppm for the exchangeable protons. Mainly the ribose protons H3', H4', H5' and H5" fall in a very narrow spectral region (3-5 ppm) and are thus subject to overlap, that compounds with the number of nucleotides. To overcome this problem, segmental labeling techniques for big RNAs are a very promising approach and have recently been applied with success to larger nucleic acids [155, 156]. Recently, also the combination of RDCs and small angle X-ray scattering data has been used for structure determination of larger RNAs [79].

Classical NMR-structure determination of nucleic acids is based on three types of restraints: short-range interproton distances, assessed by the Nuclear Overhauser Effect (NOE); selected torsion angles of the nucleotides, that are mainly studied by scalar couplings between nuclei; and long-range information on the relative orientation of different molecular regions, provided by RDCs [153, 154]. The latter are mostly important for studying larger and more complex nucleic acids. Such restraints are combined with universally valid parameters on bond geometries and non-bonded contacts to create an input set for energy-minimization algorithms. Such algorithms use for example molecular dynamics, Monte Carlo methods or gradient-based minimization to determine the conformers of lowest possible energy that satisfy the input set [157–160]. The three NMR parameters used to obtain a restraint set will be briefly introduced in the following.

The NOE is a through-space polarization transfer between two spins. Such a transfer leads to a change in signal intensity of, for example, a proton that obtains magnetization from another nearby proton, which was originally excited. The NOE is proportional to $\frac{1}{r^6}$, confining it to proton pairs that are no more than 7 Å apart. Accordingly, the NOE is of paramount importance for defining local structure (Figure 3.8c) but less useful for establishing spatial relations in large molecules. The distances reported by the NOE can also be used to infer other structural parameters, one example is the glycosidic angle χ, which is related to the distance between H1' and H6/8 in a nucleotide. A very intense H1'-H6/8 NOE cross peak usually indicates *syn* conformation (Figure 3.8a).

The *J* coupling exists between covalently linked nuclei and is mediated by the bonding electrons. It gives rise to the multiplicity of an NMR signal. Its magnitude depends on the gyromagnetic ratios of the coupled nuclei, the number of bonds that connect them and, in case of the vicinal or ^3J coupling (across three bonds), on the dihedral angles between the coupled nuclei. The latter phenomenon is known as the Karplus relation and is exceptionally useful for structure determination. For example, the ^3J coupling constant between H1’ and H2’ is helpful for the identification of the sugar pucker (Figure 3.8b). Scalar $^2J_{NN}$ couplings also occur across the hydrogen bonds in base pairs (blue arrow in Figure 3.8d) and therefore serve as a direct reporter of base pair formation [161].

RDCs depend on the angle between a bond vector and the magnetic field as well as on the gyromagnetic ratio of the bound nuclei and their distance. In solution, these couplings average to zero due to the overall tumbling of the molecule. Thus, to make use of the RDCs, a certain degree of molecular order has to be introduced, for example by adding large, homogeneously shaped particles to the NMR sample that are able to auto-align in the magnetic field. As RDCs relate the internuclear vectors to a common coordinate system, they provide orientational restraints for separate domains or remote regions of a macromolecule. For example, they have been used to identify the overall bend of a nucleic acid helix axis [162].

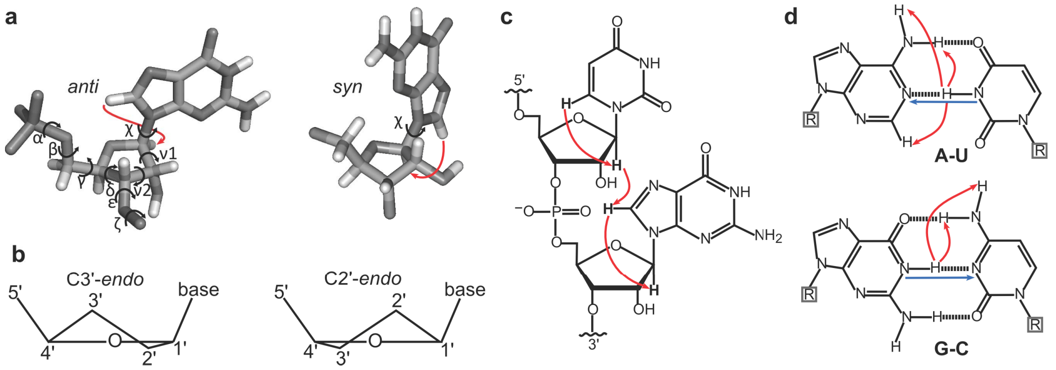

Figure 3.8: RNA conformational parameters accessible by NMR. (a) Torsion angles of the sugar-phosphate backbone (α, β, γ, δ, ϵ, ζ), of the sugar (δ, $\nu 1$, $\nu 2$) and glycosidic bond-torsion angle (χ). The nucleotide is shown in *anti* and *syn* conformation, where χ=180/0°, respectively. (b) Schematic representation of a C3’-*endo* and C2’-*endo* sugar pucker; (c-d) Important NOE correlations for proton assignment: (c) the H1’-H6/8 sequential walk and (d) correlations across the base pairs. The blue arrow links the atoms related by the $^2J_{\mathrm{NN}}$ coupling mentioned in the text. Arrows indicate the technically most convenient direction for making assignments.

3.7.2 NMR resonance assignment

The assignment of proton resonances, and selected carbon and nitrogen resonances is essential for any NMR-based structural or metal ion binding study. A proton assignment is usually done starting from the so-called sequential walk. The term denotes a regular distance pattern between the H1’ protons of a nucleotide and its own H6 or H8 and the H6/8 of the next nucleotide (Figure 3.8c). Both the intraresidue and interresidue H1’-H6/H8 distance falls between 3 and 5 Å in both A-form and B-form duplexes. Accordingly, the corresponding NOEs can be traced from one nucleotide to another from the 5’ to the 3’-end. Depending on local geometry and flexibility, this may even be possible in loops or bulges. In a very similar fashion, H2'(H2")-H6/8 correlations can be used for a sequential assignment.

With the sequential walk as a starting point, it is often possible to assign the majority of the non-exchangeable protons H1', H2', (H2"), H3', H4', H2, H5, H6, H8 and sometimes H5' and H5" (Figure 3.1). Among these, H2 of adenine has special significance both for the assignment and for structure calculation, as it is facing the helix center and thus usually has correlations to protons of the opposite strand.

The assignment of the exchangeable protons is done by a quite different approach. It mainly relies on identifying sequential correlations of uracil H3 and guanine H1 either across strands or within one strand and on characteristic NOEs within a base pair such as GH1-CH41/42 or UH3-AH2 (Figure 3.8d).

Samples transcribed from isotope-labeled nucleotides are of great help and, in larger molecules, usually essential for the assignment of the proton resonances. Carbon and nitrogen assignments are obtained from $^{13}C,^{15}N$-labeled samples, since the naturally most abundant ^{12}C and ^{14}N isotopes are no spin $\frac{1}{2}$ nuclei and thus not suitable for high-resolution NMR spectroscopy. The attributions of $[^1H,^{15}N]$ and $[^1H,^{13}C]$ correlations can be pivotal for the identification of the position of a proton by the characteristic chemical shift ranges of the attached carbon or nitrogen nucleus. For example, C5 (uracil, cytosine), C2 (adenine), N1 (guanine), N3 (uracil) and of C1' and C2' of the riboses (Figure 3.1) have rather characteristic chemical shift ranges. Furthermore, heteronuclear filtering and editing pulse sequences [163] can be applied to complexes of $^{13}C,^{15}N$-labeled and natural abundance molecules. Such pulse sequences are highly useful as they can select for, for example, NOE correlations that are intramolecular (between protons bound to the same N/C isotope) or intermolecular (between protons bound to different N/C isotopes). Partially deuterated nucleotides are often used to erase the H3', H4', H5' and H5" resonances from the NOESY or TOCSY spectrum and therefore allow to specifically assign H2' resonances, which would otherwise be overlapped. Apart from the spectral simplification thus achieved, the lower number of protons in such samples also means fewer sources of spin-spin relaxation and thus results in sharper lines; a highly desirable effect for the spectra of larger RNAs (Section 5.4). Finally, selective labeling approaches are often useful to discriminate protons belonging to one of the four nucleotides.

3.7.3 Nucleic acid complex formation investigated by SPR

In this work, surface plasmon resonance (SPR) is used to investigate the kinetics of the association and dissociation of the two strands of a nucleic acid duplex (Section 4.3.3). SPR is an optical technique well-established for studying the kinetics of biomolecular binding events in aqueous solution and has been widely applied to protein-protein, protein-nucleic acid and protein-small molecule interactions. Beyond measuring affinities and on- and off-rates, it can also be used to determine thermodynamic parameters, the activation energy and the stoichiometry of complex formation.

The SPR instrument measures the change in refractive index (RI) near a sensor surface, on which a biomolecule of interest (the ligand) is immobilized. Another molecule, whose interaction with the ligand is to be studied (the analyte) is injected in the flow cell con-

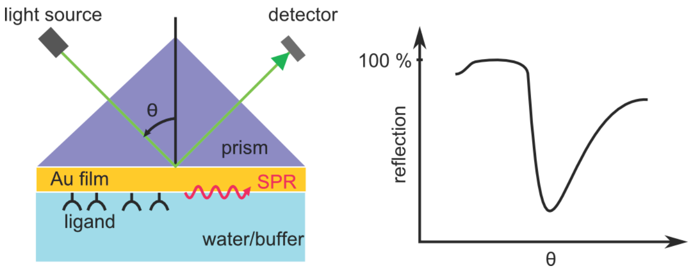

Figure 3.9: Working principle of the SPR experiment (see text for further explanation). The figure was adapted from http://www.bionavis.com/technology/spr/.

taining the sensor surface. Binding of the analyte to the ligand changes the mass on the sensor surface, which is detected in real-time as a change in RI and recorded in the form of a sensorgram [164–166] (Figure 4.6).

Surface Plasmons are electromagnetic waves propagating along a thin metal film [167]. They arise upon total internal reflection of a light beam at the interface of a low RI medium (aqueous buffer) with a high RI medium (glass), where the glass is coated with the gold (or other noble metal) film (Figure 3.9). At a given angle θ, excitation of the surface plasmons occurs using energy from the light beam. Reflection is thus not total any more as the reflected light has now lower intensity than the incident light [168, 169] (Figure 3.9). The angle, which fulfills the resonance condition is highly sensitive to the RI of the medium, for this reason, the intensity of the reflected light beam reports on mass changes on the surface.

3.7.4 Studying metal ion binding to nucleic acids

Although there is today a whole arsenal of techniques to localize metal ion binding sites in nucleic acids, the exact description of a binding site remains a challenge, as the physiologically most relevant ions, K^+ and Mg^{2+}, have generally low affinity and lack easily exploitable spectroscopic properties. Different surrogate metal ions, which bind with higher affinity and are luminescent or NMR-observable, have been used but often the surrogate does not bind to the nucleic acid in exactly the same way as K^+ or Mg^{2+}. For this reason, it is usually helpful to combine experiments with different metal ions or to employ several experimental techniques to identify the most probable binding sites.

Biochemical methods to study metal ion binding include hydrolytic cleavage studies, in which Mg^{2+}, Pb^{2+} or Tb^{3+} (Section 5.6.4) are added to stimulate self-cleavage of the RNA sugar-phosphate backbone next to their binding sites [170–172]. Using fluorescently labeled or radiolabeled RNA, the generated fragments can easily be separated and imaged in polyacrylamide gels. Nucleotide Analogue Interference Mapping (NAIM) [173–176] is another powerful technique to identify nucleotides and functional groups relevant for metal ion binding or other functions. The RNA is transcribed in the presence of different phosphorothioate nucleotide analogues that are randomly incorporated during transcription. Thereby, on average, no more than one modification per molecule is obtained. The resulting sequence pool is screened for catalytic activity or another property of interest and then treated with iodine, which promotes site-specific cleavage at the modified nucleotide.

The depletion of a certain fragment in the active pool of sequences corresponds to a nucleotide, which is critical for function. The most common experiment that uses NAIM for identifying functionally relevant metal ion binding sites is the so-called metal ion-rescue experiment [177]. Introduction of the phosphorothioate abolishes Mg^{2+} binding to the backbone of this nucleotide, as sulfur ligands are disfavored by Mg^{2+} compared to oxygen. If the binding site in question is relevant for activity, activity is decreased but can be restored by adding a thiophilic metal ion such as Cd^{2+} or Mn^{2+}.
Furthermore, other spectroscopic techniques such as EPR, Infrared and Raman spectroscopy can be exploited for metal ion binding studies.

NMR -based characterization of metal ion binding sites mostly relies on studying the impact of metal ion addition on certain NMR parameters such as the chemical shift, the line width or a *J*-coupling. A direct detection is far more difficult as all stable metal isotopes, which are relevant for nucleic acid biochemistry are either not NMR active ($^{24}Mg^{2+}$) or quadrupolar ($^{23}Na^{+}$, $^{25}Mg^{2+}$, $^{39}K^{+}$, $^{41}K^{+}$) and thus displaying broad lines.
$^{205}Tl^{+}$ and $^{107/109}Ag^{+}$ have successfully been used to directly observe several metal resonances corresponding to different nucleic acid binding sites [178]; or to measure couplings between the metal and a nucleic acid proton [178], or nucleic acid nitrogen [179], respectively. Such experiments, however, are restricted to a low number of sites where metal ions bind with high affinity and are not in fast exchange [77]. Line-shape analysis of the resonance of $^{25}Mg^{2+}$ weakly bound to a tRNA was used for measuring the metal-RNA association constant and the exchange rate of the metal in its binding sites [80].
Indirect detection of metal ion binding by NMR, as used in this thesis, can also be applied to low-affinity binding sites. The most common method is mapping perturbations of the chemical shift of ^{1}H, ^{15}N and – less frequently –^{31}P and ^{13}C, induced by different metal ions such as Mg^{2+} or Cd^{2+}. Line broadening effects caused by paramagnetic metal ions such as Mn^{2+}, Ni^{2+} or Co^{2+} [180, 181] and measurements of NOEs between nucleic acid protons and substitutes, such as $[Co(NH_3)_6]^{3+}$ replacing $[Mg(H_2O)_6]^{2+}$ [182, 183] or $NH_4{}^{+}$ replacing K^{+} [184], are also being used.
In some cases, such indirect detection methods yield information beyond the position of the binding site. For example, it may be possible to determine the affinity of a metal ion for a specific site from the progressive chemical shift changes [185]. By ^{15}N chemical shift mapping, the mode of metal ion nucleic acid interaction may be revealed. For example, a large chemical shift change of N7 upon metal addition is a good indicator of an inner-sphere contact [186]. In some cases, metal ion binding may actually alter the nucleic acid conformation in a way that measurable changes of certain NOE intensities or J-couplings occur, from which the nature of the resulting structure can be inferred.

4 EBS1·dIBS1 of a group IIB intron[1]

4.1 Introduction

Group II introns are large ribozymes and mobile genetic elements capable of catalyzing their own splicing reaction [128–130]. During splicing, the intron RNA excises itself from an RNA transcript in two sequential phosphotransesterification reactions that yield the two ligated exons and the excised intron in a lariat structure. Both steps of splicing are reversible, which enables the intron to reinsert into intronless sites on RNA or DNA, a process which is referred to as reverse splicing or retrohoming, if genomic DNA is the target of reinsertion [131, 187–190]. The most extensively studied example of the retrohoming pathway is the one of the *Lactococcus Lactis Ll.*LtrB group IIA intron, which requires an intron-encoded protein (IEP) [191, 192] encoded in an open reading frame in domain IV of the intron. During retrohoming, the IEP unwinds the DNA locally to allow hybridization of the spliced lariat intron RNA and the target DNA. The intron catalyzes the reverse splicing by cleaving the target strand and ligating its own termini to the flanking DNA. The opposite strand is cleaved by the IEP endonuclease domain and the reverse transcriptase domain of the IEP transcribes the complementary cDNA from the intron RNA template. The removal of the RNA and the synthesis and ligation of the DNA, which replaces it, are catalyzed by host proteins and complete the insertion process. As mobile genetic elements, group II introns resemble non-LTR retrotransposons [193] and they perform splicing in a way very similar as the eukaryotic spliceosome [135, 194]. These parallels gave rise to the idea that group II introns might be ancestors of both the spliceosome and non-LTR retroelements, suggesting pivotal evolutionary importance of group II introns for the shaping of eukaryotic genomes [195, 196].

In both splicing and reverse splicing, exon-intron recognition is mediated by base pair formation between the exon binding sites (EBS) of the intron and the corresponding intron binding sites (IBS) on the exons [197]. In the case of group IIB introns, there are three such contacts. EBS1 (with 5-7 nt the longest of the three sequences) and EBS2 bind the 5'-exon [198], whereas EBS3 forms a single base pair with the 3'-exon (Figure 4.1a and c). Additionally, another base pair within the intron, the so-called δ-δ' interaction helps to stabilize the intron-exon contacts by positioning the sequentially distant EBS1 and EBS3 close to each other [199, 200] (Figure 4.1c). The EBS1·IBS1 interaction confers high specificity to the site of reinsertion of the intron, thus preventing insertion into sites from which the intron cannot splice again. However, it has been shown that EBS sequences are not conserved within different group II introns [198, 201, 202]. For this reason, any desired sequence can be bound and cleaved by the intron in *trans* as long as the EBS and IBS se-

---

[1] All text, tables and figures are reproduced from [25]

quences are complementary [203–206]. This characteristic endows group II introns with a remarkable potential for gene therapy applications [207].

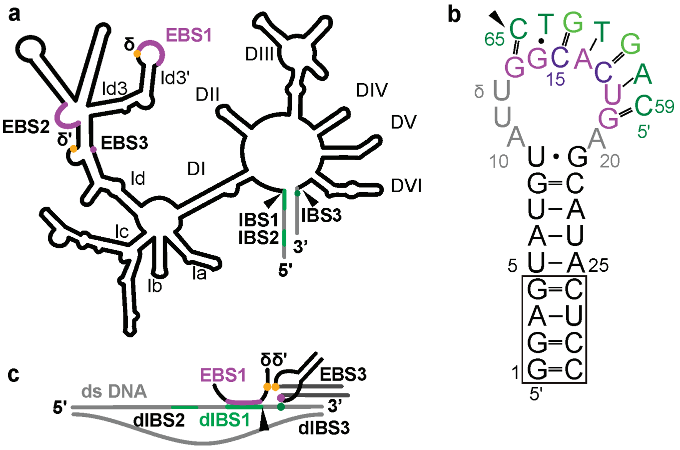

Figure 4.1: Location and secondary structure of EBS1 and dIBS1. (a) Scheme of the proposed secondary structure of a group IIB intron. Base pairs between EBS1-3 (purple) and exonic IBS1-3 (green) as well as the δ and δ' bases (orange) mediate correct recognition of the 5'- and 3'-exon both in splicing and reverse splicing events. The six domains of the intron (DI-DVI) and the four main branches of DI (Ia-Id) are labeled. Sites of intron-catalyzed cleavage are marked with black arrows. (b) d3'EBS1·dIBS1, the RNA·DNA hybrid construct used in this study. The sequences of nucleotide 5-25 of the RNA (d3'EBS1) containing EBS1 (purple) and of dIBS1 DNA (green) are derived from the *Sc*.ai5γ intron found in the *cox1* gene of *S. cerevisiae* mitochondria. The base pairs marked with light green/dark purple letters were mutated from A-T to G-C for the sake of stability [208]. The nucleotides 1-4 and 26-29 (boxed) are added to the wild type sequence. (c) The spatial arrangement of the EBS·dIBS and δ-δ' base pairs ensures binding of both exons in the correct orientation for cleavage. Interactions are exemplified for a double-stranded DNA target (gray).

Group II introns consist of six domains (DI-DVI) radiating from a central wheel (Figure 4.1a). DI, containing the EBS sequences, is the largest and constitutes an autonomous folding entity to which other domains dock in the folding process [209–211]. Together with DV it forms the minimal structure required for catalytic activity of the intron [212, 213]. Mg^{2+} ions play a critical role for both structure and function of group II introns and large ribozymes in general [58, 85, 214, 215]. Formation of a stable tertiary structure of the group II intron is dependent on the presence of divalent metal ions [49, 210, 216]. Moreover, several metal ion binding sites have been located in the active site [217–219] and a two-metal ion mechanism [220, 221] has been suggested to underlie intron catalysis [222, 223]. In-cell studies establishing a correlation between the intracellular Mg^{2+} concentration and the frequency of splicing and retrohoming buttress the relevance of Mg^{2+} for group II intron catalysis [224–227]. The importance of the identity of the divalent metal ions bound to the intron is underscored by the finding that the presence of Mn^{2+} can lead to a shift of the cleavage site [228] and that already low amounts of Ca^{2+} decrease the turnover rate by 50 % in the Sc.ai5γ intron [229].

Although a wealth of genetic and biochemical investigations have shed light on group II intron function, the information on tertiary structure is sparse. The group IIC intron of *Oceanobacillus iheyensis* is the only entire group II intron for which crystal structures are published [36, 79, 223, 230, 231].
In this paper, we present the first structure of the complex between the d3'EBS1 hairpin and the dIBS1 DNA, using EBS1·dIBS1 of the intron Sc.ai5γ, found in mitochondrial transcripts of *S. cerevisiae*, as a model construct. We focus on a detailed analysis of the metal ion binding properties of the complex as determined by NMR spectroscopy and Surface Plasmon Resonance (SPR). As the same catalytic mechanism underlies intron-catalyzed DNA and RNA cleavage, we compare our data to the structure and metal ion binding of the analogous d3'EBS1·IBS1 homoduplex construct [23] and discuss common features relevant for stable binding of the target and for the recognition of the cleavage site.

4.2 The NMR construct

In d3'EBS1·dIBS1 (Figure 4.1b), nucleotides 5-25 of the hairpin correspond to the sequence of the d3' hairpin from DI of the *Sc*.ai5γ group II intron (Figure 4.2a and b) except for nucleotides 15 and 17 in EBS1, which are adenines in the wild type sequence. In order to have a suitable starting sequence for *in vitro* transcription [232] and a more stable hairpin stem, four base pairs were added to the stem (box in Figure 4.2b). The dIBS1 sequence is a deoxyribonucleotide 7mer corresponding to the wild type sequence of dIBS1 except for T-to-G mutations in position 61 and 63 matching the mutations of EBS1. The resulting G·C base pairs are required to achieve a stable enough duplex formation for NMR investigation (Table 4.3, see also references [23, 208].

4.3 Results

4.3.1 Characterization of dIBS1 binding to EBS1 by NMR spectroscopy

To verify stable formation of the EBS1·dIBS1 hybrid, we used [^{1}H,^{1}H]-NOESY spectra recorded in H_2O (Figure 4.2a). When d3'EBS1 or dIBS1 are measured separately in solution, the imino protons of the recognition sequences (G13, G14, U18 and G19 of EBS1 and of G61, T62, G63 and T64 of dIBS1) cannot be observed as these regions are largely unstructured, and the protons exchange rapidly with the solvent. The presence of resonances for each of these protons (colored labels in Figure 4.2a) and of cross peaks within and between EBS1 and dIBS1 is a clear indication that EBS1 and dIBS1 are indeed fully base paired. Each imino proton in the d3' stem can be attributed to one resonance (black labels in Figure 4.2a), their chemical shifts being very similar to the ones observed for the unbound d3'EBS1 [23] proving that addition of dIBS1 does not interfere with the base pairing in the stem.
Sequence-specific assignment of the resonances of the nonexchangeable d3'EBS1 and dIBS1 protons was accomplished using standard [^{1}H,^{1}H]-NOESY spectra and F1,F2-[^{13}C,^{15}N]-filtered NOESY spectra [163] (Figure 4.2b and Appendix 7.1). The chemical shifts of protons from the RNA stem are in excellent accordance with previously published ones

for unbound d3'EBS1 [23]. The sequential cross peaks between U12 in the loop and G13 and G14 in EBS1 are very low in intensity (Appendix 7.1), probably due to an unusual geometry at residue G13. The remaining loop residues display typical spectral features of an A-form RNA except for A10-U12, whose ribose moieties are in C2'-*endo* conformation according to the [^{1}H,^{1}H]-TOCSY data (Figure 4.4b).

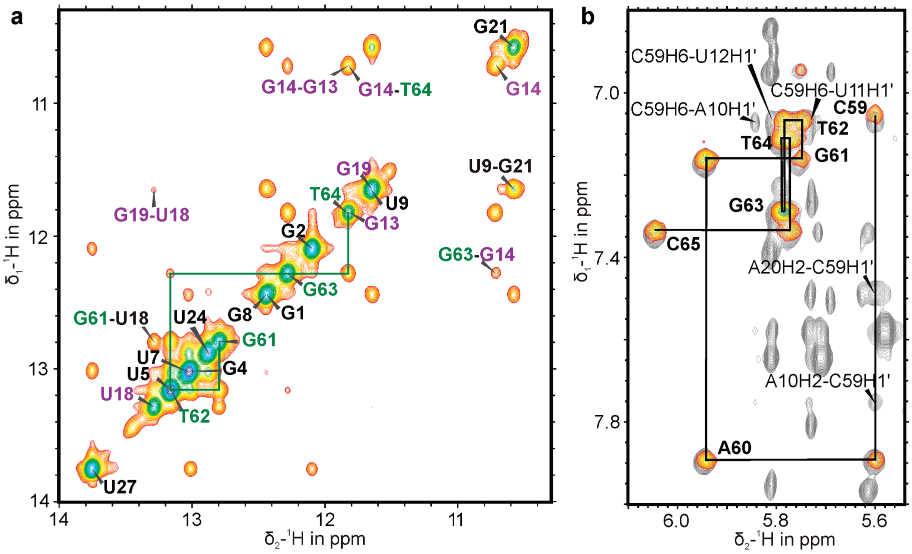

Figure 4.2: dIBS1 adopts a helical structure upon binding to EBS1. (a) [^{1}H,^{1}H]-NOESY of the exchangeable (imino) protons (5 °C, 110 mM KCl, 10 μM EDTA, in H_2O, pH 6.8). Presence of diagonal peaks for all G,T and U residues in the EBS1·dIBS1 helix and cross peaks between neighboring dIBS1 residues (connected by green lines) and between EBS1 and IBS1 residues prove base pair formation between the two strands. (b) Superposition of the F1,F2-[^{13}C,^{15}N]-filtered [^{1}H,^{1}H]-NOESY (colored) containing only peaks of IBS1 protons and the normal [^{1}H,^{1}H]-NOESY (gray) (both: 25 °C, 110 mM KCl, 10 μM EDTA, in D_2O, pD 6.8). Intense sequential cross peaks between dIBS1 residues (labeled in boldface and connected by lines) indicate that dIBS1 assumes a stable fold. Cross peaks between proton resonances of dIBS1 C59 and EBS1 proton resonances are labeled.

For dIBS1, the cross peak intensity pattern in the [^{1}H,^{1}H]-NOESY and [^{1}H,^{1}H]-TOCSY (Figures 4.3 and 4.4) reveals an unusual geometry of the DNA strand. In the [^{1}H,^{1}H]-TOCSY all dIBS1 nucleotides, except for C65, which displays the C3'-*endo* cross peak pattern, display cross peaks of intermediate intensity for both the H1'-H2' correlation and the H3'-H4' correlation, which is atypical for a pure C3'-*endo* or C2'-*endo* conformation. This can signify either conformational flexibility of the deoxyribose rings or a rare O4'-*endo* conformation. The latter however is associated with a very short H1'-H4' distance (2 Å) [157], which the NOESY data only suggest for T62 and T64 (data not shown). Additionally, the intensity difference between the H2'-H6/8 and the H2"-H6/H8 NOESY cross peaks (Figure 4.3) and a systematically higher $J_{1'2'}$ than $J_{1'2"}$ coupling characteristic for B-form DNA are not observed. It is thus clear that the DNA neither adopts the A-form of its EBS1 binding partner nor B-form geometry, which is the preferred one of DNA. Additionally, the rather broad

DNA cross peaks suggest conformational exchange within dIBS1 (Figure 4.3).

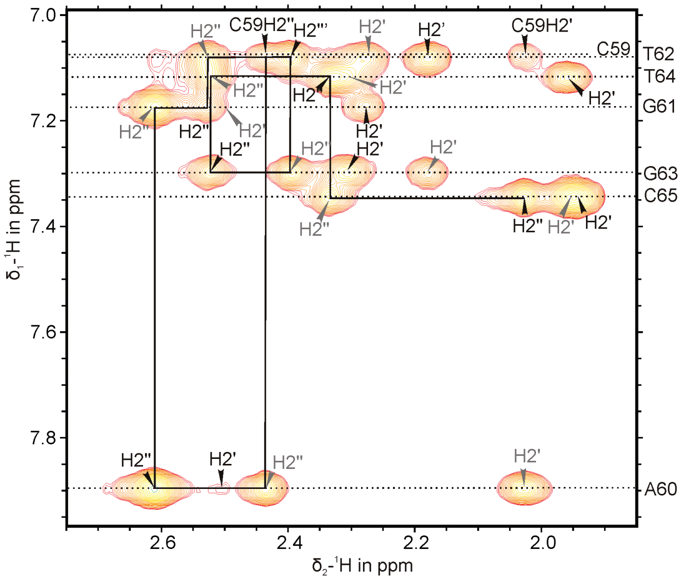

Figure 4.3: [^{1}H,^{1}H]-NOESY spectrum of d3'EBS1·dIBS1 showing cross peaks between H2'/H2" and H6/H8 protons of dIBS1. On the right, the residue of the H6/H8 resonance is indicated. The intraresidue cross peaks are labeled in black, the interresidue cross peaks are labeled in gray. The sequential walk of intra- and inter-residue H2"-H6/8 cross peaks is shown as a black line. In a standard B-form conformation cross-peak pattern, the H2'(i)-H6/8(i) (intraresidue) cross peak is more intense than the H2"(i)-H6/8(i) cross peak whereas the H2"(i-1)-H6/8(i) (interresidue) cross peak is more intense than H2'(i-1)-H6/8(i). The fact that no such pattern is observed rules out a stable B-form conformation of the DNA and the rather broad appearance of the peaks points out flexibility of dIBS1. The spectrum was recorded in D_2O at 25 °C (110 mM KCl, 10 µM EDTA, pD 6.8).

4.3.2 The solution structure

The ensemble of the 18 d3'EBS1·dIBS1 conformers (Figure 4.5a) of lowest energy shows good convergence of the heavy atoms, represented by the low overall root mean square deviation (RMSD) of 1.00 Å (Table 4.1). In the short helix formed by dIBS1 and EBS1 (Figure 4.5b), the backbone trajectory of the dIBS1 strand varies. The stem, which is a regular A-form helix and the EBS1·dIBS1 helix are nearly parallel to each other but slightly shifted in all 18 conformers. This shift is due to the uneven number of unpaired bases on the 5'- and 3'-side of EBS1 (see A10, U11, U12 and A20 in Figure 4.5d). A20 on the 3'-end of the loop forms a bridge between the stem and the EBS1·dIBS1 helix by stacking in between their terminal base pairs C59·G19 and U9·G21. Opposite of A20, A10 on the 5'-end of the loop is stacked on U9, and in some conformers U11 and U12 also display stacking interactions (Figure 4.5d). In this arrangement, it is probable that hydrogen bond formation between A10N61 and A20N1 further stabilizes the structure. The single-stranded nucleotides not

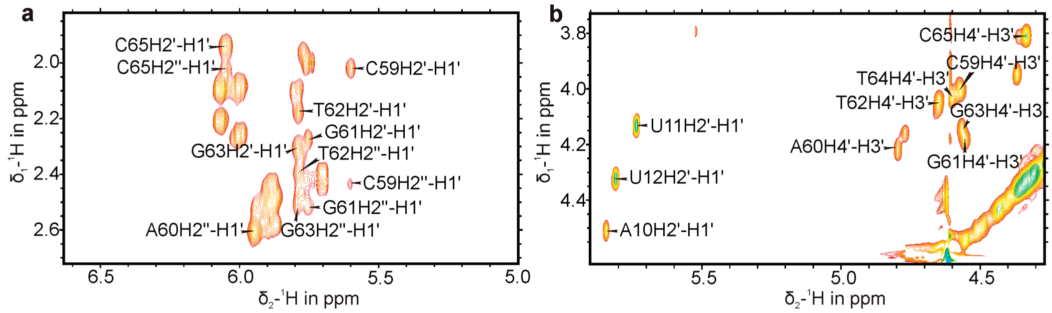

Figure 4.4: Sugar proton region of a [^{1}H,^{1}H]-TOCSY spectrum of d3'EBS1·dIBS1. (a) H1'-H2'/H2" cross peaks of dIBS1 nucleotides. (b) H1'-H2' cross peaks of A10-U12 and H3'-H4' cross peaks of dIBS1. An intense H3'-H4' and a weak or absent H1'-H2' cross peak indicates a C3'-*endo* sugar pucker, found in A-form DNA and RNA while the opposite situation is characteristic of a C2'-*endo* pucker typical for B-DNA. All H3'-H4' cross peaks belonging to dIBS1, have similar and intermediate intensities except for C65H4'-H3', which is more intense, pointing out a C3'-*endo* conformation. For comparison, the very intense H2'-H1' cross peaks of A10, U11 and U12 corresponding to a C2'-*endo* conformation are shown, other RNA H2'-H1' cross peaks that would be located in this spectral region are invisible due to the stem nucleotides having regular C3'-*endo* sugar pucker. The spectrum was recorded on a sample containing partially deuterated d3'EBS1 and natural abundance dIBS1 D_2O at 25 °C (110 mM KCl, 10 µM EDTA, pD 6.8).

only stabilize the junction between the d3' stem and EBS1·dIBS1 but also seem to fix the position of the 5'-end of dIBS1. The observation of several cross peaks between protons of C59, the 5'-terminal nucleotide of dIBS1, and A10, U11, U12 and A20 (Figure 4.2b) agree well with the position of C59, which is placed in between A10 and U11 or U12 at the 5'-end of the loop and A20 on the 3'-end (Figure 4.5d).

In contrast to C59, C65, where cleavage occurs, is in an exposed position. Between U12 and G13 of EBS1, a sharp turn or kink changes the direction of the RNA backbone (Figure 4.5c). This kink moves the bases of G13 and U12 far apart so that stacking interactions are only possible between G13 and G14. This explains why NOE correlations between U12H1' and G13H8 are extremely weak if observed at all (Appendix 7.1) because both protons are separated by a distance greater than 6 Å.

4.3.3 The variable non-standard conformations of EBS1·dIBS1 cause its low stability.

Since it was evident from TOCSY and NOESY spectra that dIBS1 does not assume any standard helical conformation and seems to be subject to conformational exchange, we evaluated more closely the geometry of EBS1 and dIBS1 in the hybrid duplex in five of the 18 lowest energy structures with visibly different backbone trajectories on the side of dIBS1 (Figure 4.5b), representing possible fits to the NOE data. Importantly, no dihedral angle restraints limiting the sugar pucker of the dIBS1 nucleotides were included in the calculation. As RNA is conformationally less tolerant than DNA, the geometries of hybrid duplexes are usually reported to be more similar to A-form [233–235]. In agreement with

Table 4.1: NMR experimental restraints and refinement statistics for the 18 lowest energy structures of d3'EBS1·dIBS1 out of 200 calculated structures.

NOE distance restraints	733
~ intraresidue $(j-i=0)$	240
~ interresidue $(k-i=1)$	351
~ long-range $(n-i>1)$	75
~ between EBS1 and dIBS1	67
~ within dIBS1	161
~ mean number per residue	20.4
hydrogen-bonding (base pair) restraints	82
dihedral angle restraints	247
~ mean number per residue	6.9
RDC restraints	21
violations	
distance > 0.2 Å	0
distance > 5°	0
RMSD of all heavy atoms vs. the mean structure in Å	
global	1.00±0.34
helical stem (residues 1-9, 21-29)	0.53±0.25
EBS1·dIBS1 (residues 13-19, 59-65)	0.60±0.17

this, the EBS1 strand adopts an A-form geometry even in control calculations, where only the α and ζ backbone angles are loosely restrained to the *trans* range, which is in line with the [^{1}H,^{1}H]-NOESY and [^{1}H,^{1}H]-TOCSY data. However, in contrast to EBS1, comparison of the backbone and sugar pucker-defining angles (Table 4.2) of dIBS1 to the standard angles found in A-form or B-form DNA proves that dIBS1 conforms to neither conformation in any analyzed trajectory. Another remarkable feature of the EBS1·dIBS1 duplex is the fact that all of the five conformers have a significantly narrower minor groove than major groove (14.8 Å vs. 16.4 Å on average), which is normally a feature of B-DNA. The deoxyribose rings of the different dIBS1 nucleotides have different sugar puckers and seem to be able to exchange between similar sugar puckers with the exception of T62 and G63 (O4'-*endo*) and C65 (C3'-*endo*), which have the same conformation in all analyzed structures (Table 4.2). This asymmetric structure of the EBS1·dIBS1 duplex adds a new variation to the continuum of helical conformations that can be observed for RNA·DNA helices, depending on the exact sequence and the distribution of purines and pyrimidines in each strand [236–238].

SPR experiments were performed to investigate the impact of the conformational heterogeneity on EBS1·dIBS1 stability. At 25 °C, in the absence of any divalent metal ions, the K_D of EBS1·dIBS1 is 29 ± 6 µM (Table 4.3). This value is at the upper limit of what can be accurately measured by the instrument and hence should be considered an estimate. For comparison, the K_D of the RNA·RNA duplex of EBS1·IBS1 is about 200 times lower (Table 4.3), due to the much lower dissociation rate of IBS1 RNA from EBS1. Given that

Table 4.2: Backbone torsion angles and pseudorotation angle of the EBS1 and dIBS1 residues. Values represent the average and standard deviation of five of the 18 lowest energy conformers of d3'EBS1·dIBS1 in degrees. While the backbone and ribose conformation within the EBS1 strand is typical for an A-form helix, dIBS1 is very weakly defined in its α, γ and ζ angles and δ, χ and P pseudorotation angles are at intermediate values between the averages of A-form and B-form.

	G13	G14	C15	A16	C17	U18	G19	average A-RNA
α	-	−72.1±0.1	−70.0±1.5	−65.9±2.6	−71.9±0.3	−58.4±1.0	−55.1±0.9	−62
β	−172.6±2.0	−171.4±3.4	−188.0±2.2	−188.2±1.6	−187.5±1.2	−177.9±2.6	−187.0±1.8	(−)180
γ	−65.0±15.5	40.2±1.8	57.5±0.1	57.5±0.1	57.6±0.1	41.4±1.6	41.5±1.4	47
δ	84.8±2.2	84.2±1.6	78.1±0.6	80.1±0.8	80.7±0.3	81.2±0.4	82.2±0.3	85
ϵ	−152.1±8.2	−144.3±3.5	−153.8±1.8	−161.9±0.1	−154.0±3.3	−149.0±2.2	-	−152
ζ	−83.0±1.1	−68.5±2.3	−63.6±0.1	−83.9±0.1	−63.7±0.1	−63.6±0.1	-	−74
χ	−147.2±4.2	−145.9±1.8	−167.8±0.8	−164.6±1.8	−161.4±1.3	−156.8±1.0	−158.0±0.2	−160
P	10.1±2.6 C3'-*endo*	0.8±4.2 C2'-*exo*	19.2±2.2 C3'-*endo*	27.7±2.0 C3'-*endo*	8.9±0.7 C3'-*endo*	15.4±1.4 C3'-*endo*	22.5±0.6 C3'-*endo*	18 C3'-*endo*

	C65	T64	G63	T62	G61	A60	C59	average B-DNA
α	−82.8±50.0	−41.9±92.7	−30.7±97.5	13.7±104.6	14.0±108.9	−47.3±57.3	-	−60
β	−143.2±4.8	−163.6±14.0	−167.3±23.5	−167.9±15.0	−183.6±24.7	−180.3±9.0	-	(−)180
γ	63.6±57.8	90.0±55.3	89.9±53.3	13.4±146.0	104.9±14.6	24.54±107.3	10.5±5	36
δ	90.6±0.9	91.2±2.5	101.9±4.5	101.6±2.3	102.2±16.3	117.2±4.2	93.6±2.0	160
ϵ	-	142.6±44.4	133.5±51.6	127.8±47.4	164.2±50.8	112.1±53.9	182.5±57.1	155
ζ	-	−21.0±73.4	−0.4±63.7	−7.9±66.7	−42.8±55.6	13.7±73.0	−35.8±60.6	−90
χ	−120.5±1.5	−127.4±1.6	−145.4±2.1	−150.8±5.2	−148.0±3.9	−150.4±2.6	−159.8±0.7	−120
P	28.0±1.5 C3'-*endo*	63.9±6.2 C4'-*exo*	86.2±13.0 O4'-*endo*	91.9±3.1 O4'-*endo*	80.9±37 C4'-*exo*	116.1±9.1 C1'-*exo*	355.3±2.8 C2'-*exo*	162 C2'-*endo*

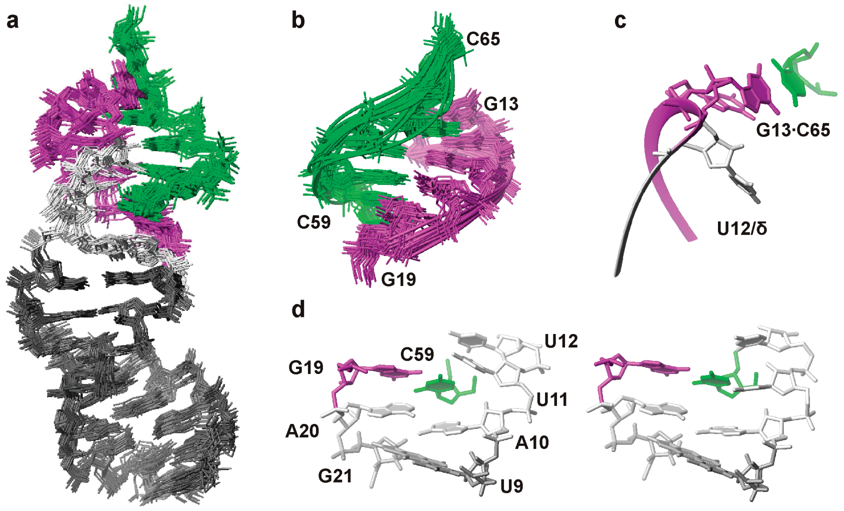

Figure 4.5: Solution structure of d3'EBS1·dIBS1. EBS1 nucleotides are colored purple, dIBS1 nucleotides are shown in green, nucleotides in single-stranded regions are shown in light gray, residues of the helical stem are shown in dark gray. (a) The 18 conformers of lowest energy superimposed by their heavy atoms. Hydrogen atoms are omitted for simplicity. (b) The EBS1·dIBS1 helix. While the EBS1 backbone traces are well converged, the dIBS1 backbone trajectory differs between the 18 conformers. (c) Close-up of the kink in the RNA backbone between U12 and G13. The sharp turn of the backbone moves G13 far from U12 and exposes it to the solvent on the 5'-side. (d) Two examples of the conformation of the single-stranded nucleotides that link EBS1·dIBS1 with the helical stem. A10 and A20 stabilize the junction of the stem helix and the EBS1·dIBS1 hybrid by stacking interactions. U11 and U12 show largest conformational variability among the d3'EBS1 nucleotides.

the EBS1·IBS1 homoduplex is a regular A-form helix [23], the heterogenous geometry of the EBS1·dIBS1 hybrid must be causing this drastically decreased affinity. To obtain more reliable data for the EBS1·dIBS1 interaction, we repeated the experiments at 15 °C, where the affinity is higher, and determined a K_D of 1.65 ± 0.2 µM (Table 4.3). We also tested the influence of low millimolar concentrations of Mg^{2+} on the stability of the interaction (Figure 4.6 and Table 4.3). Strikingly, in the presence of only 1 mM Mg^{2+}, which is in the range of the physiological intramitochondrial Mg^{2+} concentration [239, 240], k_off and, consequently K_D decrease by a factor of 6 and 4.6, respectively, and in the presence of 2 mM Mg^{2+} the K_D is about one order of magnitude lower than in the absence of Mg^{2+}. This demonstrates that Mg^{2+} is of vital importance to stabilize EBS1·dIBS1 by inhibiting dissociation of the two strands. Importantly, all experiments were carried out in a buffer with an equal ionic strength of 110 mM KCl sufficient to provide charge screening of the polyanionic sugar-phosphate backbone. Consequently, the stabilization induced by Mg^{2+} is of a specific nature and not simply a charge compensation effect.

Also, the affinity of the RNA·RNA contact is increasing upon addition of Mg^{2+} (Table 4.3). Wherease the RNA·RNA contact shows a very similar K_D in 1 and 5 mM Mg^{2+}, suggesting that the maximum affinity has been reached, the K_D of the RNA·DNA contact seems to

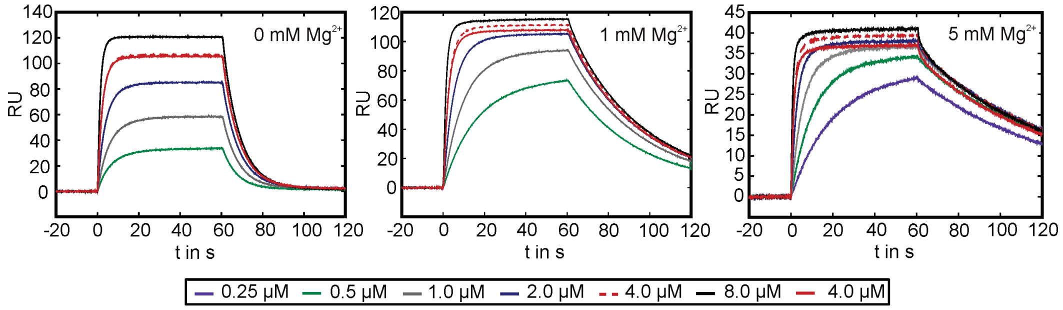

Figure 4.6: Sensorgrams of dIBS1 to d3'EBS1 binding in the presence of different concentrations of Mg^{2+}. The legend is sorted in the order of injection of the different dIBS1 concentrations. The injection starts at t = 0 s and ends at t = 60 s. All experiments were carried out at 15 °C. In the presence of 5 mM Mg^{2+}, an additional injection with 0.25 μM dIBS1 was added to sample the concentration range around the lowered K_D better. The presence of increasing amounts of Mg^{2+} markedly slows down the dissociation of dIBS1 (t > 60 s) from d3'EBS1. Note the decreasing total maximum RU value (RU_{max}) reached in 1 and 5 mM Mg^{2+} and the lower RU_{max} reached in the second injection of 4.0 μM dIBS1 relative to the first injection, which indicate Mg^{2+}-enhanced self-cleavage of d3'EBS1 from biotin.

stabilize only at 10-20 mM Mg^{2+}. Also, $[Co(NH_3)_6]^{3+}$ enhances the affinity of dIBS1 for d3'EBS1 (Appendix 7.2). $[Co(NH_3)_6]^{3+}$ is a kinetically stable complex, which mimics a hexahydrated Mg^{2+} ion. It thus probes for outer-sphere binding events of Mg^{2+}, that means a coordination mediated by the water ligands [183]. In 1 mM $[Co(NH_3)_6]^{3+}$, the K_D of dIBS1 binding to d3'EBS1 is 0.05 μM (k_{on}=0.14 $\mu M^{-1}s^{-1}$, k_{off}=0.008 s^{-1}, 15 °C) and thus is comparable to the values obtained in 20 mM Mg^{2+} (Table 4.3). $[Co(NH_3)_6]^{3+}$ binds to nucleic acids with higher affinity than Mg^{2+} [241,242], explaining the stronger stabilization effect. The ability of $[Co(NH_3)_6]^{3+}$ to stabilize EBS1·dIBS1 suggests that specific inner-sphere contacts between Mg^{2+} and EBS1·dIBS1 are not required for the stabilization.

For comparison, SPR data for the wild type sequences of d3'EBS1 and (d)IBS1 were collected. The wild type EBS1·(d)IBS1 helix has two A·U base pairs (instead of C·G) in positions 15·63 and 17·61 (Figure 4.1b, Section 4.2), which is reflected in the drastically lower stabilities of wild type d3'EBS1·(d)IBS1 (Table 4.3). Just like the mutant, the wild type contact is efficiently stabilized by Mg^{2+} addition. In fact, precise rate constants can only be measured in the presence of at least 5 mM Mg^{2+}.

4.3.4 Two metal ion binding sites are located in the EBS1·dIBS1 region

As Mg^{2+} is critical not only for EBS1·dIBS1 stability but for the folding of group II introns and retrohoming in general, we localized Mg^{2+} binding sites by a combination of Mg^{2+}, Mn^{2+} and $[Co(NH_3)_6]^{3+}$ titrations.

To determine Mg^{2+} binding sites, an NMR sample was titrated with millimolar concentrations of Mg^{2+} and $[Co(NH_3)_6]^{3+}$. A plot of the chemical shift differences $\Delta\delta$ of the protons of d3'EBS1·dIBS1 in the presence of 3 mM Mg^{2+} and 2 mM $[Co(NH_3)_6]^{3+}$ is depicted in Fig-

Table 4.3: Influence of Mg^{2+}-addition on the kinetics of (d)IBS1 binding to d3'EBS1 and (d)IBS1wt binding to d3'EBS1wt as determined by SPR experiments. Listed are the arithmetic means and one standard deviation of k_{on}, k_{off} and K_{D} from measurements on two different sensor chips.

analyte, T	c(Mg^{2+}) in mM	k_{on} in $\mu M^{-1}s^{-1}$	k_{off} in $\mu M^{-1}s^{-1}$	K_{D} in μM
dIBS1 DNA, 15 °C	0	0.11±0.04	0.18±0.08	1.65±0.20
	1^a	0.08	0.03	0.36
	2	0.15±0.07	0.02±0.01	0.20±0.03
	5	0.19±0.06	0.01±0.01	0.10±0.01
	10^a	0.20	0.01	0.07
	20	0.19±0.01	0.01±0.01	0.05±0.01
	0^b	0.12±0.01	0.21±0.04	1.60±0.14
dIBS1 DNA, 25 °C	0^c	0.05±0.02	1.45±0.35	29.0±5.65
	1^a	0.21	0.64	3.00
	5^a	0.24	0.18	0.72
IBS1 RNA, 25 °C	0	0.10±0.02	0.015±0.010	0.15±0.03
	1	0.17±0.08	0.006±0.001	0.04±0.02
	5	0.21±0.13	0.005±0.001	0.03±0.01
dIBS1wt DNA, 15 °C	0^{ad}	-	-	747
	5^{ac}	0.04	0.89	25.5
	20^a	0.05	0.42	8.17
IBS1wt RNA, 15 °C	0^c	0.05	1.15	21.3
	5^a	0.05	0.14	2.92
	20^a	0.08	0.06	0.71

[a] only one measurement was performed

[b] the 0 mM measurement was repeated to rule out on influence of Mg^{2+}-induced degradation on the kinetic parameters

[c] rate constants are at the instrument limit

[d] rate constants are outside the instrument limit, K_{D} was determined by fitting to the equilibrium RU_{max} values

ure 4.7. In the middle of the d3' stem the protons of the two base pairs G4·C26 and U5·A25 react to Mg^{2+} addition with intermediate chemical shift changes (Figure 4.7a). U5H6 and G4H8 resonances also shift strongly in the presence of the larger $[Co(NH_3)_6]^{3+}$ molecule indicating that the d3' stem contains a binding site that is accessible for both hydrated and bare Mg^{2+} ions. In the loop region (Figure 4.7b), U11H1', U12H1' and A20H8 and A20H2 display intermediate $\Delta\delta$ values while A10H2, G21H1' and C59H6 experience strong chemical shift changes > 0.05 ppm in the presence of both Mg^{2+} and $[Co(NH_3)_6]^{3+}$. C59H6 is most affected, moving by 0.074 ppm. These findings suggest that the U9·G21 wobble pair that closes the loop, the adjacent single stranded region, and C59 constitute a Mg^{2+} binding site. In a similar titration experiment of $[^1H,^{15}N]$-HSQC correlations (data not shown), the chemical shifts of A10N3 and A20N1 changed by 0.5 ppm upon addition of 3.5 mM Mg^{2+}, which corroborates this finding. G13 proton cross peaks were not observable during the

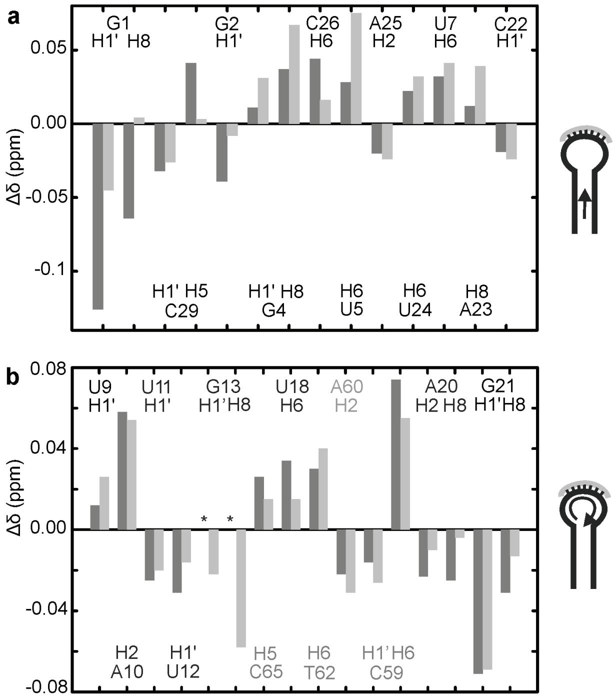

Figure 4.7: Chemical shift changes $\Delta\delta$ induced by Mg^{2+} and $[Co(NH_3)_6]^{3+}$ of (a) RNA proton resonances of the d3' stem and (b) RNA and DNA proton resonances of the loop region and EBS1·dIBS1. Displayed are the chemical shift differences between 3 mM and 0 mM Mg^{2+} (dark gray) and between 2 mM and 0 mM $[Co(NH_3)_6]^{3+}$ (light gray). Only resonances with a chemical shift difference of ≤ 0.02 ppm for either 2 mM Mg^{2+} or 3 mM $[Co(NH_3)_6]^{3+}$ were taken into account. For G13 there are no data in the presence of Mg^{2+} (*) because the peaks were not detectable in the spectra. Residues are ordered from left to right as illustrated on the right-hand side of the plot (see numbering in Figure 4.1b).

titration with Mg^{2+}, but addition of 2 mM $[Co(NH_3)_6]^{3+}$ has a large impact on G13H8. Also, the H1' of G13 and H5 of C65 experience intermediate $\Delta\delta$ in reaction to both $[Co(NH_3)_6]^{3+}$ and Mg^{2+}. This indicates a second binding site near the other end of the EBS1·dIBS1 helix. Within the EBS1·dIBS1 interaction, the A60·U18 base pair is most influenced by Mg^{2+}. H1' and H8 of G1 display very drastic shifts in the presence of Mg^{2+}, which result from Mg^{2+} binding to the di- or triphosphate moiety only present on the 5'-nucleotide [185, 218]. As this binding site, which also causes the $\Delta\delta$ of C29 and G2 protons, does not exist in the context of the whole intron, we will not discuss it any further.

A Mg^{2+}-induced chemical shift change of a proton can be the result of coordination of Mg^{2+} at the same residue or of subtle structural rearrangements caused by Mg^{2+} coordination in the vicinity. It can also be a mixture of both effects. However, the relative cross peak intensities in fingerprint regions such as the H1'-H6/8 and H2'/H2"-H6/8 cross peaks in the $[^1H,^1H]$-NOESY and the intense A10-U12 H1'-H2' C65 H3'-H4' cross peaks in the $[^1H,^1H]$-TOCSY remain unchanged in the presence of up to 4 mM Mg^{2+} and 2 mM $[Co(NH_3)_6]^{3+}$ (data not shown) [2]. This means that neither metal ion causes significant changes in the d3'EBS1·dIBS1 structure.

To locate Mg^{2+} binding sites more precisely, titration experiments were conducted with metal ions that affect NMR parameters other than the chemical shift. Mn^{2+} is a paramagnetic metal ion. Its binding to RNA at specific sites promotes relaxation of the protons in the vicinity, depending on the distance between the manganese and the proton nucleus [180]. At low ratios of Mn^{2+} to RNA (1:100), selective broadening of the resonances in Mn^{2+} binding sites can be monitored [243, 244] undisturbed by structural rearrangements.

---

[2] Other H1'-H2' or H3'-H4' TOCSY correlations could not be reliably analyzed due to line broadening.

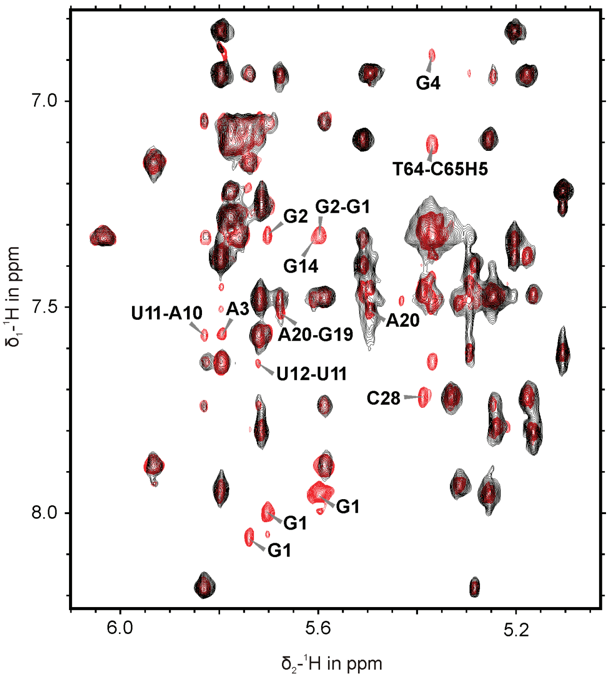

Figure 4.8: Mn^{2+} binding causes line-broadening of RNA and DNA protons. Superposition of the [^{1}H,^{1}H]-NOESY spectrum (25 °C in D_2O, 110 mM KCl, 10 µM EDTA, pD 6.8) recorded in the absence of Mn^{2+} (red) and in presence of 60 µM Mn^{2+} (black), respectively. Unless otherwise noted, all labeled resonances in F1 belong to H6 or H8 protons and resonances in F2 to H1' protons. Peaks that have broadened below the detection threshold due to the presence of Mn^{2+} appear in red. Some cross peaks like A20H1'-H8 and A20H8-G19H1' display severe broadening but are still detectable, indicating a weaker interaction of the proton and the Mn^{2+} ion.

We therefore recorded [^{1}H,^{1}H]-NOESY spectra in the presence of different micromolar Mn^{2+} concentrations (Figure 4.8). At 60 µM, very few peaks are already broadened below the detection limit, thereby indicating good binding sites for Mn^{2+}. Among the central residues in the d3' stem only G4 and A3 appear to be sensitive to the presence of Mn^{2+}. In the loop region, various protons are influenced by Mn^{2+}, but less strongly. The cross peaks between A10 and U11 and between U11 and U12 are not observable anymore in 60 µM Mn^{2+}. A20H8 and H1' also appear broader but are still observable. These findings support the idea of metal ion binding occurring at the single-stranded loop residues but imply low tendency of Mn^{2+} to bind here. C65H5 and T64H6 at the 3'-end of dIBS1 as well as G14H1' and H8 of EBS1 are broadened to baseline, indicating strong binding near the cleavage site. G13 resonances were not observed in either the absence or the presence of Mn^{2+} and could not be evaluated.

Finally, we performed structure calculations of $[Co(NH_3)_6]^{3+}$ bound to d3'EBS1·dIBS1. Apart from the chemical shift changes that $[Co(NH_3)_6]^{3+}$ binding induces (Figure 4.7), NOEs between DNA or RNA protons (Table 6.2 in the Experimental Section) and the 18 protons of the NH_3 ligands can be observed upon binding of the complex to the nucleic acid in [^{1}H,^{1}H]-NOESY spectra. This fact is exploited to localize metal ion binding sites on DNA or RNA molecules [182, 245]. These NOEs were used to calculate the solution structure of d3'EBS1·dIBS1 with three $[Co(NH_3)_6]^{3+}$ molecules bound. To obtain a more comprehensive picture of the effect of different metal ions on different parts of d3'EBS1·dIBS1, we mapped the results of Mg^{2+}, Mn^{2+} and $[Co(NH_3)_6]^{3+}$ titrations on this structure (Figure 4.9a). Evidently, the three calculated $[Co(NH_3)_6]^{3+}$ binding sites (large dark blue spheres) coincide well with the protons reacting to the addition of Mg^{2+} (gray spheres) and Mn^{2+} (yellow spheres) and with protons that are strongly affected by at least two different metal species (cyan spheres).

Ultimately, three metal ion binding sites of d3'EBS1·dIBS1 can be defined: the first one is located in the lower part of the RNA stem centered at the G4·C26 base pair, and the second and third site are found in the loop region. Of the latter two, one is located at the stem-loop junction, involving the unpaired bases on both sides of EBS1 and the G19·C59 base pair, and the other is formed between dIBS1 and EBS1, near the 5'-end of the EBS1. All of the resulting binding sites are situated in the major groove of either the stem or of EBS1·dIBS1. Figure 4.9a also demonstrates that Mg^{2+}-induced chemical shift changes alone (represented by gray spheres) often coincide well with the effect of other metal ions, indicating true binding regions. However, chemical shift changes can also be caused by structural effects on protons in the vicinity of a binding site [77] as is the case for U9H2' and U7H6 (see arrows in Figure 4.9a).

The proposed binding sites agree well with the electrostatic surface potential of d3'EBS1·dIBS1 (see arrows in Figure 4.9b and 4.9c). In the case of the loop binding site close to G13·C65, the electrostatic surface potential map reveals a small, negatively charged tunnel that is formed between dIBS1 and EBS1. Probably, the Mg^{2+}, attracted by the negative charge, binds further inside this tunnel and interacts with N7 of G13 or G14. This possibility is not reflected by the calculated position of the $[Co(NH_3)_6]^{3+}$ ion, which is probably due to the complex being too big to enter the tunnel. In contrast to Co^{3+} in $[Co(NH_3)_6]^{3+}$, both Mg^{2+} and Mn^{2+} can shed their water ligands partly or entirely and make inner-sphere contacts to nucleic acid ligands. Importantly, the addition of the much smaller Mn^{2+} ion has an effect on G14 protons, whereas $[Co(NH_3)_6]^{3+}$ addition does not, which supports the concept of Mg^{2+} and Mn^{2+} binding further inside the tunnel than $[Co(NH_3)_6]^{3+}$.

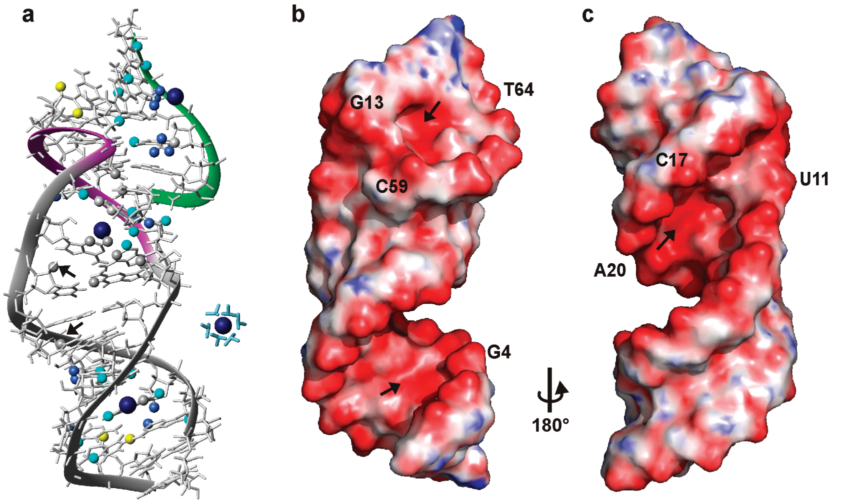

Figure 4.9: Proposed metal ion binding sites of d3'EBS1·dIBS1 and their relation to the electrostatic surface potential. (a) Metal ion binding regions defined by titration experiments. The effect of the three different metal ions Mg^{2+}, Mn^{2+} and $[Co(NH_3)_6]^{3+}$ are mapped onto the structure of d3'EBS1. Protons suffering only complete line broadening at 60 µM Mn^{2+} are shown as yellow spheres. Protons displaying only NOEs to $[Co(NH_3)_6]^{3+}$ protons are shown as blue spheres. Protons experiencing only chemical shift differences $\leq$ 0.02 ppm in presence of 3 mM Mg^{2+} are shown as gray spheres. Protons featuring at least two of these three effects are shown as cyan spheres. The positions of bound $[Co(NH_3)_6]^{3+}$ ions were defined by rMD calculations. Co^{3+} central ions are shown as large, dark blue spheres, the ammine ligands are omitted for the sake of clarity. A $[Co(NH_3)_6]^{3+}$ molecule with ligands is shown on the right for size comparison. (b) and (c) Electrostatic surface representation of d3'EBS1·dIBS1 displaying three patches of negative potential. The potential is represented by a color gradient from red (−667 mV) to blue (128 mV).

4.4 Discussion

In this study, we present the first solution structure of an EBS1·dIBS1 hybrid representing the recognition and cleavage site of a group IIB intron and a DNA target. In the absence of their binding partner, dIBS1 is entirely unstructured and d3'EBS1 forms a stable hairpin with an unstructured loop region [23]. Upon dIBS1 binding to EBS1, the two form a short hybrid helix whose position relative to the stem is determined by the stacking interactions and putative hydrogen bonds between the single-stranded nucleotides surrounding EBS1. Due to EBS1·dIBS1 helix formation, the loop backbone is no longer flexible and is forced to assume a sharp turn between the first nucleotide of EBS1 and U12/δ base. These structural features are highly similar to those of the analogous RNA·RNA interaction of d3'EBS1·IBS1 that was previously solved in our group (Figure 4.10, compare Figure 4.10a and Figure 4.5). Based on this structure, we argued that the position of EBS1 in the loop and the length of the loop forcibly leads to formation of this turn upon IBS1 binding and hence to adjusting the scissile bond at the 3'-OH of C65 in a defined position easily accessible for the other active site components. In this paper, we demonstrate that also the dIBS1 target strand induces the same characteristic kinked structure of the recognition complex, although it has a much weaker affinity and different conformation when bound to EBS1 as opposed to the RNA target. Also, in the crystal structure of a substrate-bound group IIC intron [231], a very similar turn is observed between δ and the first EBS1 nucleotide, and δ' and IBS1 bind from different sides, thus supporting a general relevance of the kink for the active site architecture. The helical geometries of EBS1·dIBS1 and EBS1·IBS1 are very different on the side of the target strand. This difference strongly suggests that the specific geometry of EBS1·(d)IBS1 is not relevant for cleavage site recognition, with the exception of C65. At C65, the cleavage site, the structure of dIBS1 and IBS1 is more similar. C65 in dIBS1 has the (for DNA) unusual C3'-*endo* sugar pucker, which it naturally has in IBS1 RNA. Probably, this conformation is meaningful for the alignment of the scissile bond in the active center and the coordination of the catalytic Mg^{2+} ions, and thus it must be the same in both DNA and RNA targets. The importance of the conformation of C65 is underlined by the crystal structure of the group IIC intron of *O. iheyensis*, in which two metal ions are coordinated in the active site between the backbone of the 3'-terminus of IBS1 and the catalytically relevant nucleotides of DV [231], in a position and mutual distance that would allow catalysis by a two-metal ion mechanism [222].

The RNA·RNA and the RNA·DNA contacts differ in the relative orientation of the EBS1·(d)IBS1 helices to the d3' stem (Figure 4.10b and c); EBS1·IBS1 is more tilted than EBS1·dIBS1, resulting in a different position of the cleavage site with respect to the stem (Figure 4.10c). One possible interpretation is that the hybrid helix, being more flexible than the homoduplex, can arrange in a way that maximizes stacking onto the stem helix, whereas the RNA·RNA interaction is too rigid for this. Within the full-length intron, however, this difference might be of little consequence, because a multitude of interactions such as the δ-δ' base pair (Figure 4.1c) and tertiary contacts between DV and EBS1·IBS1 [246] as well as contacts between the target strand and the auxiliary protein components of the IEP influence the exact cleavage site position.

The difference in geometry between the RNA·RNA and the RNA·DNA interaction causes the latter to be markedly less stable. This is well in line with previous studies attesting lower melting temperatures and lower thermodynamic stability to hybrid helices in comparison to RNA·RNA homoduplexes of corresponding sequence [247–249]. We could show by SPR measurements that Mg^{2+} concentrations similar to the physiological concentration stabilize both the RNA·DNA and the RNA·RNA interaction strongly without altering the overall helical geometry. Control experiments did not reveal any changes in the fold or the flexibility of the unbound d3'EBS1 loop upon Mg^{2+} addition [23]. This is in line with the observation that Mg^{2+} has little influence on the association of EBS1 and dIBS1. In contrast to this, Mg^{2+} strongly decreases the dissociation rate constant. Probably, Mg^{2+} helps to prevent dissociation of the exon-intron recognition complex until all active site components have been assembled or even throughout the cleavage reaction. In the following, the metal-ion binding sites relevant for this stabilization will be evaluated. At the K^+ and Mg^{2+} concentrations used, it is probable that also diffuse Mg^{2+} ions play a role in the stabilization of EBS1·(d)IBS1 [250]; a detailed quantification of their influence, however, is beyond the scope of this work. We thus focus the discussion on the site-bound Mg^{2+} ions. The binding site found in the d3' RNA stem of d3'EBS1 shows a preference for

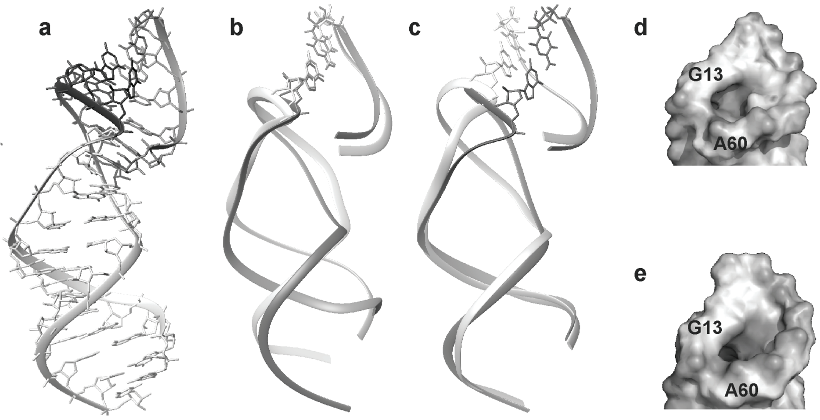

Figure 4.10: Comparison of the solution structures of the d3'EBS1·dIBS1 RNA·DNA contact and the d3'EBS1·IBS1 RNA·RNA contact. (a) Structure of d3'EBS1·IBS1. (b,c) Overlay of the backbone traces of d3'EBS1·dIBS1 (light gray) and d3'EBS1·IBS1 (dark gray) (b) aligned by the backbone atoms of nucleotides 13-17 (in EBS1) and 61-65 (in dIBS1) close to the cleavage site (RMSD = 1.17 Å), and (c) aligned by the heavy atoms of the stem nucleotides (1-9 and 21-29, RMSD: 1.45 Å) showing only the G13·C65 base pair directly next to the cleavage site. (d) Electrostatic surface potential representation of d3'EBS1·dIBS1 and (e) of d3'EBS1·IBS1 depicting the strongly negative potential (indicated by the dark shade) in the tunnel formed by the major groove of the EBS1·(d)IBS1 helix. Images of d3'EBS1·IBS1 were prepared from pdb entry 2M23 [23].

$[Co(NH_3)_6]^{3+}$ or hydrated Mg^{2+} because for almost all protons, 2 mM $[Co(NH_3)_6]^{3+}$ cause stronger chemical shift changes than 3 mM Mg^{2+} (Figure 4.7a), and a wealth of NOE correlations to $[Co(NH_3)_6]^{3+}$ are observed. Such outer-sphere binding sites in the major groove are regularly found in RNA [183]. Possibly, this binding site contributes to stability (*e.g.* by making the d3' stem more rigid). However, the two metal ion binding sites in the loop region (Figure 9A) directly involve EBS1 and dIBS1 nucleotides and thus seem more relevant for the affinity of d3'EBS1·dIBS1 in the presence of Mg^{2+}. These are located in the major groove at the two termini of EBS1·dIBS1. Neither binding site shows a clear preference for inner- or outer-sphere binding. In general, the NMR and SPR data do not provide an exact characterization of the mode of interaction [54, 55] of the Mg^{2+} ion with each binding site, because all three metal ions tested are able to interact with each binding site and because both Mg^{2+} and $[Co(NH_3)_6]^{3+}$ efficiently enhance affinity of dIBS1 for d3'EBS1.

Metal ion binding at the 5'-end of dIBS1 may reduce the flexibility of the unpaired nucleotides and contribute to stabilize this end of the EBS1·dIBS1 helix, by accepting ligand atoms from C59, G19 and the unpaired nucleotides surrounding them. In the second loop binding site, located between EBS1 and dIBS1 close to the G13·C65 and G14·T64 base pairs, Mn^{2+} and Mg^{2+} seem to be able to bind deeper inside the tunnel-shaped major groove than $[Co(NH_3)_6]^{3+}$. This indicates that a Mg^{2+} ion might be able to move slightly within this binding region by exchanging some of its hydration shell with nucleic acid ligands. Such partial inner-sphere coordination is well in line with crystal structures of RNAs in general, which show that the vast majority of Mg^{2+} ions are partially dehydrated [75, 251]. In general, the combination of the kink in the sugar-phosphate backbone at G13 and the short and tunnel-shaped major groove of EBS1·dIBS1 seems ideal to attract metal ions because it provides a suitable shape and accumulates negative charge in a small region. The G9·U21 wobble pair closing the loop, which is known for its affinity towards metal ions, completes this binding platform.

Mg^{2+} titrations of d3'EBS1·IBS1 indicate that Mg^{2+} binds to the same regions in both constructs [23]. This means that the overall structure described above, which is common to the RNA·RNA and the RNA·DNA contact (Figure 4.10b-e) is much more relevant to attract metal ions than the specific geometry of the EBS1·(d)IBS1 helix including the exact width of the major groove, which is different (Figure 4.10d and e). Moreover, this structure is supposed to form independently of the exact sequences of dIBS1 and EBS1, provided the length and position of EBS1 in the d3' loop are suitable (see above and reference [23]). The hypothesis of equivalent Mg^{2+} binding to different EBS1·(d)IBS1 sequences is tentatively supported by the observation that also the wild type sequences of d3'EBS1·IBS1 and d3'EBS1·dIBS1 show much higher affinities in the presence of low milimolar Mg^{2+} concentrations. However, localization of these binding sites and structure determination is impeded by the low affinity of the wild type recognition complexes.

It thus is reasonable to assume that similar structural features as described above are used by different group II introns to attract stabilizing metal ions to the EBS1·IBS1 complex. In the case of the *O. iheyensis* group IIC intron, a binding site for divalent metal ions is found in the d3' stem major groove near the single-stranded nucleotides framing EBS1 [231]. Furthermore, G·U wobble base pairs are found at different positions within EBS1·IBS1 (as in *Rm*Int1 [252], *Sc*B1 and *So*PETD [198] and *Ec*I5 introns [253] or at the final base pair of the d3' stem (as in *Pl.*LSU/2 [254], *Ll.*LtrB [255] introns) in other group II introns supporting the idea that metal ion binding in EBS1·IBS1 is a common feature.

It has been shown both in bacterial and eukaryotic cells that the efficiency of retrohoming is strongly coupled to the Mg^{2+} concentration in the cell [226, 227]. In fact, the lower Mg^{2+} concentration of the eukaryotic cell limits the retrohoming efficiency of group II introns that are of bacterial origin. Probably, group II introns residing in eukaryotic genomes have evolved to make optimal use of the available Mg^{2+} (*e.g.* by promoting structures such as the one of the cleavage site recognition complex described herein).

4.5 Accession codes

Structure coordinates and NMR restraint files have been deposited to the PDB with the accession code 2M1V. ^{1}H, ^{13}C and ^{15}N chemical shifts have been deposited to the BMRB with the accession code 18881.

5 The CPEB3 Ribozyme

5.1 Introduction

5.1.1 Discovery

Until recently, small self-cleaving ribozymes were thought to exist only in satellite RNA sequences. These sub-viral agents are capable of co-infecting their host depending on infection with a helper virus. The self-cleavage activity of these ribozymes is used to separate multiple copies of the genome generated during rolling circle replication (Figure 3.5a).

Although the rapid progress in bioinformatic (and *in vitro* selection) techniques helped to locate small ribozymes in the genomes of several organisms, the discovery of such self-cleaving sequences in mammalian genomes was unexpected. To date, very few mammalian sequences have been reported to possess self-cleavage activity. These include: the CoTC motif in the 3'-UTR of the β-globin gene [115]; a discontinuous hammerhead ribozyme in the 3'-UTR of C-type lectin type 2 genes [256]; a hammerhead ribozyme in an intron of a tumor suppressor gene [257]; and four human sequences in the olfactory receptor *OR4K15*, in the insulin-like growth factor 1 receptor *IGF1R*, in a LINE 1 retrotransposon and in the *cpeb3* gene [92]. However, only the CPEB3 sequence has been investigated in more detail.

The discovery of the CPEB3 ribozyme [92] was the result of an elegant *in vitro* selection approach [120] using a human genomic library of circularized fragments and selecting self-cleaving sequences without any prior knowledge about the cleavage site sequence. The CPEB3 ribozyme resides in the second intron of the *cpeb3* gene, which encodes a cytoplasmic polyadenylation element binding protein. Self-cleavage of the bond between the -1 nucleotide and the first nucleotide (G1) of the ribozyme thus disrupts the pre-mRNA of the CPEB3 protein.

CPEB proteins regulate mRNA translation in the cytoplasm by promoting 3'-polyadenylation of the mRNA but can also act as translational repressors [258]. They were initially shown to mediate *Xenopus laevis* oocyte maturation [259] and are now known to regulate embryogenesis in several organisms [260–262]. CPEB homologues in rodents, *Aplysia* and *Drosophila* are implicated in synaptic plasticity [263] and have been suggested to mediate long-term memory formation by forming prion-like structures [264, 265].

CPEB3 ribozyme cleavage yields the typical products of the self-cleavage reactions of small ribozymes (Figure 3.7a), which are a 2'-3' cyclic phosphate on one strand and a 5'-OH on the other strand [92]. Expressed sequence tags (EST) of CPEB3 have been detected in tissues of mouse, human and opossum. These ESTs contain the ribozyme sequence and terminate exactly at its cleavage site, and thereby provide evidence for the CPEB3 ribozyme being expressed and active *in vivo* [92, 266].

The sequence of the CPEB3 ribozyme (as the *cpeb3* gene in general) has a high degree of identity in mammals but no orthologues in other eukaryotes have been found. It is thus believed that the sequence is of mammalian origin and of functional relevance. This function, however, remains largely obscure. Vogler et al. have established a connection between a single nucleotide polymorphism (SNP) in position 36 of the ribozyme and episodic memory in humans [267]. The twofold faster cleavage of the rare variant with a U36C SNP was shown to be correlated with decreased memory performance. A possible role for the ribozyme is to regulate the levels of CPEB3 protein in the cell. However, judging only by the *in vitro* cleavage rate of the ribozyme this seems unlikely as it is too slow in comparison to the speed of transcription and splicing [266]. Later results suggested that the ribozyme is able to cleave very fast but retarded by alternative pairing of the P1/P1.1 helices (Figure 5.1) with the sequence upstream of the cleavage site [268]. In the light of these findings, it seems very probable that there is additional regulation of the ribozyme activity in the cell; this might also explain the different tissue-specific ratios of cleaved-to-uncleaved sequences [92].

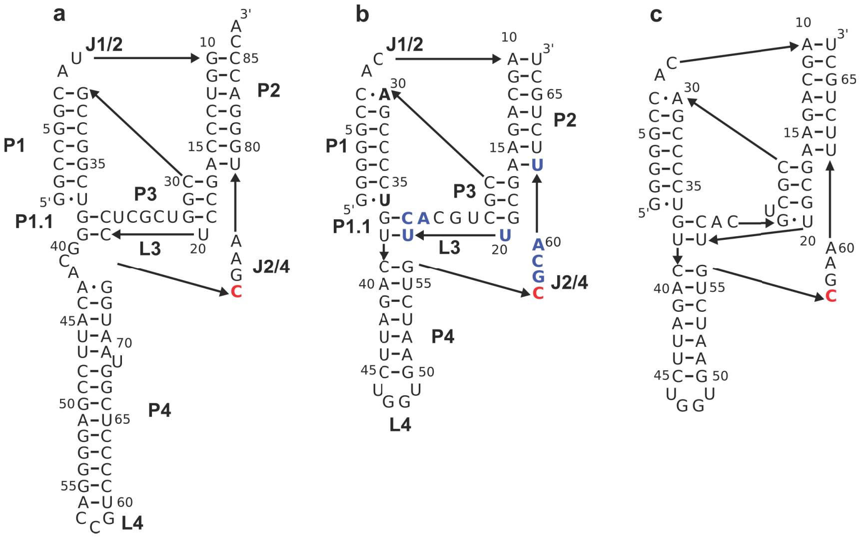

Figure 5.1: Secondary structures of (a) the genomic HDV ribozyme (b) the human CPEB3 ribozyme, (c) the human CPEB3 ribozyme with an extra reverse G25·U20 wobble base pair and. The active site cytosine (red) and the CPEB3 nucleotides, which have the strongest effect on catalytic activity when substituted by phosphorothioate [92] (blue, see text) are printed in boldface.

5.1.2 Structure and Function of CPEB3

When Salehi-Ashtiani et al. first characterized the self-cleavage of the CPEB3 ribozyme [92], they found the optimum catalytic conditions remarkably similar to those of the HDV ribozyme. Both ribozymes rely on divalent metal ions to achieve their maximal catalytic rate and are inhibited by $[Co(NH_3)_6]^{3+}$. This sets the two apart from all other small ribozymes, which sustain activity in high concentrations of only monovalent metal ions [90]. Furthermore, the cleavage rate is near-constant between a pH of 5.5 and 8.5 but is decreased by 20 % in D_2O [92], which argues for a catalytic mechanism that involves proton transfer in the rate-limiting step. Likewise, pH dependency and kinetic isotope effect have been precedented in the HDV ribozyme, whose catalytic mechanism has been thoroughly investigated [269].

In the HDV ribozyme, which cleaves off the sequence upstream of its first nucleotide (G1), the pK_a of C75 (red in Figure 5.1a) is perturbed by more than 2 units towards a neutral pH [270], suggesting that C75 is able to transfer protons in a physiological environment similar to histidine in proteins. C75 is thus referred to as the catalytically active nucleotide. Furthermore, C75 is in close contact with the 5'-O(H) of G1 in the crystal structure [38, 271], and in a suitable position to act as a general acid in the ribozyme cleavage reaction [272–274]. As such, it stabilizes the negative charge formed on the leaving group, that is the 5'-O(H) of G1. Nevertheless, the strong dependence of the catalytic rate of the HDV ribozyme on Mg^{2+} concentration implies that divalent cations play a role in the catalytic mechanism [270, 275]. More specifically, efficient catalysis requires inner-sphere contacts between Mg^{2+} ions and the active site as shown by competition experiments between $[Co(NH_3)_6]^{3+}$ and Mg^{2+} monitored by Raman spectroscopy [276]. A Mg^{2+} ion in the active site might aid catalysis by positioning the 2'-OH of the nucleotide preceding G1 for in-line attack on the phosphodiester bond [271]. In summary, the HDV ribozyme combines nucleobase- and metal ion-assisted catalysis and it is assumed that the CPEB3 ribozyme does the same [92].

The mechanistic similarities between both ribozymes are supported by the fact that the CPEB3 sequence can be threaded in the characteristic secondary structure of the HDV ribozyme [92] despite the lack of sequence conservation between HDV and CPEB3 (Figure 5.1a and b). This putative secondary structure (Figure 5.1b) is supported by enzymatic structure mapping and native gel analysis [268]. It comprises two helices (P1 and P2), the single base pair P1.1, the internal P3 hairpin with the L3 loop, the P4 hairpin with the L4 loop and the single-stranded linker regions J1/2 and J4/2 [38, 107, 277]. In the precleavage HDV ribozyme, a reverse G·U wobble pair is observed between G25 and U20 [38, 271], which is assumed to be stable throughout the catalytic cycle [278,279], and which was later suggested to be generally relevant for the cleavage reaction of the HDV-like ribozymes [280]. An analogous interaction could exist in the CPEB3 structure (Figure 5.1c).

This kind of secondary structure is referred to as a 'nested double pseudoknot'. The term can be understood in the following way: there is an outer/large pseudoknot formed by P1 and P2 and an inner/small pseudoknot formed by L3 and P1.1, which is embedded in the outer one, because P3 and L3 belong to the P1 loop.

Structural similarity of the CPEB3 and HDV ribozyme is supported by mutational studies of key positions in the CPEB3 ribozyme core. C57 of CPEB3 in the linker between P4 and P2 is in a position analogous to the one of C75 in the HDV ribozyme and was shown to be critical for ribozyme activity [92]. Moreover, the positions of phosphorothioate substitutions leading to decreased self-cleavage activity (Section 3.7.4, marked blue in Figure 5.1b) are the same in the HDV [281] and the CPEB3 ribozyme [92]. These findings suggest that a similar network of interactions define the active sites in both ribozymes.

In summary, there is strong evidence for the HDV and CPEB3 ribozymes having highly similar secondary structures (Figure 5.1a and b) and catalytic mechanisms, which suggests a relatedness of the two ribozymes.

5.1.3 Evolutionary implications of HDV and CPEB3 resemblance

Before the discovery of the CPEB3 ribozyme, the two copies of the HDV ribozyme were the only members of their class. The fact that hepatitis delta virus is a pathogen exclusively infecting humans and that no similar satellites of other animals are known, prompts the hypothesis that the ribozyme has been transmitted from virus to human or *vice versa*. The fact that no HDV-like ribozyme could be detected in non-mammalian animals speaks for a relatively late emergence of the motif and thus for the transfer from human to virus [282]. In a similar manner, the ribozyme may have been passed down to the human gut bacterium *Faecalibacterium prausnitzii*, which is the only bacterium, in which an HDV-like ribozyme has been found to date [282]. Due to its complexity [283, 284], it seems unlikely that the structural motif of the HDV has arisen independently in diverse organisms. Meanwhile, sophisticated search algorithms have identified a variety of putative ribozymes belonging to the HDV-family in different genomes. These sequences are very diverse and adopt secondary structures that vary in the length and structure of L1/2 and P4 but retain the core fold of the HDV ribozyme [108, 282].

5.1.4 Aim

The combined nucleobase- and metal-ion assisted catalytic mechanism of the HDV and CPEB3 ribozymes as well as the complexity of their nested double-pseudoknot fold make them unique among the small self-cleaving ribozymes and a promising model to study the relationship between the structure and metal ion interactions. In this work, we aimed to prove the formation of the proposed secondary structure of the CPEB3 ribozyme in solution and thus its similarity with the HDV structure. A full NMR structure determination of the CPEB3 ribozyme was impeded by pronounced spectral overlap (Section 5.4), but by obtaining the first partial assignment of the proton and nitrogen resonances, we demonstrate the formation of the P4 domain and the outer/large pseudoknot by NMR. We also determined the solution structure of P4. A detailed analysis of the ribozyme's metal ion binding properties, using NMR, Tb^{3+}-induced cleavage experiments and two different approaches for determining stoichiometry, was performed. By discriminating distinct binding sites for Mg^{2+} and $[Co(NH_3)_6]^{3+}$ in the CPEB3 ribozyme and by combining our findings with the knowledge about the structure and metal ion binding sites of the HDV ribozyme, we discuss in how far Mg^{2+} is required to form the nested double-pseudoknot topology and key interactions within the active site of the ribozyme.

5.2 The choice of the NMR construct

Proton resonance assignment of an RNA as large as 67 nt is a challenging task as spectral overlap and line widths increase with the number of nucleotides (Section 3.7.1). Moreover, the particular sequence and fold and the intramolecular dynamics of an RNA also affect the spectral dispersion and resolution. For example, the chemical shift dispersion of very repetitive sequences is often low, as many protons have very similar chemical environments. Dynamics in an RNA molecule can result in multiple resonances belonging to the same proton in different molecular conformations or in broad lines depending on the timescale of exchange.

In search of a suitable NMR construct of CPEB3, we first compared the wild type chimp and human CPEB3 sequences. These differ in only one nucleotide (compare Figures 5.1b and 5.3), which determines whether the P1 helix ends with a mismatch or a Watson-Crick base pair. Both constructs yielded similar substance amounts in *in vitro* transcription reactions and displayed similar and very low overall dispersion of peaks in [^{1}H,^{1}H]-NOESY spectra of the nonexchangeable protons (see spectrum in Appendix 7.3) By generating a mutant with an additional canonical base pair in P1.1 and a shortened P4 domain (Appendix 7.5b), we intended to create a more compact and more rigid version of the CPEB3 ribozyme. Another mutant with a GC-to-AU mutation in the P1 domain (Appendix 7.5c) was produced to avoid possible destabilization of the ribozyme by alternative base pairing in P1. Such might occur due to the long stretch of guanines and has been proposed to take place in the precleavage ribozyme [268]. However, the overlap problem persisted also in the [^{1}H,^{1}H]-NOESY spectra of these two mutants.

To investigate structural heterogeneity in the ribozyme as a possible source of badly resolved NMR spectra, the wild type human ribozyme was analyzed using native PAGE. The gels (Appendix 7.4) do not reveal any appreciable amount of extra conformations or multimers, neither in the absence or presence of Mg^{2+}.

Ultimately, the chimp sequence was used for all NMR studies requiring resonance assignments as the construct was expected to be slightly more stable than the human sequence due to the canonical base pairing throughout the P1 helix. For DOSY NMR experiments and for Tb^{3+}-cleavage studies, as well the human sequence of the ribozyme was used.

5.3 Self-cleavage activity

To assess whether the sequences used for NMR and Tb^{3+}-induced cleavage studies were catalytically competent or not, cotranscriptional cleavage studies were conducted. A DNA template strand was used for *in vitro* transcriptions that encodes the ribozyme sequence plus 18 nt on the 5'-end (Appendix 7.5d). After being transcribed, the ribozyme directly cleaves off the 18mer and the fragments can be separated by denaturing PAGE and detected by UV-light absorption.

The gels (Figure 5.2) clearly show an intense band (67mer) at the level of the postcleavage ribozyme control (C) and a band of a much shorter oligonucleotide, probably the cleaved 18mer upstream sequence near the bromophenol blue (BB) dye. Both bands become increasingly intense at longer incubation times, as expected. The faint band above the short cleavage product likely corresponds to the 24mer TS of the DNA template. The bands above the postcleavage ribozyme are more difficult to attribute. The longest band, in principle, must be the 107mer OT of the DNA template. However there are two bands very close together and they seem to be increasing in intensity over time, which is not the case for the template. The band between the two highest bands and the main product is probably the 85mer uncleaved sequence. The fact that this band is in all cases less intense than the postcleavage ribozyme band proves that cleavage proceeds faster than, or at least at a similar speed as the transcription and that the majority of molecules is indeed self-cleaving under the transcription conditions. Consequently, the sequence used for all further experiments very likely corresponds to the 67mer postcleavage ribozyme, which originates from a catalytically active sequence and should be adopting a functionally meaningful fold.

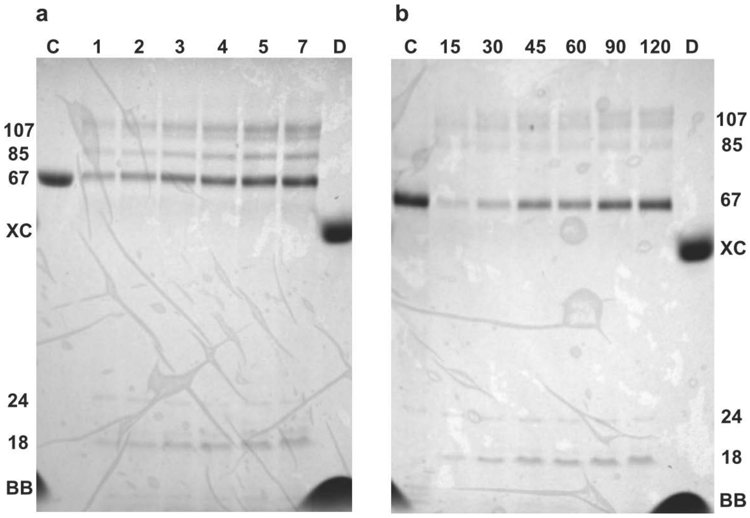

Figure 5.2: Self-cleavage assay of an elongated CPEB3 ribozyme. (a) human sequence, (b) chimp sequence. Standard *in vitro* transcription/cleavage reactions were left to proceed for 1-7 h in case of the human sequence and for 15-120 min in case of the chimp sequence. The incubation time is indicated on the top of the lanes. Lane "C" is the control sequence transcribed from a template that did not contain any nucleotides upstream of the ribozyme sequence. Lane "D" is the loading buffer. Left of the gel, the bands are labeled with the putative length (in nt) of the contained oligonucleotide (see text) and with "XC" and "BB" for the two dyes.

5.4 Resonance assignment

To obtain [^{1}H,^{1}H]-NOESY spectra amenable to resonance assignment (Section 3.7.1) in D_2O, the temperature, KCl concentration and pD value were optimized with regard to peak dispersion and resolution. Sample conditions of 50-100 mM KCl, a pD of 6.8 or 7.2 and a temperature of 25 °C proved to be appropriate. It was, however, obvious that optimization of these parameters would not result in sufficient spectral dispersion for complete resonance assignment (see the example spectrum in Appendix 7.3).

Less conventional approaches for relieving the spectral overlap via addition of cosolutes, such as 40 % PEG-400 or low millimolar amounts of the lanthanide ion Eu^{3+}, were also tested. PEG is used to simulate molecular crowding and has been shown to favor more

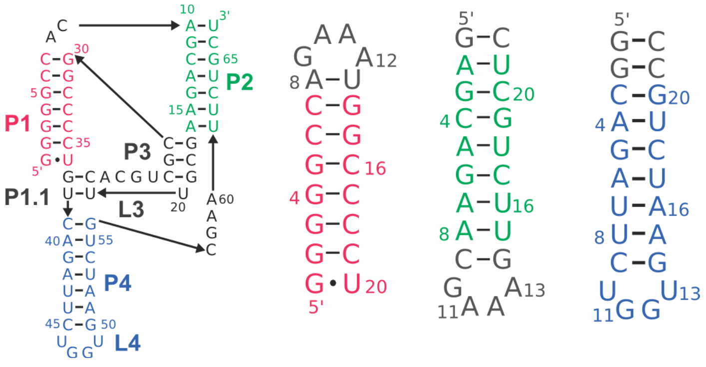

Figure 5.3: Auxiliary constructs used for resonance assignment of the protons in domain P1, P2 and P4 in spectra of the full-length chimp CPEB3 ribozyme.

compact folds and enhance the activity of several ribozymes [285–287]. We therefore hoped that it would reduce dynamics of the ribozyme as a potential source of badly resolved spectra. Eu^{3+}, as lanthanide ions in general, is known to course chemical shift changes of the proton resonances in its vicinity. This effect can be used to spread proton resonances over a wider range and to map metal ion binding sites [288]. Neither approach led to an improvement of the spectra; on the contrary, dramatically broadened lines were obtained in the presence of both agents. A significant improvement of the spectral resolution (compare spectra in Figure 5.5b and Appendix 7.3) was achieved by using partially deuterated CPEB3 RNA (Section 3.7.2).

Three auxiliary constructs (Figure 5.3) were used to assist and validate resonance assignment of the full-length construct. These represent the two helices P1 and P2 and the P4 hairpin. The P1 and P2 constructs are capped with a GAAA-tetraloop, which is very stable and has a well characterized chemical shift signature [289–291]. An extra base pair was added to decrease the influence of the tetraloop on the chemical shifts of the protons in the stem. In the P2 and P4 constructs, one or two G-C base pairs, respectively, were added to the start of the stem to increase the yields of *in vitro* transcription reactions [232].

5.4.1 Spectral features of the P1 and P2 domains

Proton resonance assignments of the P1 and P2 model constructs were relatively straightforward to obtain. Both P1 and P2 NMR spectra contain the typical spectral fingerprint of the GAAA-tetraloop [289–291], thereby proving hairpin formation. This fingerprint (see nucleotides 9-13 in Figure 5.4a and 10-14 in Figure 5.4b) comprises (i) the order in chemical shifts of the loop H8 protons, (ii) the drastic upfield shift of the H1' of the nucleotide 3' of the last adenine (see legend to Figure 5.4), (iii) the unusual downfield shift of H3' of the third adenine (labeled in Figure 5.4) and (iv) the intense H1'-H2' TOCSY cross peaks resulting from C2'-*endo* conformation of the two central adenines (data not shown).

G3 to G5 of P1 have very similar H1' and H8 resonances owing to the repetitive sequence. This creates a rather characteristic peak set in the [^{1}H,^{1}H]-NOESY spectrum (Figure 5.4a), with the H1' of each guanine being a bit more upfield shifted from G1 to G5. C16-C19 H1' and H6 on the opposite strand also cluster in a rather crowded spectral region but show no distinct evolution of the chemical shifts.

In the [^{1}H,^{1}H]-NOESY spectrum of the exchangeable protons of P1 (Appendix 7.8a), the discrimination of G3, G4 and G5 H1 was not possible based only on their mutual cross peaks. They were eventually assigned by their correlations to the H41 and H42 resonances of the base paired cytosines and the H5-H41/42 correlations within the cytosines.

For the P2 domain, resonance assignment was slightly challenging due to the presence of extra peaks (asterisks in Figure 5.4b and Appendix 7.8b) possibly stemming from a small duplex population in coexistence with the hairpin. Apart from this, the spectra do not contain uncommon features with the exception of G1H8 and A2H8 resonances being extremely similar. In the NOESY spectrum of the exchangeable protons (Appendix 7.8b), all expected correlations are present and well-dispersed.

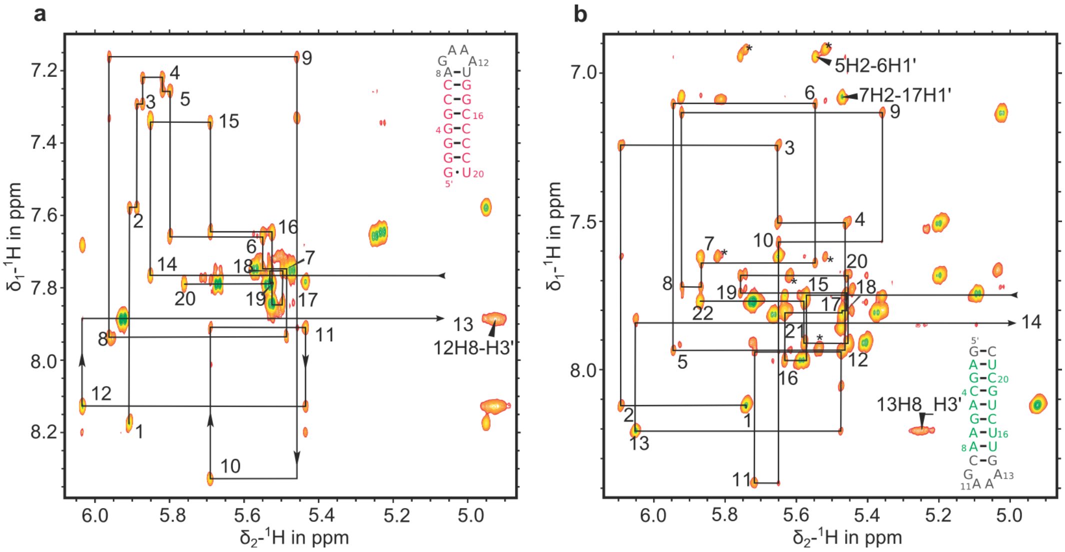

Figure 5.4: Sequential-walk region of [^{1}H,^{1}H]-NOESY spectra of the nonexchangeable protons of the model constructs (a) P1 and (b) P2. The sequential walk through the H1'-H8/6 protons is traced by black lines. Intranucleotide cross peaks are labeled with the nucleotide number. The H1' resonances of the nucleotide 3' of the tetraloop being U13 in P1 and G14 in P2 are far upfield shifted to 3.674 and 3.871 ppm, respectively, and thus not shown. The spectra were recorded at 25 °C in D_2O (100 mM KCl (P1) or 20 mM KCl (P2), 10 µM EDTA, pD 6.8).

5.4.2 Spectral features of P4

The assignment of the nonexchangeable P4 protons was unambiguous and straightforward to obtain from [^{1}H,^{1}H]-NOESY spectra (see Figure 5.5). The most interesting spectral features are contributed by the protons belonging to the UGGU tetraloop. The two G11H1'-H8 and and G12H1'-H8 cross peaks are very intense (bold labels in Figure 3.8a), indicating a *syn* conformation of these nucleotides.

G12H2' and G12H3' resonances are shifted downfield (see Figure 5.5a) while G11H4' is found unusually high upfield at 3.774 ppm (data not shown). Altogether, a wealth of NOE

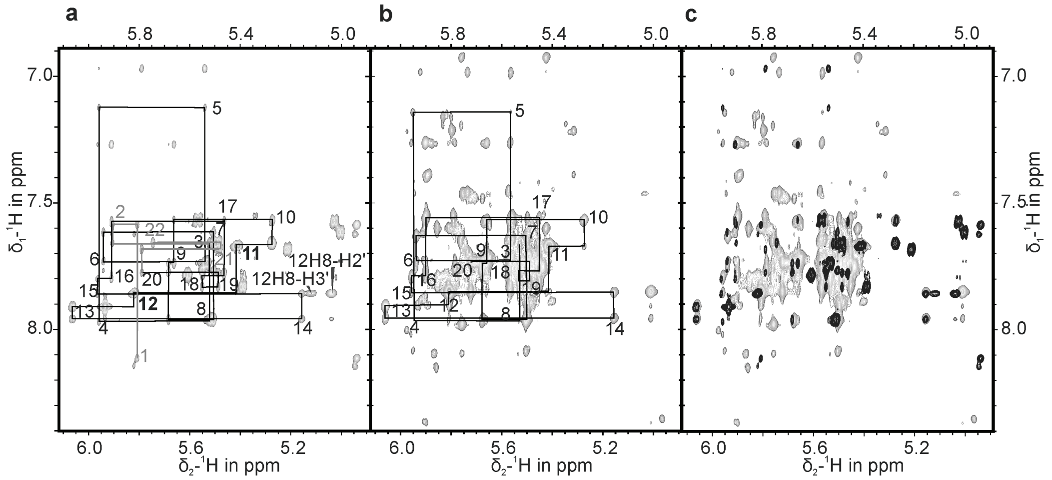

Figure 5.5: Sequential walk through the H1'-H8/6 protons of P4 in [^{1}H,^{1}H]-NOESY spectra of (a) natural abundance P4 and (b) partially deuterated CPEB3. Intranucleotide cross peaks are labeled with the nucleotide number in black for nucleotides of the natural P4 sequence and in grey for the 2 additional nucleotides on each terminus (see Section 5.4). (c) Superposition of the spectra shown in (a) (dark grey) and (b) (light grey). The spectra were recorded at 25 °C in D_2O (100 mM KCl, 10 µM EDTA, pD 6.8).

correlations (83 total, 58 interresidue) are obtained between protons of the tetraloop, suggesting a well-defined structure. [^{1}H,^{1}H]-NOESY spectra of the exchangeable protons (Figure 5.9) confirm the formation of all nine base pairs in the P4 stem and contain cross peaks between U10H3 and C9H41/H42 and between G14H1 and H3, H5, H6 and H1' of U10. This means that U10 is pointing into the loop and probably stacking onto C9, which is supported by the observation of a cross peak between C9H6 and U10H6.

In the [^{1}H,^{1}H]-TOCSY spectrum (Figure 5.6), G11 and U13 H1'-H2' and H2'-H3' cross peaks are very intense revealing a C2'-*endo* sugar pucker conformation. For U10 and G12, it is evident from the TOCSY spectrum that the sugar pucker is neither C3'-*endo* nor C2'-*endo* (compare Section 4.3.1) but an intermediate conformation.

By superimposing the [^{1}H,^{1}H]-NOESY spectra of P4 and of the full-length CPEB3 ribozyme, it was possible to trace the sequential walk of the P4 nucleotides in the latter (Figure 5.5b and c). The proton chemical shifts of the P4 model construct and of the P4 domain in the ribozyme match well. This even applies to the protons of C3 and G20, which should have rather different environments in the artificially elongated P4 stem and at the junction to P1.1 and J2/4 in the entire ribozyme. This could be explained by stacking interactions between P1.1 and P4 that maintain a helical environment on both sides of the C3-G20 base pair. In general, the similarity of the P4 proton chemical shifts in the model hairpin and in the ribozyme are a good indication that the hairpin is formed with the same secondary and maybe even 3D structure in the model construct and within the CPEB3 sequence.

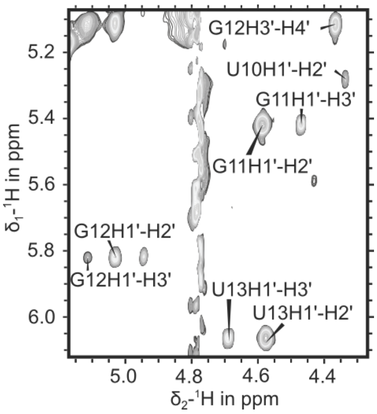

Figure 5.6: [^{1}H,^{1}H]-TOCSY cross peaks between ribose proton resonances of the UGGU tetraloop in the P4 model construct. The spectrum was recorded at 25 °C in D_2O (50 mM KCl, 10 μM EDTA, pD 6.8).

5.4.3 Resonance assignments in CPEB3 spectra

The three model constructs provided good starting points for the resonance assignment of the nonexchangeable protons of the CPEB3 ribozyme. The G3-G5 cross peak cluster of P1 and C4H6, A5H2, G6H8, and A7H2 resonances of P2 (Section 5.4.1) were easily identified, as they are shifted upfield, away from the most crowded region of the spectrum (compare Figures 5.4 and 5.11). In addition to the model constructs, we used a combination of labeling schemes to reduce spectral complexity. For example, F1,F2-[^{13}C,^{15}N]-filtered spectra of samples (Section 3.7.2) were recorded, in which either G and C were ^{13}C,^{15}N-labeled and A and U natural abundance or vice versa. In this way, the majority of peaks in the H1'-H6/8 sequential walk region could be assigned, encompassing nearly all residues of P2, P4, the J4/2 linker and the 5'-strand of P1. However, the assignment is interrupted at several positions in P3, L3 and P1.1. A Table of all assigned resonances can be found in Appendix 7.9.

The following analysis is thus focused on the [^{1}H,^{1}H]-NOESY spectrum of the imino protons of CPEB3 (Figure 5.7b), which is almost completely assigned in the H1 and H3 resonances and more suitable for assessing the secondary structure of CPEB3 than the NOESY spectrum of the nonexchangeable protons.

The P1, P2 and P4 constructs were very helpful for the assignment of the CPEB3 imino protons (Appendix 7.8, Figure 5.9b). Additionally, [^{1}H,^{15}N]-TROSY spectra of the N1H1 and N3H3 correlations (Figure 5.7a) permitted to distinguish guanines from uracils and the J_{NN} HNN-COSY spectrum (Appendix 7.10) of a sample being ^{13}C-^{15}N-labeled in its G and C residues was used to discriminate guanines in G-C base pairs from unpaired guanines or those in G·U wobble base pairs.

The G1·U36 wobble served as a good starting point for the assignment of the CPEB3 imino protons. From there on, G2 to G5 could be attributed through the spectrum of the P1 model construct (Appendix 7.8a). G30H1 does not correlate to any other proton than G31H1, which is expected due to the following single-stranded J1/2 linker (Figure 5.1). In P2, the H3 of the 3'-terminal U67, which has a single strong cross peak to G11H1 and the typical downfield shift of the 3'-terminal nucleotide was easily identified (compare Appendix 7.8b). Starting from this resonance, all remaining P2 imino protons could be assigned. The imino proton resonances of P4 are remarkably similar in the model construct and the full-length CPEB3, strongly facilitating the attribution. The fact that all expected correlations for P1, P2 and P4 are observed clearly demonstrates that the three longer helices and the thus the outer P1-P2 pseudoknot are formed in agreement with the proposed secondary structure.

There are two unassigned cross peaks (boxes in Figure 5.7b). One of them connects U62H3 or another resonance overlapped with U62H3 to a previously unassigned resonance, which belongs to a guanine(G_b)[1] in a G-C base pair in the J_{NN} HNN-COSY (Appendix 7.10). In the proposed secondary structure, only G17 would be a reasonable option for G_b, but then U61H3 should also display a cross peak to this proton, which is not the case.

Also, (G_aH1) at 13.42 ppm is in a G-C base pair according to the J_{NN} HNN-COSY. It seems to have a cross peak with either G56 or another unassigned resonance (Y) that overlaps with G56 in the proton dimension and could not be attributed to a uracil or guanine as there is no resolved peak in the TROSY spectrum. Among all unassigned Gs in G-C base pairs, G56 would only be close enough to G37 in P1.1, but it is unlikely that they would be correlated by such a strong cross peak, given that they are not direct neighbors and not part of the same helix.

In short, the extra cross peaks are not conclusive and only indicate that there are additional base pairs, namely, two more G-C pairs and possible a third one ($G_{d/e}$-C) with a very weak CN3-GH1 peak (Appendix 7.10).

Three more G-C base pairs would be expected for the P3 helix as well as a fourth one in P1.1, given that the proposed secondary structure is formed (Figure 5.3). The presence of extra G-C base pairs suggests that P3 is formed, but as informative correlations between the extra H1 resonances or to resonances of P2 are not available, it is not possible to proof this.

The [^{1}H,^{15}N]-TROSY spectrum (Figure 5.7a) is in very good agreement with the imino proton NOESY and the J_{NN} HNN-COSY, with the exception of the most downfield shifted uracil U61 at 14.75 ppm and G_b and $G_{d/e}$, whose NH peaks are missing or negligible. This is probably due to these residues being in non-rigid environments, such as the terminal base pair of P2.

---

[1] all resonances, which are not definitively assigned (G_a-G_g and U_a-U_e), are numbered by their proton chemical shift in the presence of 5 mM Mg^{2+} from low to high field (Figure 5.13).

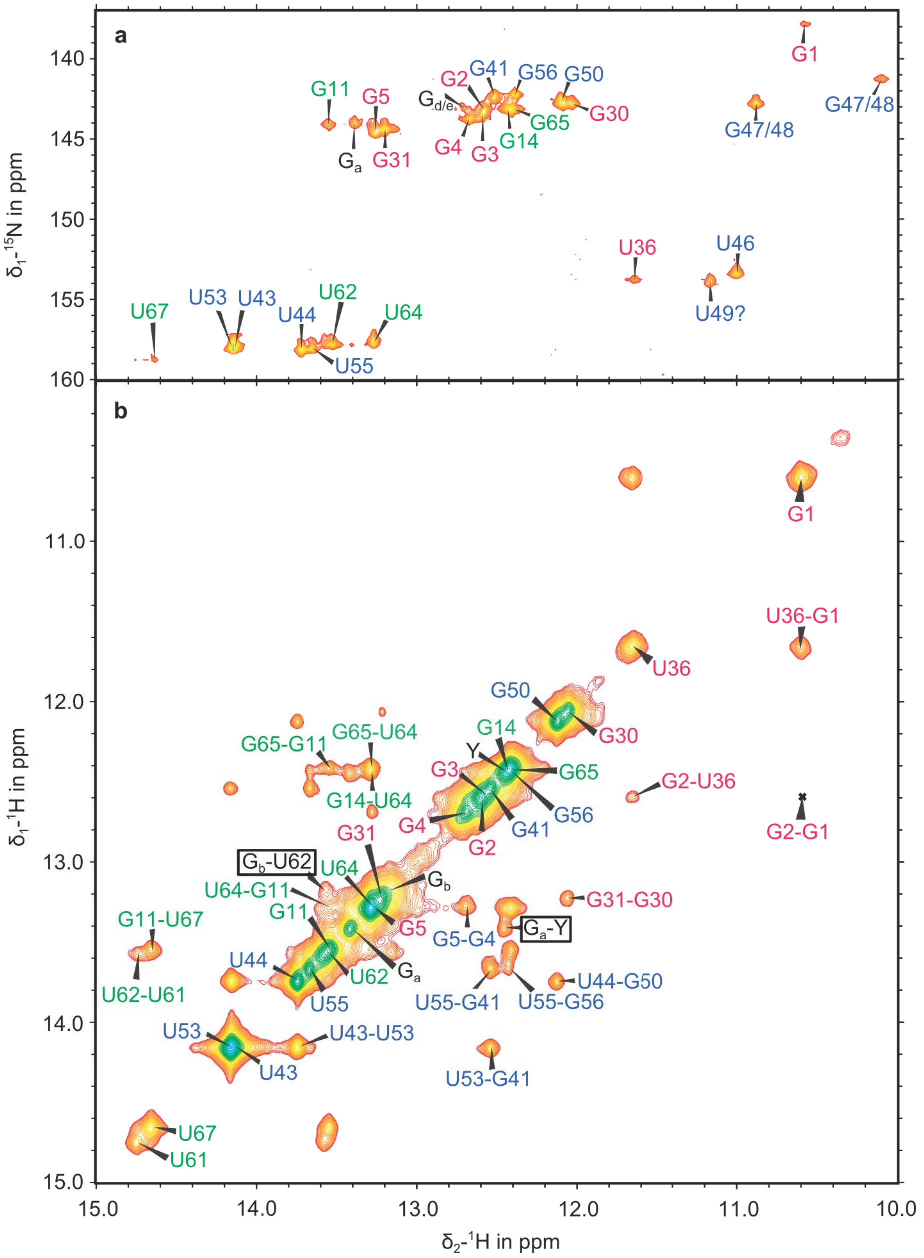

Figure 5.7: (a) [^{1}H,^{15}N]-TROSY and (b) [^{1}H,^{1}H]-NOESY correlations of the imino protons of the CPEB3 ribozyme. Peaks are labeled in the colors corresponding to the different helices P1, P2 and P4, as in Figure 5.3.

5.5 The solution structure of the P4 domain - a hairpin with a novel tetraloop structure

The P4 hairpin domain is the only domain of CPEB3 that is sequentially secluded; that means it is not involved in pseudoknot formation. In the crystal structures of the HDV ribozyme P4 protrudes from the otherwise compact pseudoknot core [38, 271, 292]. Shortening or deletion of P4 in the HDV ribozyme decreases but does not abolish catalytic activity [293], which probably applies to all HDV-like ribozymes [280, 282]. In conclusion, P4 and the catalytic core of the CPEB3 ribozyme are likely to adopt independent folds. We thus decided to undertake structure determination of the P4 model construct (Figure 5.3).

Tetraloops are generally a fascinating target of structural investigation, as they are a frequent feature in RNA structures and despite their small size, remarkably diverse in fold. The three main classes of tetraloops are UNCG, GNRA, and CUYG, where N represents any nucleotide, R represents a purine and Y a pyrimidine. Tetraloops mediate interactions between different RNA strands or molecules (as in kissing loops [34] and the GAAA-tetraloop-tetraloop receptor motif [39–42]) but they also serve as recognition sites for proteins [294].

Table 5.1: NMR restraints and and structural statistics for the P4 hairpin structure. Statistics are given for the 15 lowest energy structures out of 150 calculated. The table was taken from [26].

NOE-derived distance restraints	449
~ per nucleotide	20.4
~ intranucleotide ($j - i = 0$)	145
~ internucleotide ($k - i = 1$)	247
~ long-range ($n - i > 1$)	57
hydrogen-bond restraints	46
dihedral angle restraints	157
RMSD in Å for all heavy atoms vs. the mean structure	
global	1.24±0.48
stem (1-9,14-22)	1.07±0.43
loop (9-14)	0.16±0.06
loop (10-13)	0.15±0.08

The structure of the P4 construct was calculated based on the NOE-derived distance restraints, additional distance restraints for hydrogen bonds and dihedral angle restraints listed in Table 5.1. “The loop region is better defined than the stem with 20.75 NOEs per residue compared to 19 NOEs per residue in the stem (cross peaks between loop and stem residues not being counted). The 15 P4 conformers of lowest energy (Figure 5.8a) satisfy all distance and dihedral angle restraints within 0.2 Å/5°. All 15 structures in the ensemble adopt a stable and compact fold composed of the A-form helical stem and the very well-defined loop region (Figure 5.8b). The high convergence of the loop region among the structural ensemble is expressed in the strikingly low root mean square deviation of

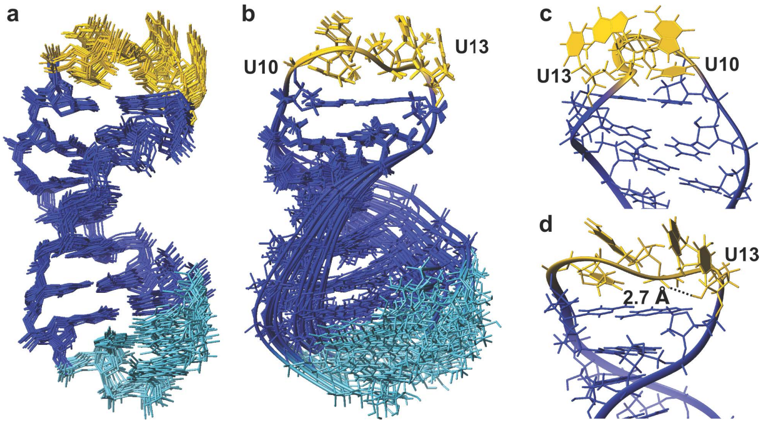

Figure 5.8: Solution structure of P4. The natural P4 stem nucleotides are colored blue, the tetraloop nucleotides (10-13) are colored yellow and the additional terminal guanines and cytosines are colored light blue. 15 lowest energy conformers of the CPEB3 P4 region (a) superimposed by all heavy atoms and (b) superimposed by the heavy atoms of residues 9-14. Due to the wealth of NOE correlations in the tetraloop (see main text) this region could be refined to high precision. (c-d) Details of the UGGU tetraloop structure: (c) The loop base U10 stacks onto C9 of the stem helix, while G11-U13 are exposed to the solvent, with their Watson-Crick edges facing to different sides. (d) Internal stabilization of the loop is achieved by stacking interactions and a putative hydrogen bond between G12O2P and U13OH2'. The Figure was taken from [26].

the loop residues compared to the ones of the entire construct and the helical stem alone (Table 5.1).

The conformation of the loop residues is such that U10, the first residue in the loop, points into the major groove of the stem helix and stacks onto C9. G11, in turn, stacks onto U10, having its Watson-Crick edge exposed to the solvent (Figure 5.8c). G12 and U13 also expose their Watson-Crick edges to the solvent but on the opposite side of the loop pointing towards the minor groove of C9-G14. The characteristic geometry of the loop is largely determined by both G11 and G12 being in a *syn* conformation and having γ angles in the unusual *trans* and *anti* range, respectively.

G11 and G12 have an S-type sugar pucker, the conformation of G11 is C2'-*endo* and the G12 C1'-*exo* sugar conformation is very similar to C2'-*endo*. This is typical for tetraloop structures, where the S-type conformation helps to expand the sugar-phosphate backbone and thus to bridge the two strands of the stem with only four nucleotides. In this special case, also U13 is in a C2'-*endo* conformation (see previous section). The unusually large chemical shift of the H2' of G12 (see previous section) is probably the result of ring current effects from the bases of G12 and U13. These are stacked on top of each other and G12H2' is situated directly next to them, [thus experiencing deshielding similar to the ring protons themselves. In contrast to this, the upfield shift of G11H4' might be the result of H4' being situated above the six-membered ring of the G14 base.] U13 is oriented perpendicular to G14, thus being in a rather exposed position (Figure 5.8c and d). Remarkably, the phosphate of U13 is also a point of a sharp directional change of the backbone (Figure 5.8c) and sticks out from the molecular surface (Figure 5.10b). Apart from the above-mentioned stacking interactions, the loop structure is stabilized by a hydrogen bond between a nonbridging G12 phosphate oxygen and the 2'-hydroxyl group of U13 (Figure 5.8d). This hydrogen bond might stabilize the highly unusual backbone trajectory that is not homogeneously curved, like most tetraloops but is instead indented in the direction of the helix axis (Figure 5.8d).

This tetraloop structure is markedly different from that of the main classes of tetraloops that have been investigated so far. The GNRA, UUCG and CUYG tetraloops all form a non-Watson-Crick base pair between the first and last nucleotide of the loop, such as the G·U wobble in the UUCG tetraloop and the sheared G·A base pair in the GAAA tetraloop. Such base pair formation can be excluded in the UGGU tetraloop as no NOEs were observed that indicate hydrogen bonding between U10 and U13 or stacking interactions of U13 and G14. Consequently, U10 and U13 are very distant, in perpendicular orientation to each other and on the other side of the sugar-phosphate backbone in the calculated structure. Also, we did not find any evidence for hydrogen bonding between amino protons and phosphate oxygens, which helps to stabilize the structures of several tetraloops such as the AGUU, GAAA and UUCG tetraloops [295–297]." [26]

5.6 Metal ion binding in the CPEB3 ribozyme

5.6.1 Mg^{2+} binding sites in the P1 and P2 model constructs

For both P1 and P2, the identification of Mg^{2+} binding sites is complicated by the strong metal ion binding site at the GAAA-tetraloop, which has been previously been described in several other constructs [182, 219, 298, 299]. The interaction of Mg^{2+} at the tetraloop of P1 is evident from the large, predominantly negative chemical shift changes throughout residues A10 to U13 (Appendix 7.11a) in the tetraloop and its closing base pair. Protons in the residues framing the tetraloop, such as in A8, C9 and U13H6 have large positive $\Delta\delta$ values. A very similar pattern of chemical shift changes is observed in P2, although with higher absolute $\Delta\delta$ values (see for example G10H2' and G14H1').

The remaining proton chemical shifts in P1 change only moderately. Protons of G1 also display somewhat higher chemical shift changes, which is likely due to Mg^{2+} binding to the 5'-triphosphate. The P1 helix therefore seems devoid of any specific Mg^{2+} binding site. In addition, a NOESY spectrum of the the P1 model construct in the presence of 1 mM $[Co(NH_3)_6]^{3+}$ (Section 3.7.4) was recorded (Appendix 7.12) to probe P1 for outer-sphere binding sites. Strong cross peaks of the $[Co(NH_3)_6]^{3+}$ protons are observed to G1H8, G2H8, G3H1, G3H8, G4H1, G4H8, G5H1, G9H8, A8H8C16 and C17H41, and weak cross peaks to G1H8, G2H1, C6H41, C6H42, G15H1 and C16H42. This confirms the metal ion binding sites at the tetraloop and at the 5'-end, though it reveals that there is a third binding site for $[Co(NH_3)_6]^{3+}$ at the level of G4/G5, in the middle of the P1 stem.

In the P2 stem, many resonances of protons distant from the tetraloop shift appreciably upon addition of 3 or 5 mM Mg^{2+}. In general, P2 proton resonances shift more than those of P1, which might be due to the lower KCl concentration in the P2 sample. The most pronounced shifts are observed for C4H6, A5H2, G6H8 and C17H6, U18H6 and G19H2'

(Appendix 7.11a), which reveals a Mg^{2+} binding site at the three central base pairs of P2. In fact, there are appreciable chemical shift changes occurring throughout the entire P2 construct. Also, the protons of A2H2', G3H8 exhibit moderate chemical shift changes and U15H6 a rather strong one. Presumably, this stems from overlapping effects of the three Mg^{2+} binding sites, which are the tetraloop, the central base pairs C4-G19, A5-U18, and G6-C17 and the 5'-triphosphate, since the construct is quite small.

Analysis of the chemical shift changes of the imino protons (Appendix 7.13) confirms the presence of three binding sites. The broadening of G1H1 and the pronounced shift of U21H3 (0.2 ppm) can be attributed to the effect of Mg^{2+} being bound at the 5'-end. Strong shifts are also observed for G10H1 (0.12 ppm) in the tetraloop and for U18H3 (0.15 ppm), which is supposed to be in the center of the stem binding site.

In summary, the data suggest only one Mg^{2+} binding site throughout the P1 and P2 domains of the CPEB3 ribozyme. This is the central base pairs of P2, at the residues C12-G14 and C63-G65. Additionally, a $[Co(NH_3)_6]^{3+}$ binding site is located in the P1 stem.

5.6.2 Specific binding of Mg^{2+} and $[Co(NH_3)_6]^{3+}$ to the loop and stem of P4

Chemical shift perturbation mapping of the P4 hairpin reveals three regions, which are most affected by the addition of Mg^{2+}. These are: (i) the first two nucleotides G1 and G2, (ii) A4 and G5 in the middle of the hairpin stem and (iii) G12 and G14 near the 3'-end of the tetraloop. "The chemical shift changes upon addition of 5 mM Mg^{2+} are shown in Figure 5.9a. G1 and G2 H8 and H1' resonances are broadened to baseline at 5 mM Mg^{2+}. Strong binding of Mg^{2+} at the 5'-terminal triphosphate with its high negative charge is expected and has been observed in a variety of other studies [185, 300, 301].

More interesting is the binding of Mg^{2+} to nucleotides A4 and G5, as indicated by the strong chemical shift changes observed upon Mg^{2+} addition (Figure 5.9a) and confirmed by the accumulation of negative charge in the major groove at the N7 and the nonbridging phosphate oxygens of A4 and G5 as well as G5O6 (Figure 5.10a). Mg^{2+} binding to this part of the stem also causes the strong chemical shift change of U19H6, as U19 forms a base pair with A4. This, however, seems to be an indirect effect of Mg^{2+} binding to G5 and A4 because neither U19 nor neighboring nucleotides form a cluster of negative charge. Also, the third Mg^{2+} binding site at U13 and G14 shows a high negative surface potential (Figure 5.10b). On addition of Mg^{2+}, resonances from nucleotides G12 and G14 are shifted significantly as are those from G11, U13 and A15, but to a lesser extent (Figure 5.9a). Accordingly, G11 and A15 marginally contribute to the negative charge cluster that likely attracts the metal ion, but as they are in the proximity of the G12/G14 binding site, they might be exposed to a different chemical environment in the absence and presence of Mg^{2+}.

To better pinpoint the metal ion binding site, we performed $[^1H,^1H]$-NOESY experiments with the P4 hairpin in the presence of 1.5 mM $[Co(NH_3)_6]^{3+}$. This stable, exchange-inert complex mimics the fully hydrated (hexaaqua) Mg^{2+} ion and is a commonly used mimic for outer-sphere coordination of Mg^{2+} [183, 302]. All protons of the ammine ligands resonate at one common frequency and NOE cross peaks can be detected between this resonance and different resonances of RNA protons in the $[Co(NH_3)_6]^{3+}$ binding site (Figure 5.9b).

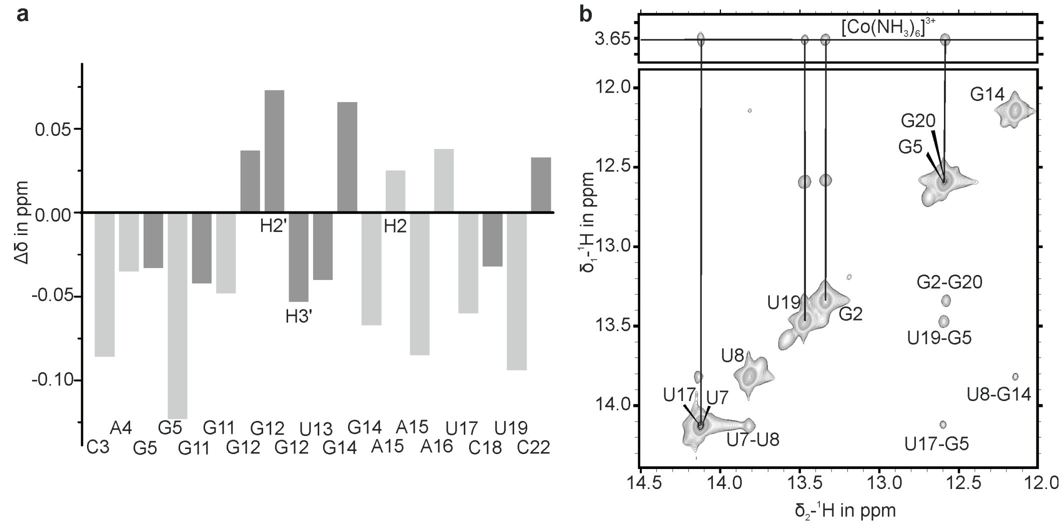

Figure 5.9: Locating Mg^{2+} binding sites in P4. (a) Chemical shift changes $\Delta\delta$ upon addition of 5 mM Mg^{2+} compared to δ in the absence of Mg^{2+}. Only residues with a $\Delta\delta$ of larger than 0.02 ppm are shown. Unless otherwise labeled, light grey bars represent $\Delta\delta$ of H6/H8 protons and dark grey bars $\Delta\delta$ of H1' protons. (b) [^{1}H,^{1}H]-NOESY spectrum of the exchangeable protons of P4 in the presence of 1.5 mM $[Co(NH_3)_6]^{3+}$ recorded in H_2O at 5 °C (50 mM KCl, 10 µM EDTA, pD 6.8). The figure was adapted from [26].

The $[Co(NH_3)_6]^{3+}$ titrations perfectly support the results from the Mg^{2+} titration described above for the two binding sites in the helical stem. Addition of $[Co(NH_3)_6]^{3+}$ leads to a broadening (G1H1), a change in chemical shift (G1H1', C22H1') as well as to cross peaks to RNA protons (G2H1 (Figure 5.9 b), G1H8, G2H8, C21H5 and G20H1' (data not shown)). Aside from Mg^{2+} binding to the 5'-triphosphate, specific outer-sphere coordination of Mg^{2+}/ $[Co(NH_3)_6]^{3+}$ also occurs within the stem. Distinct cross peaks between the protons of $[Co(NH_3)_6]^{3+}$ and G5H1, U17H3, and U19H3, all located in the stem helix on both strands, are detected (Figure 5.9b). The [^{1}H,^{1}H]-NOESY spectrum of the nonexchangeable proton region further confirms the existence of a specific Mg^{2+} binding site in the proximity of G5, corroborated by correlations with G5H8, A4H8 and C18H41 (in a base pair with G5) (data not shown).

The combined titration experiments described above support a specific outer-sphere coordination of Mg^{2+} in the central region of the P4 stem, which is known to occur in RNA A-form helices [83, 219]. In contrast, $[Co(NH_3)_6]^{3+}$ affects neither any exchangeable nor any nonexchangeable resonances of the UGGU tetraloop and the closing base pair. Consequently, Mg^{2+} binds most likely in a partly inner-sphere manner to the loop region, which cannot be mimicked by $[Co(NH_3)_6]^{3+}$. The sharp turn in the sugar-phosphate backbone at U13 causes all suitable ligands for Mg^{2+}, which are the phosphates of G12, U13 and G14, as well as G14N7 or G14O6, to be situated close to each other, too close, in fact, to accommodate the large $[Co(NH_3)_6]^{3+}$ complex." [26]

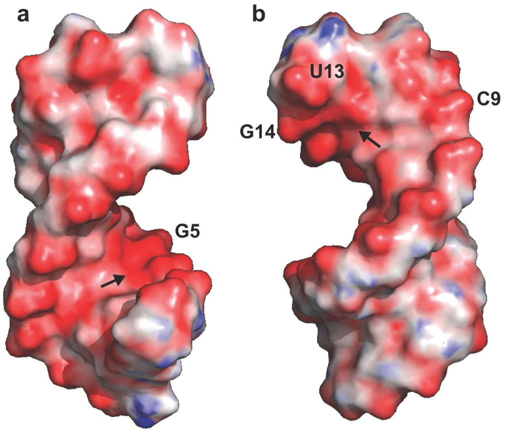

Figure 5.10: Electrostatic surface potential map of the P4 model construct. Clusters of negative charge formed by (a) the phosphate oxygens and major groove atoms at A4/G5 and (b) by major groove atoms of G14 and the phosphate oxygens of U13 in the tetraloop are marked by black arrows. The figure was adapted from [26].

5.6.3 Mg^{2+} and $[Co(NH_3)_6]^{3+}$ binding sites in the CPEB3 ribozyme as determined by NMR spectroscopy

Metal ion binding to CPEB3 was studied using NOESY spectra recorded in the absence and presence of Mg^{2+} or $[Co(NH_3)_6]^{3+}$, respectively. Figure 5.11 shows the spectrum at 0, 5 and 9 mM Mg^{2+}. Mg^{2+}-induced line broadening effects and chemical shift changes map to four main regions (see scheme on the right of Figure 5.11): the middle of the P2 helix; the upper part of the P4 stem and near the P4 loop, which is in line with the observations in the isolated P2 and P4 constructs; and the J4/2 linker, including the catalytic cytosine C57. In P1, only modest effects of Mg^{2+} are observed such as small chemical shift changes of G4H8. Interaction of Mg^{2+} with P1 thus seems to be weak, as predicted from the titrations of the P1 model construct. In the upper P4 stem, A40 and G41 are most affected by Mg^{2+} addition, confirming the existence of the outer-sphere binding site described above.

The J4/2 linker and P2 are quite strongly affected by Mg^{2+}-binding. Peaks of C12 in P2 and C57-A59 in J4/2 are broadened to baseline and A60H8 displays a strong downfield shift. It was demonstrated above that the P4 loop binds Mg^{2+} in a partly inner-sphere manner. Also, in the full-length ribozyme, shifts of G50 and A51 protons support the existence of this binding site.

NOESY spectra of the nonexchangeable (data not shown) and of the exchangeable protons were recorded in the presence of 1.5 mM $[Co(NH_3)_6]^{3+}$. The $[Co(NH_3)_6]^{3+}$ protons have cross peaks to G41H8, C54H6 and U55H3 (Figure 5.12) of P4 as well as to G2H1, G4H1 (Figure 5.12) and G5H8 of P1. Further cross peaks are observed between A60H1' and H8 in the J4/2 linker and between U36H3 and the $[Co(NH_3)_6]^{3+}$ protons, indicating one or two further $[Co(NH_3)_6]^{3+}$ binding site(s) near the active site. No cross peaks are observed to protons of the P4 tetraloop or to P2, indicating that both regions bind Mg^{2+} but not $[Co(NH_3)_6]^{3+}$, which suggests a partial inner-sphere coordination of Mg^{2+} at these sites.

The imino proton chemical shifts (Table in Appendix 7.9) are not much affected by the presence of 5 mM Mg^{2+} or 1.5 mM $[Co(NH_3)_6]^{3+}$ (Figure 5.12). This is not surprising, as their location in the helix center is rather far from potential metal ion attracting groups such as the phosphates or N7 or O6 of guanine. Selective broadening of cross peaks involv-

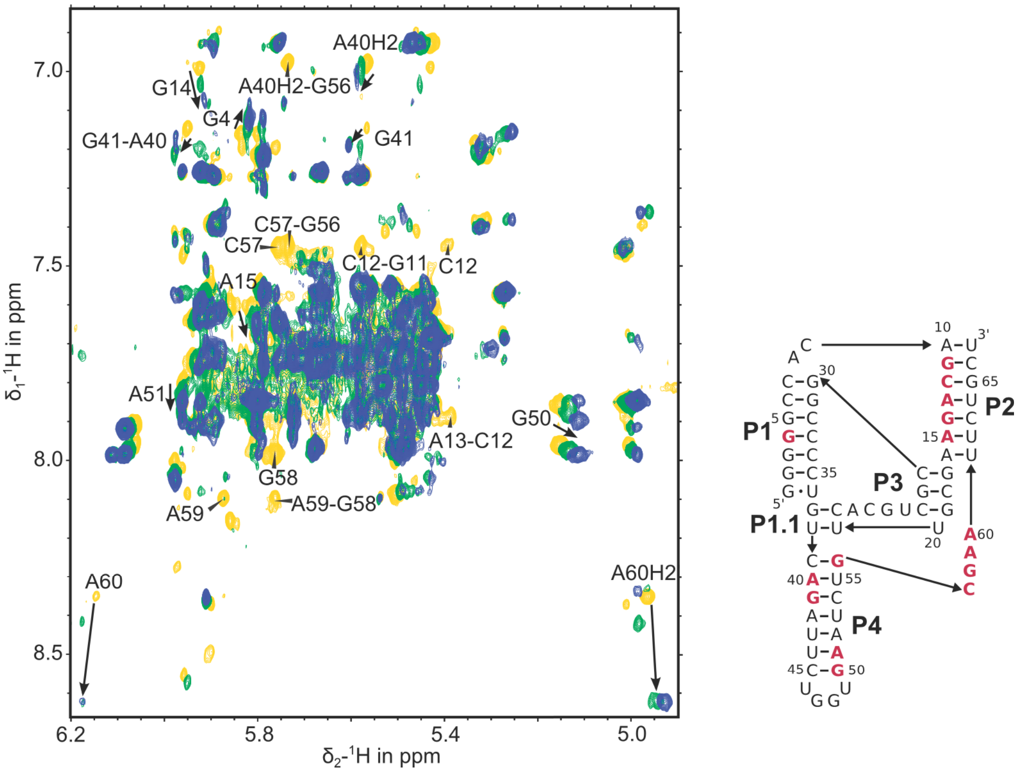

Figure 5.11: Mg^{2+} binding to the CPEB3 nonexchangeable protons. Superposition of the [^{1}H,^{1}H]-NOESY spectra of CPEB3 in the absence of Mg^{2+} (yellow), in the presence of 5 mM Mg^{2+} (green) and 9 mM Mg^{2+} (blue). Cross peaks displaying pronounced shifts (indicated by arrows) are labeled, as well as cross peaks broadened below the detection limit. Resonances in F2 belong to H1' and resonances in F1 belong to H6/8 unless otherwise indicated. All spectra were recorded at 25 °C in D_2O (100 mM KCl, 10 µM EDTA, pD 6.8).

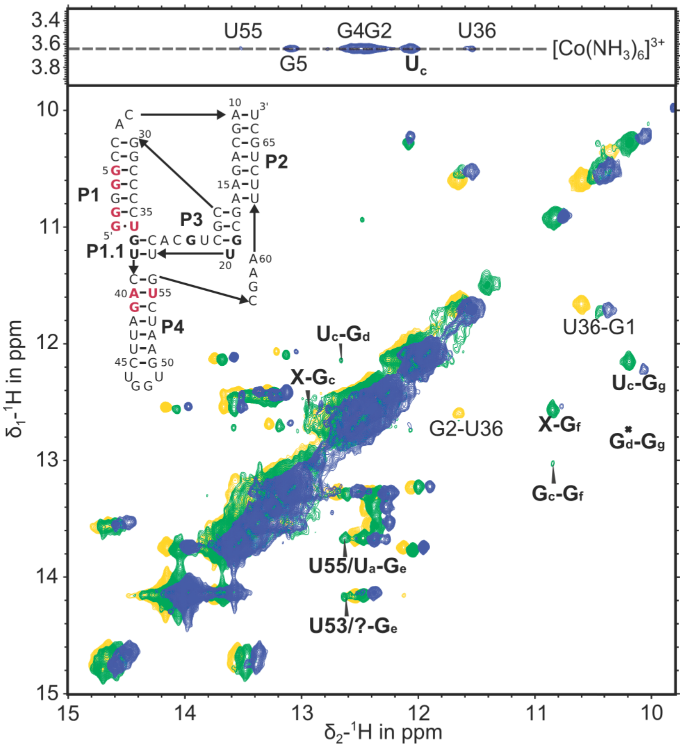

Figure 5.12: Mg^{2+} and [Co(NH$_3$)$_6$]$^{3+}$ binding to the CPEB3 imino protons. Superposition of the [^{1}H,^{1}H]-NOESY spectra of CPEB3 in the absence of any added metals (yellow), in the presence of 5 mM Mg^{2+} (green, shifted by -0.08 ppm in F2) and in the presence of 1.5 mM [Co(NH$_3$)$_6$]$^{3+}$ (blue, shifted by -0.16 ppm in F2). Upon addition of Mg^{2+}, new cross peaks appear (labeled in boldface). The G$_d$-G$_g$ cross peak is marked by an asterisk because its intensity is below the given threshold. On top, the spectral region containing cross peaks between [Co(NH$_3$)$_6$]$^{3+}$ and RNA protons is shown. In the insert, bold purple labels mark residues, whose resonances shift or broaden upon Mg^{2+} addition or display cross peak to [Co(NH$_3$)$_6$]$^{3+}$. Bold black labels mark the nucleotides proposed to contain the resonances that appear upon Mg^{2+} addition. All spectra were recorded at 5 °C in H$_2$O (100 mM KCl, 10 μM EDTA, pH 6.8).

ing U36H3 and G1H1 and G2H1 is observed upon addition of both metal ions, confirming that metal ion binding takes place at the G1·U36 wobble.

In summary, Mg^{2+} binding sites in the full-length CPEB3 ribozyme are located at the 5' G1·U36 wobble, in the upper P2 stem, in the J4/2 linker around the catalytic cytosine and in the P4 stem and loop. Among these, the P4 stem and the upper J4/2 linker also bind $[Co(NH_3)_6]^{3+}$, while the P1 stem seems to bind preferentially $[Co(NH_3)_6]^{3+}$.

New peaks emerge upon Mg^{2+} addition. Several new peaks appear in the NOESY and TROSY spectra on addition of 5 mM Mg^{2+} (marked by bold labels in Figure 5.12 and 5.13). In the TROSY spectrum, four new guanine NH correlations (G_c, G_e, G_f, G_g) and five new uracil NH correlations (U_a, U_b, U_c, U_d, U_e) are observed. In principle, there are six Gs (G17, G19, G25, G28 and G58) and four Us (U20, U21, U26, U38) in the sequence, which are not yet assigned. Including G_a, G_b and G_d, which were already observed in the absence of Mg^{2+}, there is at least one surplus correlation of both a uracil and a guanine. This might be the result of conformational exchange.

Four of the six extra guanines, G_a, G_b and G_d and G_e, seem to be in G-C base pairs according to the J_{NN} HNN-COSY (Appendix 7.10b). This is an important finding, given that four G-C base pairs are expected to be formed in for P3 and P1.1, respectively. Three guanines, G_c, G_f and G_g, are not base paired to cytosines. This means that there is one G too much, as only G59 in the single-stranded J4/2 linker and G25 (in the putative G25·U20 wobble base pair) are not in G-C base pairs (Figure 5.1a and b). None of the newly appearing UH3 correlate to an adenine H1 in the J_{NN} HNN-COSY (data not shown).

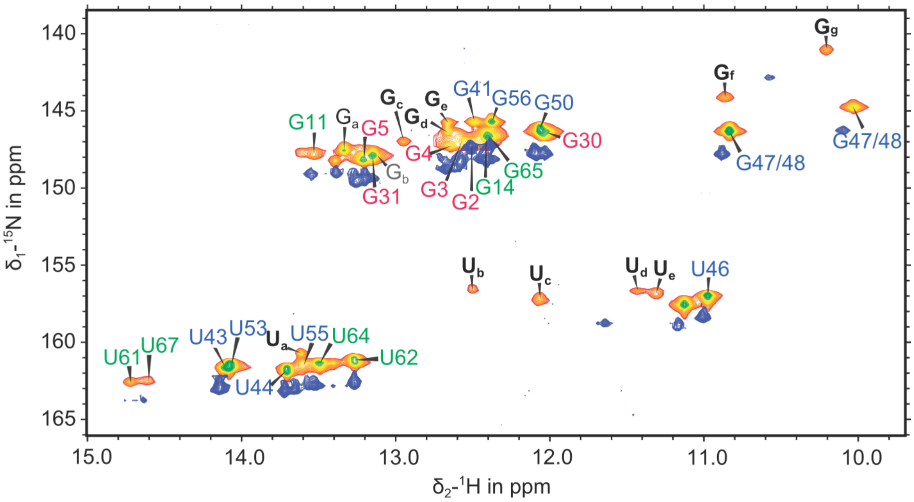

Figure 5.13: Mg^{2+}-induced changes in the $[^1H,^{15}N]$-TROSY correlations of CPEB3. The spectrum in the presence of 5 mM Mg^{2+} is shown in red-green and is superimposed with the spectrum recorded in the absence of Mg^{2+} (blue), which is shifted by 1.5 ppm in F1 for better comparison (see also Figure 5.7) Peaks appearing on addition of 5 mM Mg^{2+} are labeled bold, The G_bN1H1 cross peak is labeled grey as it cannot be precisely located. The spectrum was recorded at 5 °C in H_2O (100 mM KCl, 10 μM EDTA, pH 6.8).

The most intense cross peak appearing in response to the addition of Mg^{2+} or $[Co(NH_3)_6]^{3+}$ in the NOESY spectrum, is between a GH1 and a UH3 (U_c-G_g in Figure 5.12). Both resonances have correlations to G_dH1 and U_cH3 also has an NOE to the $[Co(NH_3)_6]^{3+}$ protons. The U_c-G_g cross peak is in a position typical for a G·U wobble pair and thus might indicate a new G25·U20 wobble formed below the P3 helix (with G_d being G19). Such a base pair that has been suggested based on observations in the crystal structure of the inhibited HDV ribozyme (Section 5.1.2).

In another newly appearing cross peak, X-G_f, X is either a uracil (U_b) or a guanine overlapped with G41, according to the TROSY correlations (Figure 5.13. Both X and G_f are correlated to another unpaired guanine G_c It is not clear which nucleotides could give rise to this cross peak, as the sequence does not contain unpaired guanines close to each other (see insert in Figure 5.12).

Furthermore, two cross peaks emerge, which correlate G_e with what seems to be U53 and U55 in P4. The P4 stem appears to be stably base paired according to all other imino proton correlations. Therefore, U53H3 and U55H3 should correlate solely to G41H1. If G41H1 was subject to conformational exchange and thus appearing as two resonances, this dynamic should also affect other P4 protons, which does not seem to be the case. As a consequence, these two cross peaks probably do not actually involve U53 and U55. Given that U55 is overlapped in the proton dimension with the newly appearing U_a, it is also possible that this is one more new correlation between a C-paired G and a uracil, which might fit to P1.1. In that case, U_a would be either U38 or U21 and G_e would be G37. Possibly, another uracil (U21/38) overlaps with U53 in both the proton and nitrogen dimension, explaining the second cross peak of G_e.

In conclusion, the effect of Mg^{2+} on the NH and NOE correlations of the imino protons demonstrates metal ion binding at G1·U36 and, more importantly, proves that Mg^{2+} binding has more impact on the CPEB3 structure than simply binding to isolated sites in P2, L4 and J4/2.Extra base pairs are formed, constituting further Mg^{2+} binding sites in the inner pseudoknot of the ribozyme. Several observations make a strong case for the secondary structure shown in Figure 5.1c being formed on addition of Mg^{2+}: (i) the NOE correlations and hence the secondary structure in P1, P2 and P4 remain unaffected upon addition of Mg^{2+}, (ii) four additional unassigned G-C base pairs (as expected in P3 and P1.1), but no additional U-A base pairs are observed (iii) NH correlations for additional Gs and Us not in Watson-Crick base pairs and several new NOE correlations between the extra Gs and Us appear, indicating a general gain of order in the ribozyme core.

However, conclusive NOE correlations between the extra G-C base pairs and the extra GH1-GH1 and GH1-UH3 cross peaks cannot be observed, so the attributions proposed above and thus the formation of the proposed secondary structure remain unproven. In addition, the observation of at least one surplus GN1H1 and UN3H3 correlation suggests dynamics in the ribozyme structure giving rise to more than one resonance for one G and one U residue. It should be noted in this context, that some of the newly appearing NOE correlations might actually be exchange peaks, which makes a correct attribution even more complicated.

5.6.4 Tb^{3+}-induced cleavage studies reveal metal ions in the P3-P1.1 pseudoknot.

Tb^{3+}-induced RNA cleavage experiments represent a very different experimental approach to identify Mg^{2+} binding sites. They were performed to complement the interpretation of the NMR titration data on Mg^{2+} binding. In the case of the CPEB3 ribozyme, they are of special relevance for obtaining data on metal ion binding sites in the inner pseudoknot (P1.1, P3, L3), which is lacking a reliable resonance assignment or contains resonances too strongly overlapped for tracing metal-induced chemical shift changes.

Lanthanide ions are assumed to occupy the same binding sites as Mg^{2+} in RNA molecules but bind with an affinity that is at least three orders of magnitude higher [303,304]. Mainly Tb^{3+} and Eu^{3+} ions have been used to detect metal ion binding sites in proteins and nucleic acids and are often employed as a mimic for Ca^{2+} or Mg^{2+} ions [172, 305, 306]. Based on these experiments, the use of Tb^{3+} for RNA structure mapping was established [171, 307]. When Tb^{3+} is added to a folded ribozyme, it binds to the RNA upon displacement of Mg^{2+}. The $Tb(OH)aq^{2+}$ complex abstracts a proton from the 2'-OH of the nearest nucleotide, thereby promoting backbone cleavage by nucleophilic attack. The resulting fragments of the ribozyme can then be used to identify the binding sites. The number of detected cleavage sites strongly depends on the amount of Tb^{3+} added. At lower micromolar concentrations, as used in our studies, only high-affinity binding sites are subjected to cleavage, while at millimolar Tb^{3+} concentrations, all single-stranded regions are cleaved. In this work, a 5'-^{32}P-labeled human CPEB3 RNA was used for cleavage studies. The fragments generated by incubation of the folded ribozyme with micromolar concentrations of $TbCl_3$ were separated by PAGE and and visualized by phosphorimaging.

Analysis of the gel (Figure 5.14) clearly indicates three main regions of Tb^{3+}-induced cleavage: the P2 helix near C12, the tetraloop of the P4 helix and several positions throughout the core of the ribozyme encompassing P1.1, P3, L3 and the upper part of P4. The most intense cleavage bands are those of the junction of P4 to J4/2 (G56, C57) and of P1.1/L3 (C22, A23). The detected cleavage sites in P2 and P4 are far from each other and from the core of the ribozyme in the secondary structure. As a consequence, they probably represent two distinct, isolated binding sites. In the ribozyme core, cleavage occurs at many nucleotides, which would be suspected to be rather close in the folded ribozyme. Most probably, some of these nucleotides bind the same Tb^{3+} ion. Therefore, the exact number of binding sites can not be deduced from these data.

The fact that the active site cytosine C57 in the postcleavage ribozyme is affected by Tb^{3+}-induced cleavage shows that Mg^{2+} binds to the active site also in the absence of the -1 nucleotide. The results obtained by Tb^{3+}-induced cleavage are in good agreement with the Mg^{2+} binding sites that were localized by NMR spectroscopy (Sections 5.6.1, 5.6.2, 5.6.3) but do not confirm the $[Co(NH_3)_6]^{3+}$ binding sites. Both Mg^{2+} and Tb^{3+} bind at C12 (C4 of P2) and in L4, while neither of the two seem to have a high affinity for the middle base pairs of P1 or the P4 stem, where $[Co(NH_3)_6]^{3+}$ binds. Thus, the geometry, which favors outer-sphere interactions in these sites does not allow the Tb^{3+}-induced self-cleavage reaction of the RNA [308].

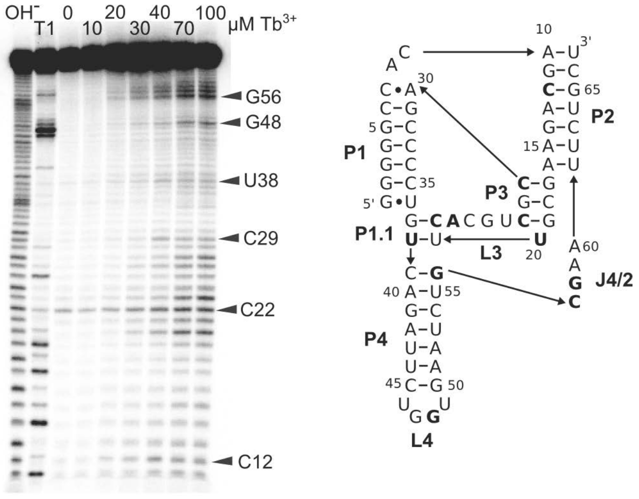

Figure 5.14: Mg^{2+} binding sites in the CPEB3 ribozyme mapped by Tb^{3+}-induced cleavage. The CPEB3 RNA (in 25 mM MOPS, 100 mM KCl, 20 mM $MgCl_2$, pH 7) was incubated with $TbCl_3$ for 30 min at RT. The cleavage products were separated by 16 % PAGE. The position belonging to the observed cleavage sites was determined with the help of the T1- and the OH^- ladder.

5.6.5 Stoichiometry of Mg^{2+}-to-CPEB3 binding

The number of Mg^{2+} ions bound to CPEB3 was determined by two different methods: by equilibrium dialysis in combination with atomic absorption spectroscopy (AAS) and by using the Mg^{2+}-binding fluorescent dye HQS.

The equivalents of Mg^{2+} bound to the CPEB3 ribozyme determined by both methods are listed in Table 5.2. Four ions are counted by both methods at a KCl concentrations of 100 mM or 2 M in the buffer. This is a good indication that these four Mg^{2+} ions being counted are sufficiently restricted in their diffusion and not diffusing in the ion cloud surrounding the ribozyme. At 50 mM KCl in the buffer, 4.4 ions are counted, which reflects a higher proportion of Mg^{2+} in the ion cloud [309].

It is not straightforward to relate this number to the binding sites identified by NMR and Tb^{3+}-induced cleavage studies. Tight and partly solvent protected Mg^{2+} binding would be expected in the active site (at G1·U36, C57) and probably somewhere in the inner pseudoknot at P3 or P1.1. Also, the ions in L4 and P2 might be counted due to their inner-sphere interactions, while sites preferring outer-sphere contacts probably would not, because this interaction mode often allows metal diffusion to a certain degree.

Table 5.2: Number of Mg^{2+} ions bound to CPEB3. Values represent averages and maximum error of two measurements.

$c(K^+)$ in mM	ratio Mg^{2+}:CPEB3	
	equilibrium dialysis	HQS fluorescence
50	4.41 ± 0.05	4.36 ± 0.24
100	3.95 ± 0.25	4.13 ± 0.32
2000	3.96^a	4.33 ± 0.08

[a] only one measurement was performed

5.6.6 Mg^{2+} induces a compaction of the CPEB3 ribozyme.

To investigate the effect of K^+ and Mg^{2+} concentration on the dimensions of CPEB3, a sample of human CPEB3 was titrated with increasing amounts of K^+. At 100 mM K^+, additional Mg^{2+} was titrated to the sample. After each addition of K^+ or Mg^{2+}, a DOSY spectrum was acquired, from which the hydrodynamic radius r_H was calculated (Table 5.3). This experiment is used to indirectly assess the amount of secondary and tertiary interactions formed from the r_H of the ribozyme, and therefore reports on the conditions required to achieve a compact fold.

Clearly the ribozyme is not properly folded in the absence of significant amounts of counterions and the very large hydrodynamic radius of 3.91 nm is probably an averaged value of different extended states. 10 mM K^+ are not sufficient to compact the ribozyme fully, which is not surprising given the rather intricate pseudoknot topology of CPEB3. A strong compaction is already achieved in the presence of 100 mM K^+ alone, but even low concentrations of Mg^{2+} further reduce r_H. At 2 mM Mg^{2+} and higher, the changes in r_H become smaller and between 10 and 20 mM Mg^{2+} concentration, there is no difference anymore within the error limit. We repeated the titration on the chimp variant of the CPEB3 ribozyme, thereby confirming the trend observed, but obtaining slightly smaller r_Hs (Appendix 7.14).

In another experiment, the NMR sample was treated and spectra were acquired in exactly the same way but the sample was re-annealed after the addition of different amounts of Mg^{2+}. This did not affect the change in r_H, indicating all interaction sites between the ribozyme and Mg^{2+} that mediate the compaction are accessible without prior disruption of the secondary structure.

Table 5.3: Hydrodynamic radius r_H of the human CPEB3 ribozyme in the presence of different concentrations of K^+ and Mg^{2+} as determined through DOSY (D_2O, pD 6.8, 25 °C). All values are averages of three integrated regions with one standard deviation.

c(K^+) in mM	c(Mg^{2+}) in mM	$r_H \pm 1\sigma$ in nm
0	0	3.91±0.03
10	0	3.38±0.03
100	0	2.83±0.01
100	2	2.56±0.02
100	5	2.53±0.02
100	10	2.45±0.02
100	20	2.44±0.02

To understand which of the measured radii realistically reflects the dimension of CPEB3 according to the secondary structure, we estimated the theoretical r_H of the CPEB3 ribozyme. A straightforward calculation of the theoretical r_H is not possible in this case, as the maximum length or width of the CPEB3 structure are not known and cannot be estimated as simply as for a duplex or a hairpin [310]. To obtain an estimate, we made the assumptions that the ribozyme has a length *a*, corresponding to at least 19 base pairs (the sum of the number of base pairs in P2, P3, P4 and P1.1, Figure 5.3), and perpendicular to *a* a width b of about twice the diameter of an RNA helix. With 0.26 nm being the distance between two base pairs and 2.4 nm being the diameter in a standard A-form RNA helix this results in $a = 18 \cdot 0.26$ nm = 4.68 nm and $b = 2 \cdot 2.4$ nm = 4.8 nm. As the ratio between b and a is lesser than 2, a spherical model can be applied [311,312] to the ribozyme structure, in which r_H is defined as half of the longer distance in the structure. Consequently, the results suggest that 2.34 nm $\leq r_\mathrm{H}$(CPEB3) $\leq$ 2.4 nm.

Compared to this approximated r_H, the experimentally determined hydrodynamic radii appear reasonable and the values obtained in the presence of K^+ and Mg^{2+} seem more realistic than those obtained in K^+ alone. It can thus be concluded that divalent metal ions are required to achieve the native fold of the CPEB3 ribozyme. Recent studies on the influence of molecular crowding agents on the size and activity of human CPEB3 have shown that the dimension of the ribozyme in 10 mM Mg^{2+} is equivalent to the size in the presence of 0.5 mM Mg^{2+} and molecular crowding agents [313]. This indicates that the r_H we determined in 10-20 mM Mg^{2+} might actually reflect the physiological one.

5.7 Discussion

5.7.1 The postcleavage CPEB3 ribozyme has a robust global fold

The results clearly show that the outer P1-P2 pseudoknot and P4 of the CPEB3 ribozyme are formed in monovalent metal ions alone and obey the secondary structure predicted by Salehi-Ashtiani et al. [92]. These three domains constitute the largest part of the ribozyme sequence and are fixed in their orientation due to the pseudoknot topology and the relatively short linkers. As a consequence, the global shape and dimensions of the CPEB3 ribozyme are largely determined in 100 mM KCl, which is in agreement with the hydrodynamic radius obtained. The folding of the outer pseudoknot and P4 is robust in the postcleavage ribozyme, as neither the 2D-NMR spectra, the DOSY data, nor the native gels indicate any significant populations of unfolded or mispaired sequences or refolding over time. The formation of stable mispaired intermediates, as previously reported for the HDV ribozyme [314, 315], does not seem to take place in the postcleavage CPEB3 ribozyme.

Whether or not the inner pseudoknot is fully base paired in the absence of Mg^{2+}, remains open. Possible structures in monovalent ions complying with our data would consist of either P1, P2 and P4, with an incomplete P3; or of P1, P2, P4 with single base pairs being formed in both P3 and P1.1; or of all five helices being formed but mobile relative to each other and more distant than in the native state. Also, formation of P1, P2 and P4 with a mispaired P3-L3 region cannot be ruled out.

5.7.2 Mg^{2+} binding sites in CPEB3

Mg^{2+} promotes additional interactions in the ribozyme core. The pronounced impact of Mg^{2+} on the CPEB3 ribozyme is undeniable. The addition of millimolar concentrations makes the ribozyme more compact and leads to additional structure being formed in the ribozyme core. A compaction along the longitudinal axis could result from coaxial stacking of P1, P1.1 and P4 and P2 and P3, respectively, as it is observed in the HDV ribozyme crystal structures [38, 271, 292]. Compaction in the transverse would be achieved by relieving backbone repulsion between P1/P1.1 and P2/P3, or by stabilizing the inner pseudoknot. Certainly, Mg^{2+} in the ionic atmosphere surrounding CPEB3, plays an important role for the compaction of the ribozyme [56, 250], but a thorough treatment of this effect is beyond the scope of this thesis. The following discussion focuses on the site-bound (partly chelated) or diffusion-restricted (glassy) Mg^{2+} ions (Section 3.5.1), which are observed by NMR and Tb^{3+}-induced cleavage and assesses their structural relevance.

As we have already confirmed that at least the outer pseudoknot is formed in exactly the same way as in the HDV ribozyme, it is reasonable to compare the structure and metal ion binding sites of CPEB3 to the corresponding data on the HDV ribozyme.

As mentioned above, the most obvious interpretation of the NMR data recorded in the presence of Mg^{2+} is the formation of the secondary structure shown in Figure 5.1b.

In the HDV ribozyme, the G25·U20 wobble is thought to present the catalytically active Mg^{2+} ion to G1 and to the active site cytosine, C75 [271] (Figure 5.15a and b (ion number 1)). This ion is suggested to be coordinated via water molecules in the minor groove of the G25·U20 wobble and via inner-sphere contacts to the pro-R_p phosphate oxygen of G1 and C75. Consequently, this ion holds the J4/2 linker, the stem of P1 and L3 together.

Mg^{2+} binding to the analogous nucleotides in the CPEB3 ribozyme (red in Figure 5.15c) would explain some of the new NOE cross peaks (such as U_cH3-G_gH1 in Figure 5.12)) and the strong broadening of C57 and G58 resonances we observe upon Mg^{2+} addition. This interpretation is supported by our finding that $[Co(NH_3)_6]^{3+}$ binds in the same site, which is consistent with the data on the HDV ribozyme. $[Co(NH_3)_6]^{3+}$ is suggested to be able to substitute Mg^{2+} in the active site of the HDV ribozyme [276, 292], thereby inactivating it [275]. If we are indeed observing the formation of the G25·U20 wobble and the inner pseudoknot, this raises the question of why conclusive NOE correlations of the P1.1 and P3 imino protons cannot be detected.

One reason for this is Mg^{2+}-induced line broadening, which affects protons in the Mg^{2+} binding site. Mg^{2+} binding might stabilize P1.1 and P3, but at the same time cause the disappearance of the corresponding NOE cross peaks (as it is the case for G1, G2 and U36 in Figure 5.12), despite a sufficiently short distance between the protons. This possibility is supported by the Tb^{3+}-induced cleavage data, which strongly suggest that Mg^{2+} binds to both P3 and P1.1.

Another possible reason for expected NOE cross peaks being absent would be dynamics within the ribozyme core, which is discussed below.

Our data suggest that there is another common Mg^{2+} binding site of the CPEB3 and the HDV ribozyme. In the HDV ribozyme crystal structure there is a Mg^{2+} ion bound in between the sugar-phosphate backbone of the upper linker adenines and the P1 stem (ion number 2 in Figure 5.15a). According to the NMR data of the CPEB3 ribozyme, the corresponding sites are both in contact with $[Co(NH_3)_6]^{3+}$. Possibly water-mediated coordination of Mg^{2+} between J4/2 and P1 (blue site in Figure 5.15c), helps to overcome backbone repulsion, and thereby promotes a compact structure of the catalytic core region of both ribozymes.

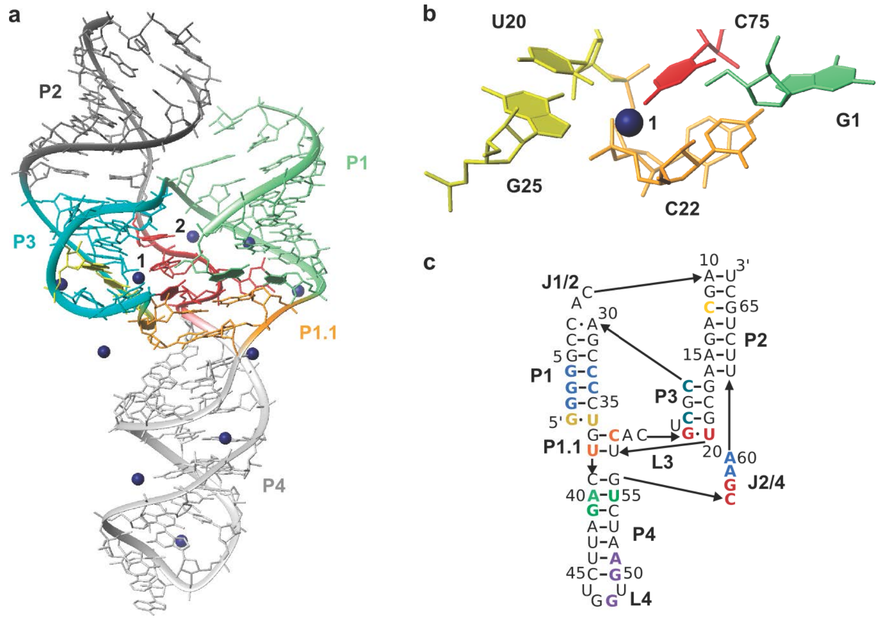

Figure 5.15: Location of metal ion binding in the HDV and CPEB3 ribozymes. (a-b) Crystal structure of the inhibited HDV ribozyme. Mg^{2+} ions are shown as dark blue spheres, J4/2 is shown in red and the G25·U20 wobble is shown in yellow. Shown is (a) the full structure and (b) a close-up of the active site. The figure was adapted from pdb entry 3NKB [271]. (c) Mg^{2+} binding sites in the CPEB3 ribozyme. Each color stands for one binding site; red corresponds to ion number one and blue to ion number two in (a).

Which are the four Mg^{2+} determined by ion counting? Apart from the two binding sites discussed above, there is evidence for up to six other Mg^{2+} binding sites (Figure 5.15c) in the CPEB3 ribozyme.

Molecular dynamics studies have revealed diffuse binding of a hydrated Mg^{2+} ion to the major groove of the G1·U37 wobble in the HDV ribozyme [316]. The line broadening of peaks belonging to the cleavage site G1·U36 wobble and the NOEs between $[Co(NH_3)_6]^{3+}$ and U36H3, suggest that this binding site is also present in the CPEB3 ribozyme (khaki in Figure 5.15 c). Additionally, we have observed Mg^{2+} binding in the P4 tetraloop, the P4 stem (violet and green in Figure 5.15c) and in P2 (yellow in Figure 5.15c). As discussed above, P3 seems to contain another binding site (blue-gray in Figure 5.15c), which cannot be precisely located from our data. This also applies to the putative binding site in P1.1 (orange in Figure 5.15c).

Although a total of eight potential binding sites were determined, it is highly unlikely that all of these would be detected by the ion counting techniques employed, as they could also involve water-mediated contacts, as for example the binding site at the G1·U36 wobble and in the P4 stem. Such contacts can be partly diffuse and are thus not necessarily captured by the ion counting methods. It is thus reasonable that approximately four ions, which have a more site-bound character, are being counted in 50 or 100 mM KCl. Those might likely be ions in bound to the ribozyme core, which are more solvent protected, such as the G25·U20 wobble-binding site or the binding sites in P3 and P1.1.

It is surprising, though, that four ions are counted in the presence of 2 M KCl. At 2 M KCl, all Mg^{2+} ions, which are not highly chelated and well shielded from the solvent (Section 3.5.2) are supposed to be outcompeted by K^{+} [317]. It seems impossible that the comparably small CPEB3 structure could accommodate four such binding sites. For comparison, the 158 nt P4-P6 segment of the *Tetrahymena thermophila* group I intron, binds only two Mg^{2+} ions in high monovalent salt concentrations, a number, which was determined by the same approach as the one used here [317]. In the light of these facts, the number of four ions bound to the CPEB3 ribozyme seems realistic at 50-100 mM KCl, but is surprisingly high at 2 M KCl.

Dynamics in the ribozyme core As mentioned above, a possible reason for the absence of NOE correlations between the P3 and P1.1 imino proton resonances is dynamics in the inner pseudoknot, which would make NOE contacts within the shorter, less stable P1.1 and P3 helices and between helices difficult to observe. The appearance of surplus N1H1 and N3H3 correlations on addition of Mg^{2+}, supports the idea of conformational exchange taking place. This could also explain, why some correlations appearing at 5 mM Mg^{2+}, such as X-G_f cannot be reasonably attributed (Section 5.6.3). If conformational exchange is slow compared to the difference in resonance frequency of the proton in the two conformations of the RNA, exchange cross peaks between the two frequencies can be detected in a NOESY spectrum, but cannot be discriminated from actual NOE cross peaks without additional data.

The suggestion of the inner pseudoknot of the CPEB3 ribozyme being flexible is buttressed by the fact that L3 in the HDV ribozyme has a certain degree of disorder in all published crystal structures (1CX0 [38], 1SJ3 [292] and 3NKB [271]) (as reflected by higher B-factors than in P2 and P4, for example). This is corroborated by MD simulations [278] that have proven L3 to be flexible.

One might speculate that a certain plasticity in the inner pseudoknot is required for ribozyme activity. It has been shown that the CPEB3 ribozyme is active in up to 4 M urea [92], and that HDV-ribozyme self-cleavage is stimulated by the addition of up to 5 M urea or 10 M formamide [318, 319]. Under these conditions, P1.1 – and possibly P3 – should be denatured, while P1, P2 and P4 structure (Section 5.7.1) should remain base paired and hold the ribozyme together. In 9.5 M urea or 22.5 M formamide, that is in fully denaturing conditions, the HDV ribozyme is not active anymore, which underscores the importance of a stable outer pseudoknot for catalysis.

5.7.3 P4 - a new tetraloop structure and a protein binding site?

“By NMR, we solved the solution structure of a well-defined and conserved fragment of the human CPEB3 ribozyme, the P4 hairpin and for the first time characterized the structure of a UGGU tetraloop in detail. UGGU tetraloops have been found to appear in targets of the *Saccharomyces cerevisiae* endonuclease Rnt1p [320]. Rnt1p recognizes many of its targets by interactions with AGNN tetraloops [321] but also UGNN tetraloops are recognized [295, 320]. The most similar tetraloop sequence, of which a 3D structure is available, and which is found in an Rnt1p target, is the AGUU tetraloop [295]. Comparing the structures of the UGGU and the AGUU tetraloop (Protein Data Bank ID 1K4B), we find that both loops have an S-shaped backbone trajectory (Figure 5.16) as seen from the top, with the first two and last two loop bases pointing to opposite sides of the helix. Also, the second loop residue (G11 in P4) being the conserved guanine is in a *syn* conformation and has a similar position and orientation in both loops, which is an important determinant for recognition by Rnt1p [295,321,322], and is also found in the AGUC and AGAA tetraloops that serve as recognition sites for Rnt1p [322]. The crystal structure of a 32mer hairpin containing the AGAA tetraloop bound to the RNA-binding domain of Rnt1p revealed that the *syn*-guanine is important for the overall fold of the tetraloop, which is recognized by Rnt1p [323] rather than the *syn*-guanine itself.

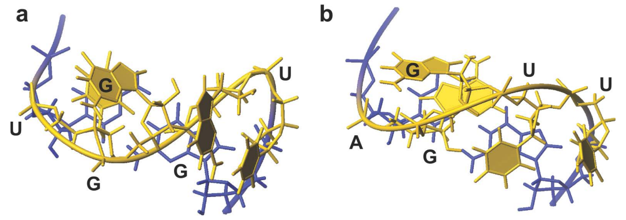

Figure 5.16: Comparison of the UGGU and the AGUU tetraloop structures: View down the stem helix axis of (a) the UGGU tetraloop in P4 and (b) the AGUU tetraloop (prepared from pdb entry 1K4B [295]). The Figure was taken from [26].

Of all available tetraloop sequences, the UGUU tetraloop [324] is the most similar one. This tetraloop also plays a role in RNA-protein interaction; it is found in hepatitis beta virus encapsidation signals and mediates the initiation of replication when it is bound by the viral reverse transcriptase [325]. Despite the large sequence similarity of the two tetraloops and their closing base pair (cUGGUg vs cUGUUg), the tetraloop fold is remarkably different. The guanine in UGUU is in an *anti* conformation and the first and last uracils form a buckled *cis*-wobble base pair. The only common features are the stacking of the first uracil on the adjacent cytosine in the hairpin stem and the distribution of the first two bases pointing towards the major groove of the stem and the third loop base pointing towards the minor groove. It is quite striking how much structural variation is introduced by the substitution of a single nucleobase. This underlines the variability of RNA folding even in such small motives as a tetraloop.

Another interesting aspect of the UGGU loop structure is the fact that it forms an inner-sphere binding site for Mg^{2+} that probably stabilizes this particular fold of the tetraloop. This feature, the similarity to the AGNN tetraloop, the sequence conservation of P4 between mammalian transcripts [despite the dispensability for self-cleavage activity [280]], and the fact that it is the only protuberant domain of the otherwise very compact ribozyme structure, point out that P4 has some functional relevance, for example, as an interaction site with a protein or RNA binding partner. [For instance, such an interaction might adjust self-cleavage activity of the ribozyme to the *cpeb3* transcript concentration required in different tissues (see Section 5.1.1).] However, up to date there is no biological or biochemical data on the function of this region that could support this hypothesis.

Apart from the tetraloop itself, also the P4 stem deserves some attention, as it is very close in space to the active-site cytosine C57 (Figure 5.1b). With regard to this, it is possible that the metal ion coordination at A4 and G5 might be relevant for the active-site structure. To further investigate this, we analyzed different crystal structures of the HDV ribozyme that have the same general secondary structure as the P4 region directly preceding the catalytic cytosine. In the structures of the precleavage HDV ribozyme [271] and of the C75U mutant [292] there is a major-groove binding site, accessible for both Mg^{2+} and $[Co(NH_3)_6]^{3+}$ in the upper part of the P4 stem. The respective Mg^{2+} ion is rather far from C75, but still close enough to interact with the phosphates of C41 and A42 of the P1.1 region and thus might support the continuous stacking interactions between P1, P1.1 and P4, which are present in the HDV ribozyme. A similar function of the P4 stem Mg^{2+}-binding site in the CPEB3 ribozyme seems reasonable to suggest." [26]

5.7.4 Conclusion

Mg^{2+} is of crucial importance for the CPEB3 ribozyme to access the intricate double-pseudoknot secondary structure underlying its native fold. This is achieved by making the overall ribozyme more compact and by enabling specific interactions between residues in the core region of the ribozyme, where catalysis occurs. The data presented here extend the parallels between CPEB3 and HDV, as they provide evidence for Mg^{2+} binding to several corresponding sites in both ribozymes, in particular, to a catalytically important G·U wobble at the base of P3. As mentioned before, the HDV-like ribozymes are special among the small self-cleaving ribozymes regarding the complexity of their fold and the need for divalent metal ions in catalysis. Despite their small size, it appears that the HDV-like ribozymes resemble more to the large ribozymes, in which the native fold and the catalytic mechanism are coupled by their requirement for specific interactions with Mg^{2+}. It seems paradoxical that Mg^{2+} also appears to give rise to dynamics in the ribozyme. This underscores the need for further investigations of the interplay of Mg^{2+} and the nested double-pseudoknot structure, especially addressing conformational changes during catalysis.

5.8 Accession codes

Structure coordinates and NMR restraint files of P4 have been deposited to the PDB with the accession code 2M5U. ^{1}H chemical shifts of P4 have been deposited to the BMRB with the accession code 19081.

6 Experimental Section

6.1 Material & Instruments

6.1.1 Chemicals

^{32}P-γ-ATP	PerkinElmer, Switzerland
AccuGel (29:1 acrylamide:bisacrylamide)	National Diagnostics, UK
BIAnormalizing solution for SPR	GE Healthcare, UK
D_2O	Armar Chemicals, Switzerland
DCl	Armar Chemicals, Switzerland
DNA templates	Microsynth, Switzerland
HQS	Fluka/Sigma-Aldrich, Switzerland
LongRanger acrylamide solution	Cambrex Bio Sciences, USA
NaOD	Armar Chemicals, Switzerland
NTPs, natural abundance	GE healthcare/Roth, Switzerland
NTPs, (5, 3', 4',5', 5")-deuterated	Cambridge Isotope Laboratories Ltd., USA
NTPs, uniformly ^{13}C,^{15}N-labeled	Silantes GmbH, Germany
Pf1 filamentous bacteriophages	ASLA Biotech Ltd., Latvia
T4 polynucleotide kinase	Promega, USA
TSAP	Promega, USA
Ultima Gold XR scintillation fluid	Canberra Packard, USA

All other chemicals were purchased at the highest purity grades (puriss p.a. or molecular biology grade) from Fluka/Sigma-Aldrich, Brunschwig Chemie, Merck AG (Switzerland) or Acros Organics, (Belgium).
All samples, buffers and reactions were prepared in deionized, millipore-filtered water. In addition, solutions were autoclaved (if possible) and/or sterile filtered before use to prevent RNA degradation.

6.1.2 Buffers

transcription buffer 40 mM Tris-HCl (pH 7.5), 40 mM DTT, 2 mM spermidine, stored at -20 °C
TBE buffer for denaturing PAGE and electroelution 90 mM Tris-HCl (pH 8.3), 90 mM boric acid, 0.2 mM EDTA
urea loading buffer for denaturing PAGE, 2x 11.8 M urea, 8.3 % sucrose, 4.2 mM Tris-HCl (pH 7.5), 0.83 mM EDTA (pH 8), 0.083 % XC, 0.083 % BB, stored at 4 °C
formamide loading buffer for denaturing PAGE, 2x 82 % formamide, 10 mM EDTA (pH 8), 0.16 % XC, 0.16 % BB, stored at 4 °C

native PAGE buffer 66 mM HEPES, 34 mM Tris-HCl, 50 mM KCl (pH 7.2), (5 mM Mg acetate)
SPR running buffer 10 mM MOPS, 107 mM KCl, 0.05 % Polysorbate 20 (pH 6.8)
ME buffer 10 mM MOPS, 1 µM EDTA (pH 6.5), stored at 4 °C
crush & soak buffer 10 mM MOPS, 1 mM EDTA, 250 mM NaCl (pH 6.5), stored at 4 °C

6.1.3 RNA and DNA constructs

d3'EBS1: 5'-GGAGUAUGUAUUGGCACUGAGCAUACUCC-3'
d3'EBS1-4U-biotin: 5'-GGAGUAUGUAUUGGCACUGAGCAUACUCCUUUU-3'-biotin
d3'EBS1wt: 5'-GGAGUAUGUAUUGGAAAUGAGCAUACUCC-3'
d3'EBS1-4U-biotin: 5'-GGAGUAUGUAUUGGAACUGAGCAUACUCCUUUU-3'-biotin
IBS1: 5'-CAGUGUC-3'
IBS1wt: 5'-CAUUUUC-3'
dIBS1: 5'-CAGTGTC-3'
dIBS1wt: 5'-CATTTTC-3'
CPEB3, human: 5'-GGGGGCCACAGCAGAAGCGUU
CACGUCGCAGCCCCUGUCAGAUUCUGGUGAAUCUGCGAAUUCUGCU-3'
CPEB3, human, elongated: 5'-GGGAUCAAGGGGAUAACA
GGGGGCCACAGCAGAAGCGUUCACGUCGCAGCCCCUGUCAGAUUCU
GGUGAAUCUGCGAAUUCUGCU-3'
CPEB3, chimp: 5'-GGGGGCCACAGCAGAAGCGUU
CACGUCGCGGCCCCUGUCAGAUUCUGGUGAAUCUGCGAAUUCUGCU-3'
CPEB3, chimp, elongated: 5'-GGGAUCAAGGGGAUAACA
GGGGGCCACAGCAGAAGCGUUCACGUCGCGGCCCCUGUCAGAUUCU
GGUGAAUCUGCGAAUUCUGCU-3'
CPEB3, chimp, extra base pair in P1.1, P4 stem shortened:
(39U>A, 42A>C, 43Udel, 44Udel,51Adel,52Adel, 53U>G)
5'-GGGGGCCACAGCAGAAGCGUUCACGUCG
CGGCCCCUGACAGCCUGGUGGCUGCGAAUUCUGCU-3'
CPEB3, chimp, GC-to-AU mutation in P1:(4G>A, 33C>U)
5'-GGGAGCCACAGCAGAAGCGUUCACGUCG
CGGCUCCUGUCAGAUUCUGGUGAAUCUGCGAAUUCUGCU-3'
P1: 5'-GGGGGCCAGAAAUGGCCCCU-3'
P2: 5'-GAGCAGAACGAAAGUUCUGCUC-3'
P4: 5'GGCAGAUUCUGGUGAAUCUGCC-3'

6.1.4 Instruments

NMR spectra were recorded on a Bruker Avance 500 MHz spectrometer with a 5 mm CRYO QNP probehead with z-gradient coil, a Bruker Avance 600 MHz spectrometer with a 5 mm CRYO TCI inverse triple-resonance probehead with z-gradient coil or on a Bruker Avance 700 MHz spectrometer with a 5 mm CRYO TXI inverse triple-resonance probehead with z-gradient coil (all: Bruker Biospin AG, Switzerland). NMR data were processed using TopSpin version 3.0 or 3.2 (Bruker Biospin AG, Switzerland).

SPR data were recorded on a Biacore T100 system (GE Healtcare, UK). UV-absorption measurements were performed on Cary 100 UV/Vis and Cary 500 scan UV/Vis-NIR (both: Varian Inc, USA) and Lambda 25 UV/Vis (PerkinElmer, USA) spectrophotometers and on a NanoDrop microvolume UV/Vis spectrophotometer (Thermo Fisher Scientific Inc., USA). Pictures of analytical PAGE gels were taken with a Bio-Vision 3026 WL/LC/26Mx gel imaging system (Vilber Lourmat, France).

Quantification of radiolabeled RNA was done using a Tri-Carb scintillation counter 22000CA Liquid Scintillation (Canberra Packard, USA). Phosphorimaging was performed on a Typhoon scanner FLA 9000 (GE Healthcare, USA). HQS fluorescence was measured on a Varian Cary Eclipse fluorescence spectrometer (Varian Inc, USA). AAS was perfomed on a Varian SpectraAA 110 spectrometer (Varian Inc, USA).

6.2 NMR sample preparation

RNA samples were produced by *in vitro* transcription following standard procedures [326]. Reaction mixtures typically contained 4.5-6 mM of each NTP, 0.9-1.2 μM of each strand of the synthetic, PAGE-purified, double-stranded DNA template [326], 30-50 mM $MgCl_2$, 40 mM Tris-HCl (pH 7.5), 40 mMDTT, 2 mM spermidine and 0.01 % Triton X. T7 Polymerase for transcription was made in-house; according to the activity of each batch, different amounts were used for transcription reactions. Transcription reactions were typically left to proceed for 6 h. RNA was precipitated and PAGE-purified on gels containing 7 M urea, TBE and 15-18 % acrylamide/bisacrylamide (AccuGel) (12 % for CPEB3 samples); bands were UV-shadowed, excised and subjected to electroelution in a Whatman elutrap system (Whatman, UK) to recover the RNA from the gel.

The RNA was desalted and concentrated by ultrafiltration in Vivapsin®devices (Sartorius Stedim Biotech GmbH, Germany; 2000 Da MWCO for P1, P2 and P4, 3000 Da MWCO for d3'EBS1, 5000 Da MWCO for CPEB3) by washing with 5 volumes of 1 M KCl, pH 8 and 7 volumes of water. dIBS1 was bought HPLC-purified and was desalted using illustra™ NAP-10 columns (GE Healthcare, UK). The nucleic acid concentration was determined by UV-absorption measurements using molecular extinction coefficients ϵ_{260} of (303 $mM^{-1}cm^{-1}$ (d3'EBS1), 63.9 $mM^{-1}cm^{-1}$ (dIBS1), 203.4 $mM^{-1}cm^{-1}$ (P1), 212 $mM^{-1}cm^{-1}$ (P2), 281.5 $mM^{-1}cm^{-1}$ (P4), 725 $mM^{-1}cm^{-1}$ (CPEB3). d3'EBS1·dIBS1 samples were prepared by adding dIBS1 to d3'EBS1 in an excess of 10 % to avoid the presence of any unbound d3'EBS1. All samples contained 0.2-0.9 mM RNA 10 μM EDTA, 100-110 mM KCl (CPEB3 and d3'EBS1·dIBS1, P1), 20-50 mM KCl (P2-P4) and were adjusted to a pH or pD of 6.8, respectively[1]. RNA samples were annealed by heating them to 85-90 °C for 1-2 min and then rapidly cooling them on ice. Prior to NMR data acquisition, samples were dissolved in 100 % D_2O or 90 % H_2O/10 % D_2O.

---

[1] The pD is measured by adding 0.4 units to the pH meter reading [327].

6.3 NMR spectroscopy

For all measurements, 5 mm Shigemi tubes were used. 4,4-dimethyl-4-silapentane-1-sulfonic acid (DSS) was used as an external, direct reference for ^{1}H resonances and as an external, indirect reference for ^{13}C and ^{15}N resonances [328]. All samples contained 0.4-0.9 mM of construct being either natural abundance RNA (DNA), partially deuterated ([5, 3', 4',5',5"]-^{2}H) RNA or uniformly ^{13}C,^{15}N-labeled RNA.

Nonexchangeable proton resonances were assigned from [^{1}H,^{1}H]-NOESY spectra, typically recorded with a mixing time of 250 ms at 25 °C, in 100 % D_2O. Water suppression was achieved using presaturation pulses. To aid the assignment, additional spectra of the same kind were acquired at 20 or 30 °C or with mixing times of 60 or 120 ms. Furthermore, [^{1}H,^{1}H]-NOESY and [^{1}H,^{1}H]-TOCSY spectra with a [^{13}C,^{15}N]-filter in F1 and F2 [163] were recorded of d3'EBS1·dIBS1 samples containing natural abundance dIBS1 and ^{13}C,^{15}N-labeled d3'EBS1 and of G,C-[^{13}C,^{15}N]-labeled CPEB3 samples to select for correlations of the natural abundance components.

Exchangeable proton resonances were assigned from [^{1}H,^{1}H]-NOESY spectra with a WATERGATE pulse sequence for water suppression recorded at 5 °C with a mixing time of 150 ms, in 90 % H_2O/10 % D_2O. Of d3'EBS1·dIBS1, the same spectra were also recorded at 20 °C, to facilitate comparison with the nonexchangeable proton resonances. [^{1}H,^{1}H]-TOCSY spectra with a mixing time of 50 ms were recorded in 100 % D_2O at 25 °C for the assignment of pyrimidine H5-H6 correlations and to assess sugar puckers.

^{13}C resonances of d3'EBS1 were assigned from [^{1}H,^{13}C]-HSQC spectra recorded at 25 °C. ^{15}N resonances of d3'EBS1 were assigned from SOFAST [^{1}H,^{15}N]-HMQC spectra (d3'EBS1·dIBS1) or [^{1}H,^{15}N]-TROSY spectra (CPEB3) recorded at 5 °C in 90 % H_2O/10 % D_2O.

Base pair formation was verified by recording J_{NN} HNN-COSY [161] spectra at 5 °C in 90 % H_2O/10 % D_2O.

All processing was done in TopSpin 3.0 or TopSpin 3.2. (Bruker Biospin AG, Switzerland), all assignments were made in Sparky (`http://www.cgl.ucsf.edu/home/sparky/`).

6.3.1 RDC measurements

RDCs for d3'EBS1·dIBS1 were determined from a series of J-modulated [^{1}H,^{13}C]-HSQC spectra according to [329], which was recorded both in the absence and in the presence of ca. 17 mg/mL Pf1 bacteriophage. Peak intensities in each spectrum were determined in the program CCPNmr Analysis [330] and fit with the program gnuplot (`http://www.gnuplot.info`) to obtain J. The RDC is calculated as $\Delta J = J_{\mathrm{phages}} - J_{\mathrm{w/o\ phages}}$.

6.3.2 DOSY measurements of the CPEB3 ribozyme

To determine the diffusion coefficient D and hydrodynamic radius r_{H} of CPEB3, DOSY experiments with excitation sculpting water suppression were recorded with a diffusion delay Δ of 400 ms and a gradient duration d of 2 ms at 25 °C in D_2O. The gradient strength was raised incrementally from 1.7 to 32.4 G/cm in 56 steps. The peak areas at each point of gradient strength were determined in TopSpin. By plotting $\ln \frac{A}{A_0}$ against the square of the gradient strength (G_z) and fitting to a straight line, the diffusion coefficient can be obtained from

$$\ln \frac{A}{A_0} = -(\gamma d)^2(\Delta - \frac{d}{3}){G_z}^2 \tag{6.1}$$

where γ = 2.675222005·10^{-8} rad^{-1} T^{-1} is the proton gyromagnetic ratio. The hydrodynamic radius is then calculated according to the Stokes-Einstein equation

$$r_H = \frac{k_b \cdot T}{6 \cdot \pi \cdot \eta \cdot D} \tag{6.2}$$

where k_B = 1.3806488·10^{-23} J/K is the Boltzmann constant and $\eta_{\mathrm{D_2O}}$ = 1.0998 mPa is the viscosity of D_2O at 25 °C.

6.3.3 Metal ion titrations

Mg^{2+}-induced chemical shift perturbations of d3'EBS1·dIBS1 were obtained by titrating a sample with increasing amounts of $MgCl_2$ (0, 0.5, 1, 1.5, 2, 3, 4, 5, 6, 8, and 10 mM), recording a [^{1}H,^{1}H]-NOESY spectrum in each step. Following assignment of all spectra, chemical shift changes were analyzed by creating bar plots in gnuplot. $[Co(NH_3)_6]^{3+}$-induced chemical shift perturbations of d3'EBS1·dIBS1 were determined in the same way titrating a sample with 0, 0.5, 0.75, 1.25 and 2 mM $[Co(NH_3)_6]Cl_3$. Paramagnetic line broadening of d3'EBS1·dIBS1 was assessed by titrating a sample with increasing amounts of $MnCl_2$ (0, 20, 40, 60, 80, 100 µM) recording a [^{1}H,^{1}H]-NOESY spectrum in each step. Spectra were superimposed in Sparky to visually assess line broadening.

Mg^{2+}-induced chemical shift perturbations of the nonexchangeable protons of the P1, P2 and P4 model constructs were determined as described for d3'EBS1·dIBS1, titrating samples with increasing amounts of $MgCl_2$ (0, 0.5, 1.5, 3 and 5 mM for P1, 0, 1, 2, 3, 5 and 7 mM for P2, 0, 0.5, 1, 1.5, 2, 2.5, 3.5, 5, 8, 12 and 18 mM for P4). Mg^{2+}-induced chemical shift perturbations of the exchangeable protons of the P2 model construct were obtained by titrating a sample with increasing amounts of $MgCl_2$ (0, 1, 2, 3, 4, 5, 6.5, 8, 9 mM), recording a 1D-^{1}H spectrum in each step and analyzing chemical shift perturbations in TopSpin.

K^+- and Mg^{2+}-induced changes of the hydrodynamic radius of CPEB3 were determined by titrating a sample with increasing amounts of KCl and $MgCl_2$ (0, 10, 100 mM of KCl plus 2, 5, 10, 20 mM of $MgCl_2$) recording a DOSY experiment in each step. D and r_H were calculated for each concentration as described in the previous section. Prior to data acquisition, the pD was readjusted after having reached 100 mM KCl, and 10 and 20 mM $MgCl_2$, respectively. In addition, the RNA was re-annealed (Section 6.2) after both additions of KCl.

6.4 Structure calculation and analysis

Interproton distances were estimated from [^{1}H,^{1}H]-NOESY spectra (25 °C, 250 ms mixing time and 5 °C and 20 °C (d3'EBS1), 150 ms mixing time). The peak volumes of the nonexchangeable protons were integrated using Sparky (`http://www.cgl.ucsf.edu/home/sparky/`), excluding strongly overlapped peaks. Calibration of the interproton distances was done with the program DYANA [331], using fixed distances such as the H5-H6 distances in pyrimidines (2.4 Å) and the H1'-H2' distances (2.8-3.0 Å). Cross peaks were assigned to either of the four categories: strong (1.8-3.0 Å), intermediate (1.8-4.5 Å), weak (3-6 Å) or very weak (4-7 Å).

The intensity of intraresidue H1'-H2' cross peaks in [^{1}H,^{1}H]-TOCSY spectra was used to obtain sugar pucker torsional angle restraints (Section 3.7.1). Residues with very intense H1'-H2' cross peaks (A10, U11, U12 of d3'EBS1·dIBS1 and G11 and U13 of P4) were confined to south/C2'-*endo* conformation (δ= 145, $\nu1$ = 25, $\nu2$ = $-35 \pm 20°$) residues with absent cross peaks were restrained to north/C3'-*endo* conformation (δ = 85, $\nu1$ = -25, $\nu2$ = 37 $\pm20°$) (Figure 3.8b). For residues with intermediate cross peaks (G1, C29 of d3'EBS1·dIBS1 and G1, U10, G12 and C22 of P4) no sugar pucker restraints were set. For all residues, which belong to helical regions and have a C3'-*endo* sugar pucker, the backbone torsion angles α, β, γ, ϵ and ζ (Figure 3.8a) were set to the average values of an typical A-form helix (α = -62, β = -180, γ = 48, ϵ = -152, ζ = -74, $\pm10°$ for d3'EBS1·dIBS, α = -68, β = 178, γ = 54, ϵ = -153, ζ = -71, $\pm20°$ for P4). The spectral data of the dIBS1 residues, were not finally conclusive regarding the sugar conformation or backbone geometry (Section 4.3.1). For this reason, β, γ, ϵ, δ, $\nu1$ and $\nu2$ were not restrained. χ angles were set according to the intensity of the intraresidue H1'-H8/6 cross peaks in [^{1}H,^{1}H]-NOESY spectra with 60 ms mixing time (Figure 3.8a and Section 3.7.1) to either $60\pm20°$ (G11 and G12 of P4) or $-160\pm20°$ for RNA residues and to $-120\pm40°$ for DNA (dIBS1) residues. For d3'EBS1·dIBS, α and ζ angles of all residues not constrained to A-form geometry were set to $0\pm120°$ to exclude the *trans* range, as no downfield shifted resonances were observed in a 1D-^{31}P spectrum [157]. The 1D-^{31}P spectrum of P4 contained resonances between 0-1.5 ppm. α and ζ angles were therefore left unrestrained.

Base pairs, whose formation was validated by the presence of characteristic interstrand [^{1}H,^{1}H]-NOESY cross peaks (Figure 3.8d), were maintained by applying distance restraints between donor hydrogen and acceptor atoms and between donor and acceptor atoms and by enforcing planarity. 200 starting structures were calculated from the extended RNA (and DNA) chain(s), by rMD with CNS version 1.21 [158, 332]. All restraints except for RDCs were applied in this step, which contains a high temperature stage of 40 ps at 20000 K, followed by two cooling stages of 90 ps in torsional space and 30 ps in cartesian space. The resulting structures of lowest energy (20 structures in the case of d3'EBS1·dIBS1 and 15 in the case of P4) were refined by 88 ps of rMD cooling from 3000 K to 50 K using the program XplorNIH version 2.3 [159, 160]. In this step, 21 [^{1}H,^{13}C] RDCs were included in the structure calculation of d3'EBS1·dIBS1. The PALES program [333] was used for obtaining an estimation of the axial and rhombic component of the alignment tensor, which were then determined more precisely by an extensive grid search [334] to be

27.3/0.08. During the refinement, the force constant for the RDCs was gradually increased from 0.01 kcal $mol^{-1}Hz^{-2}$ to 1 kcal $mol^{-1}Hz^{-2}$.
Since some of the refined structures of d3'EBS1·dIBS1 from the 19th conformer on contained one or more NOE violations, the 18 conformers of lowest energy, which satisfied all given restraints, were subjected to further analysis. Of P4, the 15 lowest energy structures out of 150 refined were further analyzed. Analysis of the structure ensembles was mainly done using the program MOLMOL [335], the electrostatic surface potential was determined with the PDB2PQR v1.8 web server [336, 337] (`http://nbcr-222.ucsd.edu/pdb2pqr_1.8/`) and visualized with APBSTools2 v1.4.1 in the program Pymol. The sugar puckers and backbone geometry of d3'EBS1·dIBS were evaluated with the help of the web servers web3DNA [338, 339] and PROSIT (`http://cactus.nci.nih.gov/prosit/`).

6.5 Calculation of the d3'EBS1·dIBS1 structure with bound $[Co(NH_3)_6]^{3+}$ ions

"In order to localize binding sites for $[Co(NH_3)_6]^{3+}$-ions in d3'EBS1·dIBS1, $[^1H,^1H]$-NOESY spectra of d3'EBS1·dIBS1 were recorded in the presence of 1 mM $[Co(NH_3)_6]^{3+}$ (for the non-exchangeable protons, 25 °C) and 1.5 mM $[Co(NH_3)_6]^{3+}$ (exchangeable protons, 5 °C). Cross peaks between RNA or DNA protons and $[Co(NH_3)_6]^{3+}$ protons were assigned in Sparky. All nucleic acid protons displaying such cross peaks to the ammine protons were clustered according to their position in the solution structure calculated in the absence of $[Co(NH_3)_6]^{3+}$ (Table 6.2). For rMD calculations of the structures with bound $[Co(NH_3)_6]^{3+}$, a loose distance restraint of 3-7 Å between the Co^{3+} central ion and each nucleic acid proton displaying an NOE cross peak to the ammine protons was added in the refinement. Because all ammine protons of $[Co(NH_3)_6]^{3+}$ resonate at one common frequency and therefore cannot be distinguished, the distance to the Co^{3+} central ion was used for the restraints [182]. In the resulting ensemble, the six out of 10 lowest energy conformers that had no violations of NOE or dihedral angle restraints were used for further analysis." [25]

Table 6.2: Definition of the $[Co(NH_3)_6]^{3+}$ binding sites for rMD calculations of d3’EBS1·dIBS1 with three $[Co(NH_3)_6]^{3+}$ ions bound. All protons displaying a cross peak to hexamminecobalt(III) are sorted into three different binding sites combining protons situated close to each other in the calculated structure without metal ions. The table was taken from [25]

binding site 1		binding site 2		binding site 3	
d3’ stem		lower loop, dIBS1 5’ end		dIBS1 and EBS1, 5’ end	
A3	H1’	U11	H1’	G13	H1
A3	H2’	U11	H6	T62	H3
G4	H1	G19	H1’	T62	CH_3(71-73)
G4	H8	G19	H8	T64	H3
U5	H3	A20	H2	T64	CH_3(71-73)
U5	H6	C59	H1’	C65	H5
A6	H1’	C59	H2”	C65	H6
U24	H1’				
U24	H6				
C26	H1’				
U27	H3				

6.6 SPR sample preparation and measurements

“d3’EBS1/d3’EBS1wt coupled to biotin via a four-uracil 3’-overhang were purchased PAGE-purified from IBA GmbH (Göttingen, Germany) and used as ligands. (d3’EBS1/d3’EBS1wt)-4U-biotin was immobilized on a Series S Sensor Chip SA (GE Healthcare) pre-coated with Streptavidin on a carboxymethyldextran surface or on a carboxymethyldextran hydrogel chip (XanTec bioanalytics, Düsseldorf, Germany), coated with neutravidin in our laboratory. The surface was pre-treated with 3-5 injections of 1 M NaCl, 50 mM NaOH lasting 50 s at a flow of 30 µL/min. Immobilization was carried out by injecting 200 µg/mL (d3’EBS1/d3’EBS1wt)-4U-biotin for 10 min at a flow of 5 µL/min. All experiments were performed in 10 mM MOPS, 107 mM KCl (I = 110 mM), 0.05 % Polysorbate 20, pH 6.8. The dIBS1 and dIBS1wt DNA and IBS1 and IBS1wt RNA 7mers were used as analytes for kinetics measurements. dIBS1 and dIBS1wt were acquired and treated as described for NMR experiments. IBS1 and IBS1wt were purchased double-HPLC purified from IBA GmbH. Each kinetics run was preceded by five startup cycles injecting the current running buffer. The system was normalized using BIA normalizing solution (GE Healthcare). The flow rate was 30 µL/min. In each cycle, the adsorption and desorption was allowed to proceed for 60 s, each followed by 180 s of stabilization. At the end of each cycle, water was injected for 60 s to remove any residual analyte and Mg^{2+} bound to the surface. For all experiments, buffer injections were used for blank subtraction and one or more non-zero concentrations of the analyte were injected twice before and after the highest concentration to ensure that the performance of the surface did not significantly change within one experiment. All analyte samples were injected both into a flow cell where d3’EBS1(wt) was immobilized and in a ligand-free reference flow cell for control and background subtraction. Measurements were repeated on a different sensor chip for confirmation. In order to compare the affinity of dIBS1 and IBS1 to d3'EBS1, kinetics experiments were recorded at 25 °C. Mg^{2+} titrations of dIBS1 and IBS1 binding to d3'EBS1, and dIBS1wt and IBS1wt binding to d3'EBS1wt were performed at 15 or 25 °C by adding 0, 1, 2, 5 or 20 mM $MgCl_2$ or 1 mM $[Co(NH_3)_6]Cl_3$ to the running buffer and to the analyte stock. For each concentration of $MgCl_2$ a separate experiment was run. In all experiments, 5-7 non-zero concentrations of the analyte were injected being in the range of 0.25-16 µM for dIBS1, 0.5-45 µM for dIBS1wt, 0.0156-8 µM for IBS1 and 0.19-45 µM for IBS1wt. In order to obtain k_{on}, k_{off} and K_{D} ata were fitted and analyzed with the corresponding Biacore T100 evaluation software assuming a 1:1 binding model." [25]

6.7 Cotranscriptional self-cleavage assays of the CPEB3 ribozyme

In vitro transcription reactions with an elongated DNA template (Appendix 7.5) were performed as described in Section 6.2 in aliquots of 40 µL. For human CPEB3, one aliquot was removed after 1, 2, 3, 4, 5 and 7 h each and immediately frozen in liquid nitrogen to stop both transcription and cleavage. Samples were centrifuged briefly and a mixture of 82 % formamide and 10 mM EDTA was added to the supernatant (1:1). The transcription/cleavage products were subsequently separated on a 12 % denaturing PAGE gel.

6.8 Tb^{3+}-induced cleavage studies of the CPEB3 ribozyme

6.8.1 Dephosphorylation

To allow 5'-radiolabeling of the RNA, the 5'-triphosphates of RNA produced by *in vitro* transcription reactions first had to be removed. CPEB3 RNA (produced as described in Section 6.2) was therefore dephosphorylated using thermosensitive shrimp alkaline phosphatase (TSAP). For this, 5 µL TSAP (1U/µL) were added to aliquots of 60 pmol CPEB3 in 50 µL and the mixture was incubated at 37 °C for 30 min at 300 rpm. 3 additional µL of TSAP were added after 15 min of incubation. To remove the TSAP from the dephosphorylated RNA, two rounds of standard phenol-chloroform extraction and subsequent ethanol precipitation were performed. The RNA pellet was then redissolved in ME-buffer.

6.8.2 Radiolabeling

480 pmol of dephosphorylated CPEB3 in 31 µL ME-buffer were mixed with 4.5 µL T4 polynucleotide kinase and 4.5 µL of the appropriate commercial kinase buffer and 5 µL of ↑-γ-ATP (6000 Ci/mmol, 150 mCi/mL) to a total volume of 45 µL. The phosphorylation reaction was left to proceed for 30 min at 37 °C and 300 rpm and then quenched by adding 45 µL of formamide loading buffer. Unreacted ↑-γ-ATP and RNA degradation products were separated from the radiolabeled CPEB3 by 8 % PAGE. The CPEB3 RNA band was visualized by phosphorimaging, excised, crushed and mixed with crush & soak buffer by vortexing vigorously. The RNA was eluted into the buffer by slight shaking for 90 min at 4

°C and repeated vortexing. The supernatant was precipitated with ethanol to recover the RNA. The amount of radiolabeled CPEB was determined by scintillation counting.

6.8.3 Tb^{3+}-induced cleavage reactions

For Tb^{3+}-induced cleavage reactions, 2.4 - 2.5 nM of the radiolabeled CPEB3 RNA were first refolded in a mixture of 25 mM MOPS (pH 7), 100 mM KCl. 1 µM of cold CPEB3 RNA was added to later reduce the extent of nonspecific RNA degradation by Tb^{3+} and to facilitate precipitation of the RNA [340]. The RNA was annealed by heating to 90 °C for 90 s and by adding 5 or 20 mM $MgCl_2$ immediately after transferring to ice. Refolding was left to proceed for at least 15 min on ice.

Tb^{3+}-induced cleavage was carried out in 22.5 fmol aliquots of the refolded, radiolabeled CPEB3 RNA. A different amount of $TbCl_3$, kept in 5 mM sodium cacodylate (pH 5.5), was added to each aliquot and the reaction mixtures were incubated either for 30 min at RT or for 2-4 h at 4 °C. The cleavage reactions were quenched by adding a mixture of 82 % formamide and 10 mM EDTA to each aliquot at a 1:1 ratio and by subsequent ethanol precipitation of the cleavage fragments. The CPEB3 RNA fragments were separated by PAGE in 7 M urea, TBE and 16 % acrylamide/bisacrylamide (LongRanger) and visualized on a phosphorimager.

On each gel, an alkaline hydrolysis ladder (OH^-) and a T1-ribonuclease cleavage ladder of the CPEB3 RNA were loaded[2]. The OH^- ladder was prepared by incubating the same amount of radiolabeled CPEB3 RNA as used in the Tb^{3+}-induced cleavage reactions in 50 mM sodium carbonate buffer (pH 9) and 1 mM EDTA for 4-5 min at 90 °C and by quenching with formamide loading buffer (1:1). In a similar way, the T1 ladder was generated by incubation of the same amount of CPEB3 RNA with 0.1 U/µL T1 in 25 mM sodium citrate buffer (pH 5), 55-60 % formamide, ca. 7 mM EDTA at 55 °C for 4-5 min. The digestion was quenched by adding a 7:3 mixture of water/formamide loading buffer at a 1:1 ratio.

6.9 Determination of the equivalents of Mg^{2+} binding to the CPEB3 ribozyme

All samples contained 20 mM MOPS (pH 7) and either 50, 100 or 2000 mM KCl. 24 µM of the chimp CPEB3 ribozyme (produced as described in Section 6.2) were used for each experiment.

6.9.1 By HQS fluorescence

Determinations of the equivalents of Mg^{2+} bound to the CPEB3 ribozyme were performed as previously described [341, 342]. Two samples containing 0.1 µM of HQS[3], one of which contained the CPEB3 RNA, were titrated with Mg^{2+} in exactly the same way by adding 2-260 µM $MgCl_2$ in 29-42 steps. In each step, the sample was mixed thoroughly and the

---

[2] Alkaline hydrolysis occurs at each nucleotide; T1 cleaves 3' of each G in an RNA strand.

[3] The dye HQS served as a Mg^{2+} chelator and a fluorescent reporter at the same time. Mg^{2+} binds to HQS at a 1:1 ratio, strongly enhancing emission at 550 nm [342]

intensity of HQS fluorescence at 550 nm was recorded (the excitation wavelength was set to 400 nm).
By plotting $I_{CPEB3([Mg^{2+}])} - I_{blank([Mg^{2+}])}$ against $\frac{[Mg^{2+}]}{[CPEB3]}$, a curve is obtained, which reaches a plateau when the equivalents of Mg^{2+} binding to the RNA have been added.

6.9.2 By AAS

In the case of equilibrium dialysis, 100 µL of a CPEB3 sample containing 0.5 mM Mg^{2+} were dialyzed for 4-10 h against 5 mL of the buffer containing no Mg^{2+}. Dialysis was carried out in Tube-O-DIALYZER micro dialysis devices with an MWCO of 1000 Da (G-Biosciences, USA). After dialysis, the Mg^{2+}-content in the dialysate was measured by AAS and the equivalents of Mg^{2+} bound to one CPEB3 molecule are obtained according to

$$\frac{[Mg^{2+}]}{[CPEB3]} = \frac{[Mg^{2+}_{CPEB3}] - [Mg^{2+}_{dialysate}]}{[CPEB3]} \tag{6.3}$$

[309, 343], where $[Mg^{2+}_{CPEB3}]$ is the difference between the total Mg^{2+} concentration (0.5 mM) and $[Mg^{2+}_{dialysate}]$.

7 Appendices

7.1 NOESY spectrum of d3’EBS1·dIBS1

Sequential-walk region of a [^{1}H,^{1}H]-NOESY spectrum of the nonexchangeable protons of d3’EBS1·dIBS1. The H1’-H6/8 sequential walk of the d3’EBS1 residues is traced by dashed lines (4 terminal base pairs), solid lines (native d3’ hairpin sequence) and purple lines (EBS1 sequence). The spectrum was acquired at 25 °C (110 mM KCl, 10 μM EDTA, pD 6.8) in D_2O.

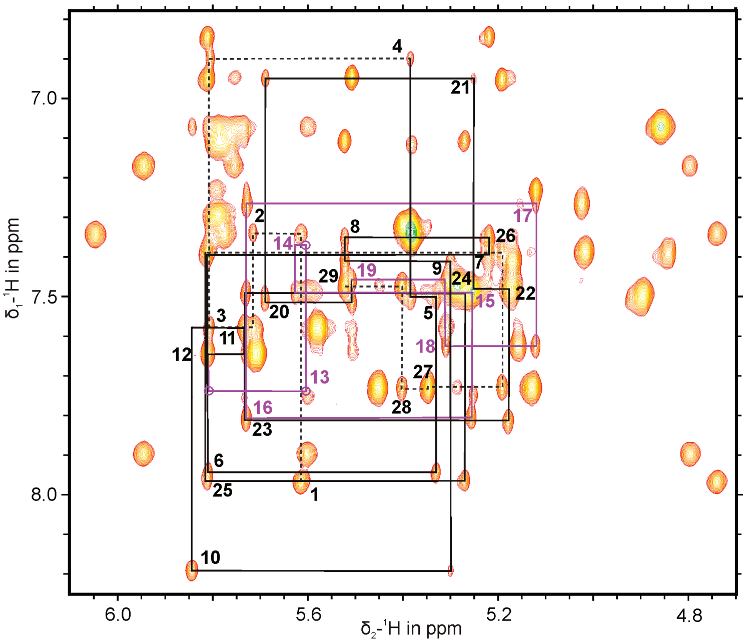

7.2 Kinetics of (d)IBS1 binding to d3'EBS1 in the presence of $[Co(NH_3)_6]^{3+}$

Influence of $[Co(NH_3)_6]^{3+}$ addition on the kinetics of dIBS1 binding to d3'EBS1 as determined by SPR experiments.

T	c($[Co(NH_3)_6]^{3+}$)	k_{on} in $\mu M^{-1}s^{-1}$	k_{off} in $\mu M^{-1}s^{-1}$	K_D in μM
15 °C	1 mM	0.1	0.008	0.053
	5 mM	0.11	0.004	0.041
25 °C	1 mM	0.42	0.05	0.12
	5 mM	0.69	0.03	0.05

7.3 NOESY spectrum of CPEB3

H1'-H6/8 sequential-walk region of a [^{1}H,^{1}H]-NOESY spectrum of the nonexchangeable protons of the chimp CPEB3 ribozyme showing the high degree of peak overlap. The spectrum was acquired at 25 °C (50 mM KCl, 10 μM EDTA, pD 6.8) in D_2O.

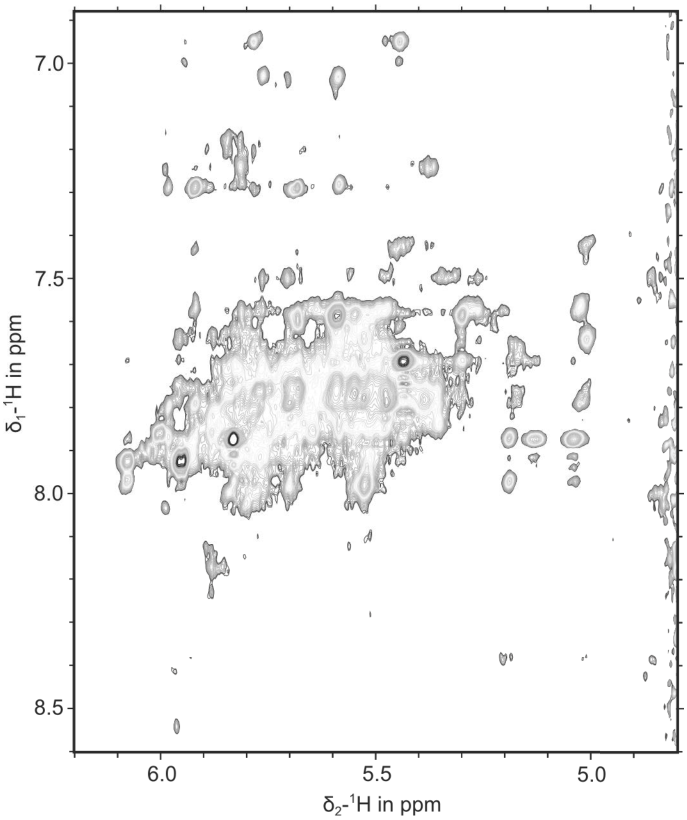

7.4 Native gels of CPEB3

12 % nondenaturing PAGE gels were prepared and run in the absence (a) and presence of 5 mM Mg^{2+} (b). Both conditions reveal only one major 3D structure of CPEB3. Lanes are labeled with the loaded substance amount of CPEB3 in nmol and "D" for the loading buffer. On the left, the positions of the two dyes are indicated with "XC" and "BB" for xylene cyanol and bromophenol blue, respectively.

Possible structural heterogeneity in the human ribozyme was investigated using native PAGE (Appendix 7.4). Irrespective of the presence of Mg^{2+}, there is only one main band in the gels, even when very high substance amounts are loaded. There are very faint bands higher in the gel, which are slightly more intense in the presence of 5 mM Mg^{2+}. These bands could correspond to mis- or partly unfolded sequences or multimers. The different location of the main band relative to the two dyes is due to a different migration behavior caused by the presence of Mg^{2+} and does not reflect a more extended conformation (Section 5.6.6).

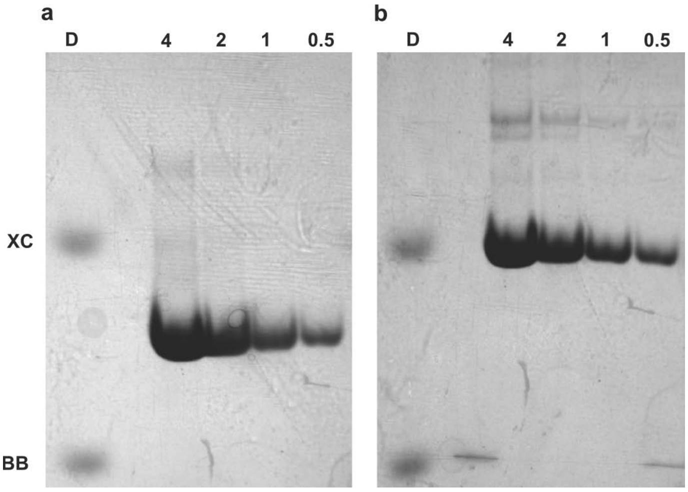

7.5 CPEB3 wild type and mutant sequences tested for NMR spectroscopy

(a) chimp sequence (b) chimp sequence with modified P1.1 domain and shortened and modified P4 domain (c) chimp with modified P1 domain. Mutated residues are shown in boldface. (d) elongated chimp sequence used for cleavage studies. The 18 nt extension corresponds to the upstream sequence in the human and chimp *cpeb3* gene. The triangle marks the cleavage site.

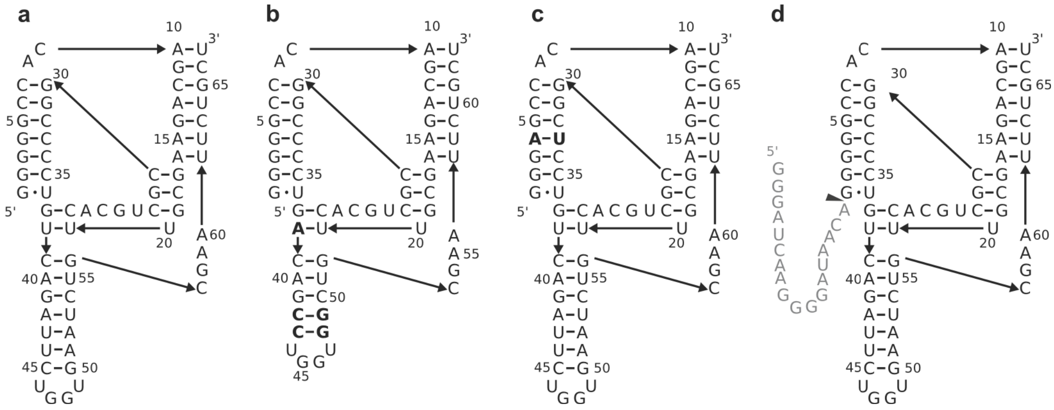

7.6 Chemical shifts of the P1 protons

Nonexchangeable proton resonances were recorded at 25 °C in D_2O and exchangeable proton resonances were recorded at 5 °C in H_2O (100 mM KCl, 10 µM EDTA, pD/pH 6.8). Chemical shifts are given in ppm.

P1	CPEB3	H1’	H2’	H6/8	H2/5	H1/3	H41	H42
G1	G1	5.906	4.949	8.174	-	10.841	-	-
G2	G2	5.887	4.715	7.578	-	12.816	-	-
G3	G3	5.871	4.648	7.291	-	12.688	-	-
G4	G4	5.818	4.659	7.22	-	12.736	-	-
G5	G5	5.797	4.548	7.255	-	13.291	-	-
C6	C6	5.55	4.452	7.656	5.247	-	8.751	7.004
C7	C7	5.487	4.484	7.748	5.569	-	8.535	0.001
A8	-	5.962	4.55	7.933	7.332	-	-	-
G9	-	5.457	4.329	7.162	-	10.535	-	-
A10	-	5.691	4.736	8.329	7.782	-	-	-
A11	-	5.435	4.394	7.91	7.682	-	-	-
A12	-	6.033	4.453	8.127	8.2	-	-	-
U13	-	3.673	4.412	7.886	5.925	-	-	-
G14	G30	5.851	4.571	7.765	-	12.153	-	-
G15	G31	5.69	4.436	7.343	-	13.349	-	-
C16	C32	5.523	4.445	7.646	5.228	-	8.719	7.033
C17	C33	5.497	4.401	7.845	5.526	-	8.664	7.007
C18	C34	5.529	4.433	7.751	5.471	-	8.554	7.016
C19	C35	5.524	4.435	7.786	5.669	-	8.456	6.98
U20	U36	5.761	4.037	7.79	5.541	11.906	-	-

7.7 Chemical shifts of the P2 protons

Nonexchangeable proton resonances were recorded at 25 °C in D_2O and exchangeable proton resonances were recorded at 5 °C in H_2O (20 mM KCl, 10 µM EDTA, pD/pH 6.8). Chemical shifts are given in ppm.

P2	CPEB3	H1’	H2’	H6/8	H2/5	H1/3	H41	H42
G1	-	5.741	4.922	8.115	-	12.632	-	-
A2	A10	6.092	4.796	8.122	7.614	13.435	-	-
G3	G11	5.651	4.435	7.245	-	-	-	-
C4	C12	5.461	4.528	7.506	5.2	-	8.343	6.892
A5	A13	5.945	4.708	7.935	6.944	-	-	-
G6	G14	5.547	4.528	7.104	-	-	-	-
A7	A15	5.868	4.561	7.639	7.076	-	-	-
A8	A16	5.922	4.438	7.721	7.751	-	-	-
C9	-	5.358	4.322	7.134	5.024	-	8.176	6.908
G10	-	5.651	4.475	7.57	-	10.545	-	-
A11	-	5.717	4.75	8.382	7.86	-	-	-
A12	-	5.474	4.348	7.941	7.827	-	-	-
A13	-	6.051	4.631	8.206	8.054	-	-	-
G14	-	3.874	4.285	7.849	-	12.964	-	-
U15	U61	5.57	4.522	7.744	5.092	14.433	-	-
U16	U62	5.633	4.518	7.969	5.585	13.929	-	-
C17	C63	5.472	4.313	7.814	5.665	-	8.344	7.043
U18	U64	5.462	4.599	7.807	5.377	13.354	-	-
G19	G65	5.757	4.532	7.742	-	12.467	-	-
C20	C66	5.458	4.315	7.681	5.2	-	8.497	6.986
U21	U67	5.577	4.294	7.909	5.405	14.162	-	-
C22	-	5.87	3.993	7.77	5.722	-	8.272	7.187

7.8 NOESY spectra of the P1 and P2 exchangeable protons

Imino-proton regions of the [^{1}H,^{1}H]-NOESY spectra of the (a) P1 and (b) P2 model constructs. The spectra were recorded at 5 °C in H_2O (100 mM KCl (P1)/ 20 mM KCl (P2), 10 µM EDTA, pH 6.8).

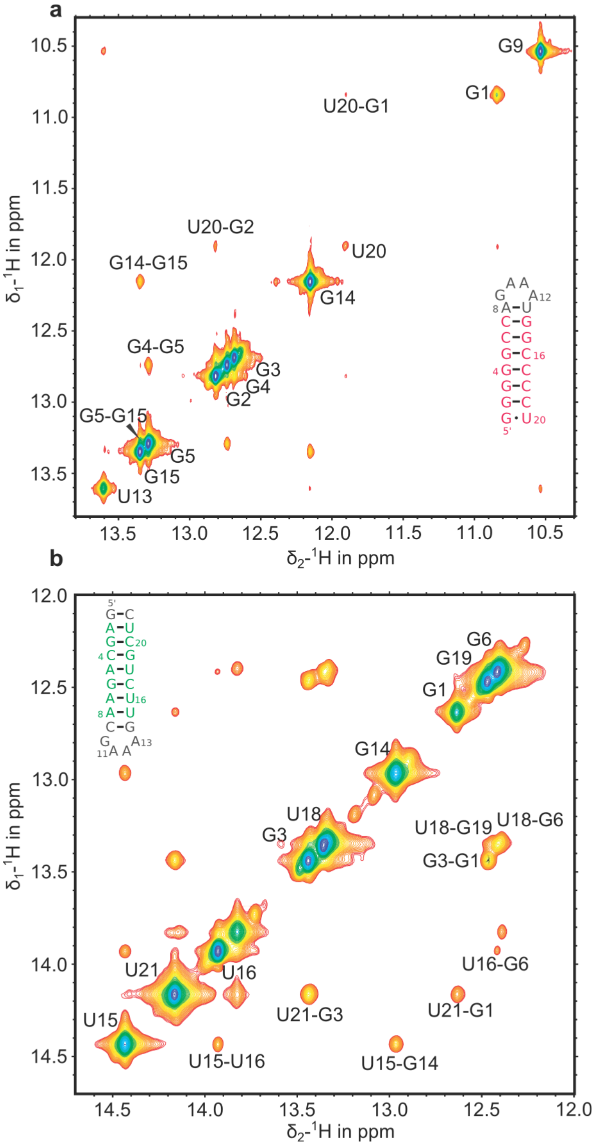

7.9 Chemical shifts of the CPEB3 protons and nitrogens

Nonexchangeable proton resonances were recorded at 25 °C in D_2O and nitrogen and exchangeable proton resonances were recorded at 5 °C in H_2O (100 mM KCl, 10 µM EDTA, pD/pH 6.8). Chemical shifts are given in ppm.

	0 mM Mg^{2+}						5 mM Mg^{2+}	
	H1'	H2'	H6/8	H2	H1/3	N1/3	H1/3	N1/3
G1	5.641	4.831	8.372	-	10.601	142.813	10.517	-
G2	5.892	4.221	7.512	-	12.598	148.488	12.604	148.537
G3	5.8	4.604	7.217	-	12.572	148.131	12.622	148.569
G4	5.838	4.487	7.161	-	12.695	148.658	12.7	148.663
G5	5.761	4.621	7.199	-	13.274	149.614	13.285	149.632
C6	5.493	-	7.627	-	-	197.464	-	197.503
C7	5.562	-	7.71	-	-	195.762	-	195.74
A8-U9	-	-	-	-	-	-	-	-
A10	5.905	-	-	7.742	-	-	-	
G11	5.575	4.517	7.73	-	13.551	149.018	13.56	149.201
C12	5.392	3.996	7.448	-	-	196.914	-	197.648
A13	5.924	4.687	7.889	6.928	-	220.368	-	220.213
G14	5.429	4.468	6.992	-	12.428	148.142	12.47	148.124
A15	5.816	4.606	7.61	7.271	-	220.413	-	220.568
A16	5.883	4.682	7.828	7.269	-	-	-	-
G17	5.46	4.666	6.896	-	-	-	-	-
C18	5.492	-	7.736	-	-	-	-	-
G19	5.807	-	7.958	-	-	-	-	-
U20-U26	-	-	-	-	-	-	-	-
C27	5.505	-	7.726	-	-	-	-	-
G28	5.979	-	8.003	-	-	-	-	-
C29	5.86	-	7.414	-	-	-	-	-
G30	5.433	-	7.599	-	12.059	147.729	12.092	147.834
G31	-	-	-	-	13.226	149.39	13.223	149.372
C32	-	-	-	-	-	197.851	-	197.851
C33	-	-	-	-	-	197.729	-	197.213
C34	-	-	-	-	-	195.66	-	195.461
C35	-	-	-	-	-	197.464	-	197.296
U36	-	-	-	-	11.655	-	11.721	-
G37	-	-	-	-	-	-	-	-
U38	5.885	4.429	-	-	-	-	-	-
C39	5.503	4.473	7.897	-	-	197.719	197.661	
A40	5.951	4.675	8.083	6.977	-	219.692	-	219.692
G41	5.566	-	7.144	-	12.538	147.392	12.561	147.195

	0 mM Mg^{2+}						5 mM Mg^{2+}	
	H1’	H2’	H6/8	H2	H1/3	N1/3	H1/3	N1/3
A42	5.938	-	7.73	7.754	-	222.059	-	222.048
U43	5.505	-	7.634	-	14.15	162.997	14.14	163.326
U44	5.678	-	7.968	-	13.743	163.106	13.767	163.342
C45	5.66	4.47	7.74	-	-	196.363	-	196.415
U46	5.275	4.333	7.568	-	-	158.384	11.04	158.499
G47	5.413	-	7.673	-	10.876	147.758	10.832	147.796
G48	5.808	5.007	7.849	-	10.103	146.277	10.029	146.215
U49	6.06	4.566	7.908	-	-	-	-	
G50	5.154	4.682	7.955	-	12.122	147.706	12.133	147.688
A51	5.96	4.664	7.857	7.263	-	220.683	-	220.838
A52	5.905	4.423	7.799	7.764	-	222.397	-	222.474
U53	5.455	4.386	7.565	-	14.158	162.849	14.162	162.948
C54	5.571	4.325	7.765	-	-	197.321	-	197.321
U55	5.454	4.505	7.839	-	13.664	163.078	13.666	163.053
G56	5.735	4.173	7.69	-	12.339	147.19	12.459	147.141
C57	5.747	4.136	7.451	-	-	-	-	-
G58	5.762	4.623	7.984	-	-	-	-	-
A59	5.874	3.652	8.097	7.167	-	-	-	-
A60	6.148	4.964	8.351	-	-	-	-	-
U61	5.692	3.772	7.485	-	14.748	163.713	14.79	163.998
U62	5.804	-	7.967	-	13.559	162.838	13.562	162.838
C63	5.479	-	7.801	-	-	196.577	-	196.688
U64	5.457	4.574	7.783	-	-	162.747	13.317	162.769
G65	5.764	4.454	7.765	-	12.415	148.131	12.441	148.113
C66	5.501	4.22	7.656	-	-	197.974	-	197.961
U67	5.787	4.021	7.768	-	14.664	163.749	14.666	163.956
Ga	-	-	-	-	13.414	149.002	13.407	149.367
Gb	-	-	-	-	13.165	149.32	13.199	149.368
Gc	-	-	-	-	-	-	13.023	148.478
Gd	-	-	-	-	12.73	148.082	12.747	147.837
Ge	-	-	-	-	-	-	12.721	147.341
Gf	-	-	-	-	-	-	10.935	145.617
Gg	-	-	-	-	-	-	10.275	142.499
Ua	-	-	-	–	-	-	13.61	162.138
Ub	-	-	-	-	-	-	12.497	158.036
Uc	-	-	-	-	-	-	12.15	158.615
Ud	-	-	-	-	-	-	11.44	158.218
Ue	-	-	-	-	-	-	11.306	158.212
X	-	-	-	-	-	-	12.561	
Y	-	-	-	-	12.451	-	12.471	

7.10 J_{NN} HNN-COSY of CPEB3

J_{NN} HNN-COSY spectrum of the N1-H1· · ·N3 correlations of all G-C base pairs in the CPEB3 ribozyme (a) in the absence of Mg^{2+} and (b) in the presence of 5 mM Mg^{2+}. Peaks appearing upon addition of Mg^{2+} are labeled in boldface. The spectrum was recorded at 5 °C in H_2O (100 mM KCl, 10 µM EDTA, pH 6.8).

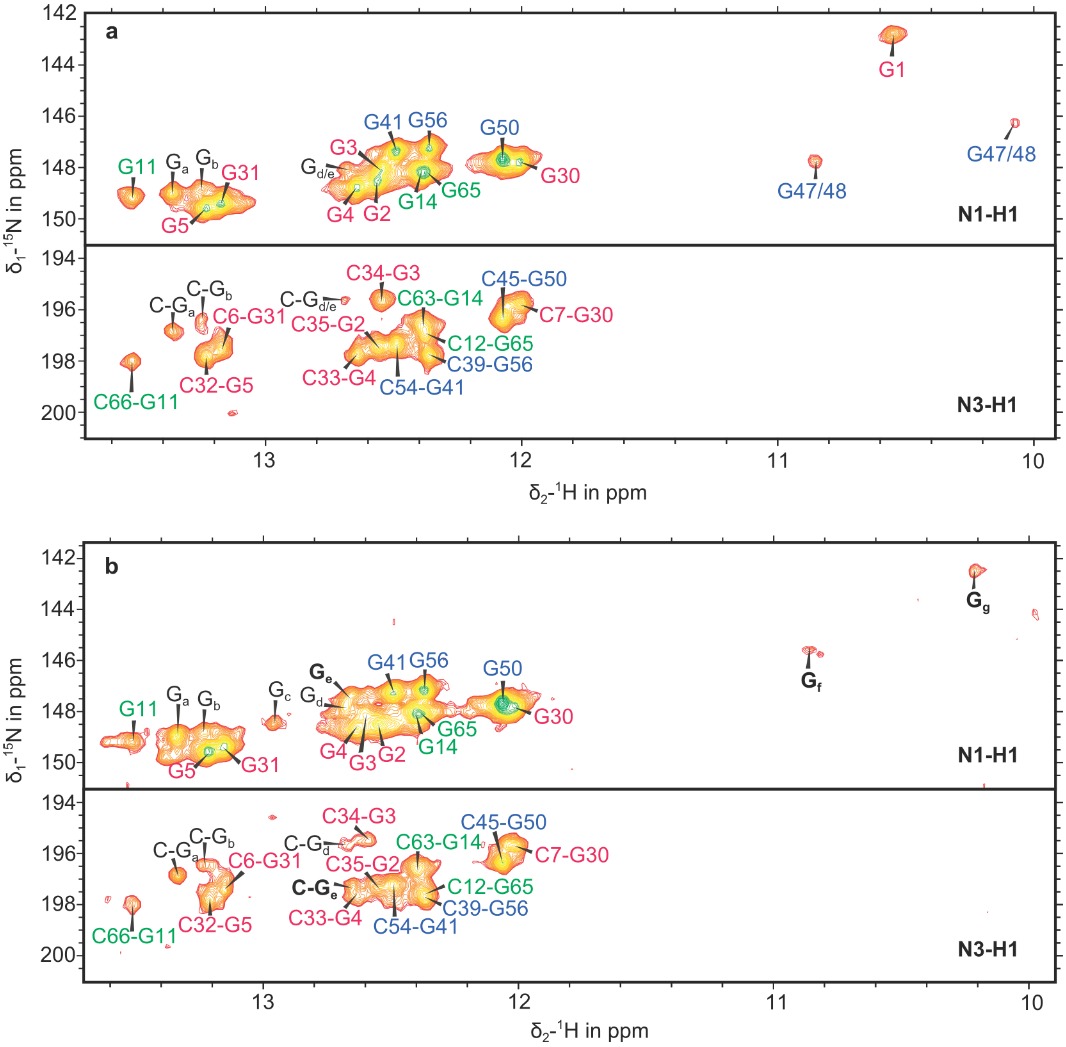

7.11 Mg^{2+} binding to the P1 and P2 model constructs

Mg^{2+}-induced chemical shift changes $\Delta\delta$ of (a) P1 proton resonances and (b) P2 proton resonances. G14H1’ shifts by -0.191 ppm from 0-3 mM and further -0.083 ppm from 3-5 mM. The correponding histogramm bar is truncated for display reasons. δ values were obtained from spectra recorded at 25 °C in D_2O (100 mM KCl (P1), 20 mM KCl (P2), 10 µM EDTA, pD 6.8).

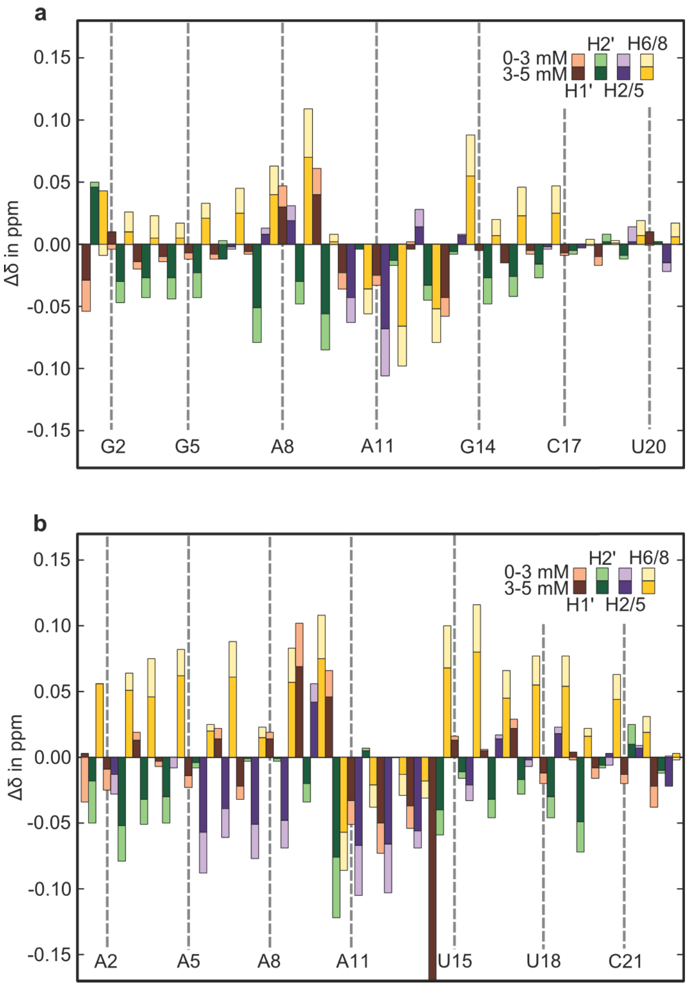

7.12 NOE correlations between P1 imino protons and $[Co(NH_3)_6]^{3+}$ protons

The spectrum was recorded at 5 °C in H_2O (100 mM KCl, 10 µM EDTA, 1 mM $[Co(NH_3)_6]Cl_3$, pH 6.8).

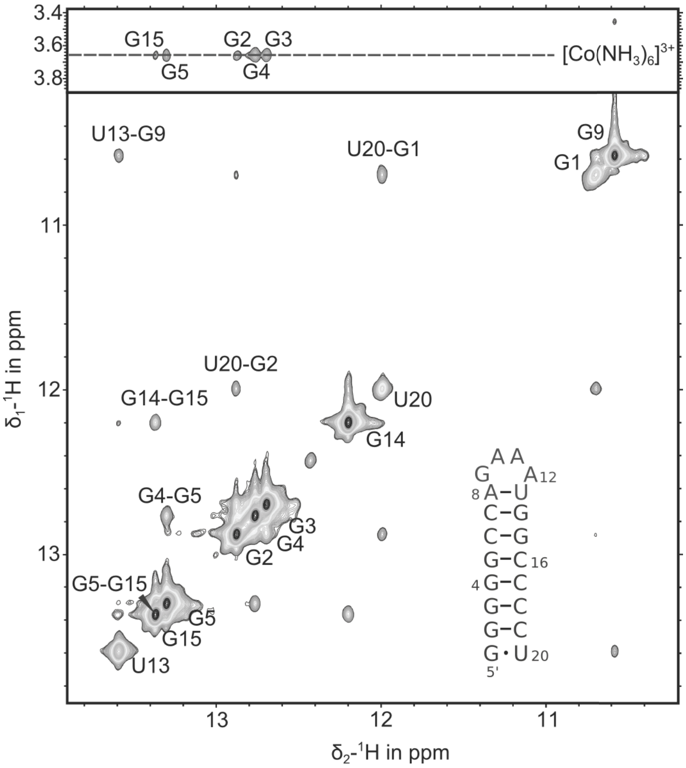

7.13 Mg^{2+}-induced chemical shift changes of the P2 imino protons

1D-^{1}H spectra of the exchangeable protons of the P2 model construct in the presence of different Mg^{2+} concentrations. All spectra were recorded at 5 °C in H_2O (50 mM KCl, 10 μM EDTA, pH 6.8).

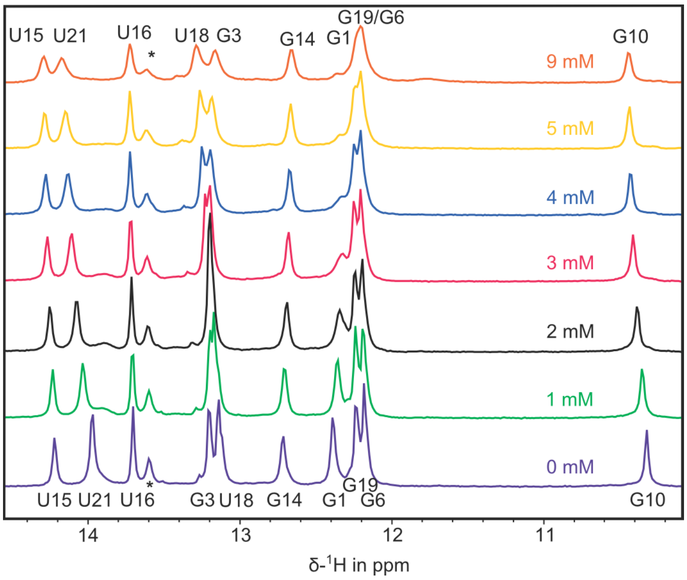

7.14 Hydrodynamic radius of the chimp CPEB3 ribozyme

The hydrodynamic radius r_H was determined in different concentrations of K^+ and Mg^{2+} by DOSY measurements. All values are averages of two integrated regions with one standard deviation.

c(K^+) in mM	c(Mg^{2+}) in mM	$r_H \pm 1\sigma$ in nm
10	0	3.03±0.01
100	0	2.49±0.07
100	2	2.40±0.03
100	5	2.40±0.04
100	10	2.36±0.03
100	20	2.36±0.03

List of Figures

List of Tables

Bibliography

[1] F. H. Crick, “On protein synthesis,” *Symposia of the Society for Experimental Biology*, vol. 12, pp. 138–163, 1958.

[2] M. B. Hoagland, M. L. Stephenson, J. F. Scott, L. I. Hecht, and P. C. Zamecnik, “A soluble ribonucleic acid intermediate in protein synthesis,” *Journal of Biological Chemistry*, vol. 231, no. 1, pp. 241–257, 1958.

[3] C. R. Woese, *The genetic code: the molecular basis for genetic expression.* New York: Harper & Row, 1967.

[4] F. H. C. Crick, “The origin of the genetic code,” *Journal of Molecular Biology*, vol. 38, no. 3, pp. 367–379, 1968.

[5] L. E. Orgel, “Evolution of the genetic apparatus,” *Journal of Molecular Biology*, vol. 38, no. 3, pp. 381–393, 1968.

[6] B. C. Stark, R. Kole, E. J. Bowman, and S. Altman, “Ribonuclease P: an enzyme with an essential RNA component,” *Proceedings of the National Academy of Sciences of the United States of America*, vol. 75, no. 8, pp. 3717–3721, 1978.

[7] C. Guerrier-Takada, K. Gardiner, T. Marsh, N. Pace, and S. Altman, “The RNA moiety of ribonuclease P is the catalytic subunit of the enzyme,” *Cell*, vol. 35, no. 3, pp. 849–857, 1983.

[8] T. R. Cech, A. J. Zaug, and P. J. Grabowski, “In vitro splicing of the ribosomal RNA precursor of *Tetrahymena*: Involvement of a guanosine nucleotide in the excision of the intervening sequence,” *Cell*, vol. 27, no. 3, pp. 487–496, 1981.

[9] A. J. Zaug and T. R. Cech, “The intervening sequence excised from the ribosomal RNA precursor of *Tetrahymena* contains a 5-terminal guanosine residue not encoded by the DNA,” *Nucleic Acids Research*, vol. 10, no. 9, pp. 2823–2838, 1982.

[10] A. S. Mironov, I. Gusarov, R. Rafikov, L. E. Lopez, K. Shatalin, R. A. Kreneva, D. A. Perumov, and E. Nudler, “Sensing small molecules by nascent RNA: a mechanism to control transcription in bacteria,” *Cell*, vol. 111, no. 5, pp. 747–756, 2002.

[11] A. Nahvi, N. Sudarsan, M. S. Ebert, X. Zou, K. L. Brown, and R. R. Breaker, “Genetic control by a metabolite binding mRNA,” *Chemistry & Biology*, vol. 9, no. 9, pp. 1043–1049, 2002.

[12] W. Winkler, A. Nahvi, and R. R. Breaker, “Thiamine derivatives bind messenger RNAs directly to regulate bacterial gene expression,” *Nature*, vol. 419, no. 6910, pp. 952–956, 2002.

[13] W. Nellen and C. Lichtenstein, “What makes an mRNA anti-sense-itive?,” *Trends in Biochemical Sciences*, vol. 18, no. 11, pp. 419–423, 1993.

[14] A. Fire, S. Xu, M. K. Montgomery, S. A. Kostas, S. E. Driver, and C. C. Mello, “Potent and specific genetic interference by double-stranded RNA in *Caenorhabditis elegans*,” *Nature*, vol. 391, no. 6669, pp. 806–811, 1998.

[15] W. Gilbert, “Origin of life: The RNA world,” *Nature*, vol. 319, no. 6055, pp. 618–618, 1986.

[16] M. P. Robertson and G. F. Joyce, “The origins of the RNA world,” *Cold Spring Harbor Perspectives in Biology*, vol. 4, no. 5, p. a003608, 2012.

[17] G. Joyce, “Forty years of in vitro evolution,” *Angewandte Chemie International Edition*, vol. 46, no. 34, pp. 6420–6436, 2007.

[18] R. R. Breaker and G. F. Joyce, “A DNA enzyme that cleaves RNA,” *Chemistry & Biology*, vol. 1, no. 4, pp. 223–229, 1994.

[19] J. C. Burnett and J. J. Rossi, “RNA-Based therapeutics: Current progress and future prospects,” *Chemistry & Biology*, vol. 19, no. 1, pp. 60–71, 2012.

[20] J. C. Chaput, H. Yu, and S. Zhang, “The emerging world of synthetic genetics,” *Chemistry & Biology*, vol. 19, no. 11, pp. 1360–1371, 2012.

[21] N. K. Navani and Y. Li, “Nucleic acid aptamers and enzymes as sensors,” *Current Opinion in Chemical Biology*, vol. 10, no. 3, pp. 272–281, 2006.

[22] H. Kobayashi, S. G. Eckhardt, J. A. Lockridge, M. L. Rothenberg, A. B. Sandler, C. L. O’Bryant, W. Cooper, S. N. Holden, R. D. Aitchison, N. Usman, M. Wolin, and M. L. Basche, “Safety and pharmacokinetic study of RPI.4610 (ANGIOZYME), an anti-VEGFR-1 ribozyme, in combination with carboplatin and paclitaxel in patients with advanced solid tumors,” *Cancer Chemotherapy and Pharmacology*, vol. 56, no. 4, pp. 329–336, 2005.

[23] D. Kruschel, M. Skilandat, and R. K. O. Sigel, “NMR structure of the 5’ splice site in the group IIB intron *Sc*.ai5γ – conformational requirements for exon–intron recognition,” *RNA*, vol. 20, no. 3, pp. 295–307, 2014.

[24] M. Skilandat and R. K. O. Sigel, “Ribozymes,” in *Brenner’s Encyclopedia of Genetics (Second Edition)* (S. Maloy and K. Hughes, eds.), pp. 254–258, Academic Press, 2013.

[25] M. Skilandat and R. K. O. Sigel, “The role of Mg(II) in DNA cleavage site recognition in group II intron ribozymes – solution structure and metal ion binding sites of the

RNA·DNA complex," *Journal of Biological Chemistry*, vol. 289, no. 30, pp. 20650–20663, 2014.

[26] M. Skilandat, M. Rowińska-Żyrek, and R. K. O. Sigel, "Solution structure and metal ion binding sites of the human CPEB3 ribozyme's p4 domain," *Journal of Biological Inorganic Chemistry*, vol. 19, no. 6, pp. 903–912, 2014.

[27] P. Yakovchuk, E. Protozanova, and M. D. Frank-Kamenetskii, "Base-stacking and base-pairing contributions into thermal stability of the DNA double helix," *Nucleic Acids Research*, vol. 34, no. 2, pp. 564–574, 2006.

[28] R. E. Dickerson, H. R. Drew, B. N. Conner, R. M. Wing, A. V. Fratini, and M. L. Kopka, "The anatomy of A-, B-, and Z-DNA," *Science*, vol. 216, no. 4545, pp. 475–485, 1982.

[29] Y. Mitsui, R. Langridge, B. E. Shortle, C. R. Cantor, R. C. Grant, M. Kodama, and R. D. Wells, "Physical and enzymatic studies on poly d(I-C)-poly d(I-C), an unusual double-helical DNA," *Nature*, vol. 228, no. 5277, pp. 1166–1169, 1970.

[30] A. H. Wang, G. J. Quigley, F. J. Kolpak, J. L. Crawford, J. H. van Boom, G. van der Marel, and A. Rich, "Molecular structure of a left-handed double helical DNA fragment at atomic resolution," *Nature*, vol. 282, no. 5740, pp. 680–686, 1979.

[31] Y.-M. Hou, "Base pairing in RNA: unusual patterns," in *eLS*, John Wiley & Sons, Ltd, 2001.

[32] E. N. Nikolova, H. Zhou, F. L. Gottardo, H. S. Alvey, I. J. Kimsey, and H. M. Al-Hashimi, "A historical account of Hoogsteen base-pairs in duplex DNA," *Biopolymers*, vol. 99, no. 12, pp. 955–968, 2013.

[33] K. Y. Chang and I. Tinoco Jr, "Characterization of a "kissing" hairpin complex derived from the human immunodeficiency virus genome," *Proceedings of the National Academy of Sciences*, vol. 91, no. 18, pp. 8705–8709, 1994.

[34] E. Skripkin, J. C. Paillart, R. Marquet, B. Ehresmann, and C. Ehresmann, "Identification of the primary site of the human immunodeficiency virus type 1 RNA dimerization in vitro," *Proceedings of the National Academy of Sciences*, vol. 91, no. 11, pp. 4945–4949, 1994.

[35] P. L. Adams, M. R. Stahley, A. B. Kosek, J. Wang, and S. A. Strobel, "Crystal structure of a self-splicing group I intron with both exons," *Nature*, vol. 430, no. 6995, pp. 45–50, 2004.

[36] N. Toor, K. S. Keating, S. D. Taylor, and A. M. Pyle, "Crystal structure of a self-spliced group II intron," *Science*, vol. 320, no. 5872, pp. 77–82, 2008.

[37] G. J. Quigley and A. Rich, "Structural domains of transfer RNA molecules," *Science*, vol. 194, no. 4267, pp. 796–806, 1976.

[38] A. R. Ferré-D'Amaré, K. Zhou, and J. A. Doudna, "Crystal structure of a hepatitis delta virus ribozyme," *Nature*, vol. 395, no. 6702, pp. 567–574, 1998.

[39] H. W. Pley, K. M. Flaherty, and D. B. McKay, "Model for an RNA tertiary interaction from the structure of an intermolecular complex between a GAAA tetraloop and an RNA helix," *Nature*, vol. 372, no. 6501, pp. 111–113, 1994.

[40] M. Costa and F. Michel, "Frequent use of the same tertiary motif by self-folding RNAs," *The EMBO Journal*, vol. 14, no. 6, pp. 1276–1285, 1995.

[41] J. H. Cate, A. R. Gooding, E. Podell, K. Zhou, B. L. Golden, C. E. Kundrot, T. R. Cech, and J. A. Doudna, "Crystal structure of a group I ribozyme domain: principles of RNA packing," *Science*, vol. 273, no. 5282, pp. 1678–1685, 1996.

[42] J. H. Davis, M. Tonelli, L. G. Scott, L. Jaeger, J. R. Williamson, and S. E. Butcher, "RNA helical packing in solution: NMR structure of a 30 kDa GAAA Tetraloop–Receptor complex," *Journal of Molecular Biology*, vol. 351, no. 2, pp. 371–382, 2005.

[43] P. Nissen, J. A. Ippolito, N. Ban, P. B. Moore, and T. A. Steitz, "RNA tertiary interactions in the large ribosomal subunit: The A-minor motif," *Proceedings of the National Academy of Sciences*, vol. 98, no. 9, pp. 4899–4903, 2001.

[44] M. Tamura and S. R. Holbrook, "Sequence and structural conservation in RNA ribose zippers," *Journal of Molecular Biology*, vol. 320, no. 3, pp. 455–474, 2002.

[45] A. V. Kazantsev and N. R. Pace, "Bacterial RNase P: a new view of an ancient enzyme," *Nature Reviews Microbiology*, vol. 4, no. 10, pp. 729–740, 2006.

[46] S. H. Kim, J. L. Sussman, F. L. Suddath, G. J. Quigley, A. McPherson, A. H. J. Wang, N. C. Seeman, and A. Rich, "The general structure of transfer RNA molecules," *Proceedings of the National Academy of Sciences*, vol. 71, no. 12, pp. 4970–4974, 1974.

[47] P. Brion and E. Westhof, "Hierarchy and dynamics of RNA folding," *Annual Review of Biophysics and Biomolecular Structure*, vol. 26, no. 1, pp. 113–137, 1997.

[48] O. Fedorova, C. Waldsich, and A. M. Pyle, "Group II intron folding under near-physiological conditions: collapsing to the near-native state," *Journal of Molecular Biology*, vol. 366, no. 4, pp. 1099–1114, 2007.

[49] M. Steiner, K. S. Karunatilaka, R. K. O. Sigel, and D. Rueda, "Single-molecule studies of group II intron ribozymes," *Proceedings of the National Academy of Sciences*, vol. 105, no. 37, pp. 13853–13858, 2008.

[50] R. Schroeder, A. Barta, and K. Semrad, "Strategies for RNA folding and assembly," *Nature Reviews Molecular Cell Biology*, vol. 5, no. 11, pp. 908–919, 2004.

[51] A. Zhang, K. M. Wassarman, C. Rosenow, B. C. Tjaden, G. Storz, and S. Gottesman, "Global analysis of small RNA and mRNA targets of Hfq," *Molecular Microbiology*, vol. 50, no. 4, pp. 1111–1124, 2003.

[52] A. S. Petrov, J. C. Bowman, S. C. Harvey, and L. D. Williams, "Bidentate RNA–magnesium clamps: On the origin of the special role of magnesium in RNA folding," *RNA*, vol. 17, no. 2, pp. 291–297, 2011.

[53] D. Pörschke, "The mode of Mg^{++} binding to oligonucleotides. Inner sphere complexes as markers for recognition?," *Nucleic Acids Research*, vol. 6, no. 3, pp. 883–898, 1979.

[54] D. E. Draper, D. Grilley, and A. M. Soto, "Ions and RNA folding," *Annual Review of Biophysics and Biomolecular Structure*, vol. 34, no. 1, pp. 221–243, 2005.

[55] J. C. Bowman, T. K. Lenz, N. V. Hud, and L. D. Williams, "Cations in charge: magnesium ions in RNA folding and catalysis," *Current Opinion in Structural Biology*, vol. 22, no. 3, pp. 262–272, 2012.

[56] V. K. Misra and D. E. Draper, "Mg^{2+} binding to tRNA revisited: the nonlinear Poisson-Boltzmann model," *Journal of Molecular Biology*, vol. 299, no. 3, pp. 813–825, 2000.

[57] V. K. Misra and D. E. Draper, "A thermodynamic framework for Mg^{2+} binding to RNA," *Proceedings of the National Academy of Sciences*, vol. 98, no. 22, pp. 12456–12461, 2001.

[58] R. K. O. Sigel and A. M. Pyle, "Alternative roles for metal ions in enzyme catalysis and the implications for ribozyme chemistry," *Chemical Reviews*, vol. 107, no. 1, pp. 97–113, 2007.

[59] T.-S. Lee, G. M. Giambaşu, C. P. Sosa, M. Martick, W. G. Scott, and D. M. York, "Threshold occupancy and specific cation binding modes in the hammerhead ribozyme active site are required for active conformation," *Journal of Molecular Biology*, vol. 388, no. 1, pp. 195–206, 2009.

[60] A. A. Szewczak, E. R. Podell, P. C. Bevilacqua, and T. R. Cech, "Thermodynamic stability of the P4–P6 domain RNA tertiary structure measured by temperature gradient gel electrophoresis," *Biochemistry*, vol. 37, no. 32, pp. 11162–11170, 1998.

[61] S. A. Woodson, "Metal ions and RNA folding: a highly charged topic with a dynamic future," *Current Opinion in Chemical Biology*, vol. 9, no. 2, pp. 104–109, 2005.

[62] S. Moghaddam, G. Caliskan, S. Chauhan, C. Hyeon, R. M. Briber, D. Thirumalai, and S. A. Woodson, "Metal ion dependence of cooperative collapse transitions in RNA," *Journal of Molecular Biology*, vol. 393, no. 3, pp. 753–764, 2009.

[63] D. Leipply and D. E. Draper, "Effects of Mg^{2+} on the free energy landscape for folding a purine riboswitch RNA," *Biochemistry*, vol. 50, no. 14, pp. 2790–2799, 2011.

[64] A. Savinov, C. F. Perez, and S. M. Block, "Single-molecule studies of riboswitch folding," *Biochimica et Biophysica Acta (BBA) - Gene Regulatory Mechanisms*, 2014, in press, doi:10.1016/j.bbagrm.2014.04.005.

[65] G. J. Quigley, M. M. Teeter, and A. Rich, “Structural analysis of spermine and magnesium ion binding to yeast phenylalanine transfer RNA,” *Proceedings of the National Academy of Sciences of the United States of America*, vol. 75, no. 1, pp. 64–68, 1978.

[66] D. J. Klein, P. B. Moore, and T. A. Steitz, “The contribution of metal ions to the structural stability of the large ribosomal subunit,” *RNA*, vol. 10, no. 9, pp. 1366–1379, 2004.

[67] A. V. Kazantsev, A. A. Krivenko, and N. R. Pace, “Mapping metal-binding sites in the catalytic domain of bacterial RNase P RNA,” *RNA*, vol. 15, no. 2, pp. 266–276, 2009.

[68] J. H. Cate, R. L. Hanna, and J. A. Doudna, “A magnesium ion core at the heart of a ribozyme domain,” *Nature Structural Biology*, vol. 4, no. 7, pp. 553–558, 1997.

[69] J. A. Liberman, M. Salim, J. Krucinska, and J. E. Wedekind, “Structure of a class II preQ1 riboswitch reveals ligand recognition by a new fold,” *Nature Chemical Biology*, vol. 9, no. 6, pp. 353–355, 2013.

[70] C. Hsiao, E. Tannenbaum, H. VanDeusen, E. Hershkovitz, G. Perng, A. R. Tannenbaum, and L. D. Williams, “Complexes of nucleic acids with group I and II cations,” in *Nucleic Acid-Metal Ion Interactions*, pp. 1–38, The Royal Society of Chemistry, 2009.

[71] J. L. Fiore, E. D. Holmstrom, and D. J. Nesbitt, “Entropic origin of Mg^{2+}-facilitated RNA folding,” *Proceedings of the National Academy of Sciences*, vol. 109, no. 8, pp. 2902–2907, 2012.

[72] H. Diebler, M. Eigen, G. Ilgenfritz, G. Maass, and R. Winkler, “Kinetics and mechanism of reactions of main group metal ions with biological carriers,” *Pure and Applied Chemistry*, vol. 20, no. 1, 1969.

[73] G. D. Markham, J. P. Glusker, and C. W. Bock, “The arrangement of first- and second-sphere water molecules in divalent magnesium complexes: Results from molecular orbital and density functional theory and from structural crystallography,” *The Journal of Physical Chemistry B*, vol. 106, no. 19, pp. 5118–5134, 2002.

[74] A. A. Rashin and B. Honig, “Reevaluation of the Born model of ion hydration,” *The Journal of Physical Chemistry*, vol. 89, no. 26, pp. 5588–5593, 1985.

[75] E. Freisinger and R. K. O. Sigel, “From nucleotides to ribozymes – a comparison of their metal ion binding properties,” *Coordination Chemistry Reviews*, vol. 251, no. 13-14, pp. 1834–1851, 2007.

[76] J. Schnabl and R. K. O. Sigel, “Controlling ribozyme activity by metal ions,” *Current Opinion in Chemical Biology*, vol. 14, no. 2, pp. 269–275, 2010.

[77] M. Pechlaner and R. K. O. Sigel, “Characterization of metal ion-nucleic acid interactions in solution,” *Metal Ions in Life Sciences*, vol. 10, pp. 1–42, 2012.

[78] K. Juneau, E. Podell, D. J. Harrington, and T. R. Cech, “Structural basis of the enhanced stability of a mutant ribozyme domain and a detailed view of RNA–solvent interactions,” *Structure*, vol. 9, no. 3, pp. 221–231, 2001.

[79] J. Wang, “Inclusion of weak high-resolution X-ray data for improvement of a group II intron structure,” *Acta Crystallographica Section D Biological Crystallography*, vol. 66, no. 9, pp. 988–1000, 2010.

[80] S. S. Reid and J. A. Cowan, “Biostructural chemistry of magnesium ion: characterization of the weak binding sites on tRNAPhe(yeast). implications for conformational change and activity,” *Biochemistry*, vol. 29, no. 25, pp. 6025–6032, 1990.

[81] R. L. Gonzalez Jr and I. Tinoco Jr, “Solution structure and thermodynamics of a divalent metal ion binding site in an RNA pseudoknot,” *Journal of Molecular Biology*, vol. 289, no. 5, pp. 1267–1282, 1999.

[82] J. Noeske, H. Schwalbe, and J. Wöhnert, “Metal-ion binding and metal-ion induced folding of the adenine-sensing riboswitch aptamer domain,” *Nucleic Acids Research*, vol. 35, no. 15, pp. 5262–5273, 2007.

[83] M. M. T. Korth and R. K. O. Sigel, “Unusually high-affinity Mg^{2+} binding at the AU-rich sequence within the antiterminator hairpin of a Mg^{2+} riboswitch,” *Chemistry & Biodiversity*, vol. 9, no. 9, pp. 2035–2049, 2012.

[84] D. Leipply and D. E. Draper, “Evidence for a thermodynamically distinct Mg^{2+} ion associated with formation of an RNA tertiary structure,” *Journal of the American Chemical Society*, vol. 133, no. 34, pp. 13397–13405, 2011.

[85] M. J. Fedor, “The role of metal ions in RNA catalysis,” *Current Opinion in Structural Biology*, vol. 12, no. 3, pp. 289–295, 2002.

[86] K. M. Brooks and K. J. Hampel, “Rapid steps in the *glmS* ribozyme catalytic pathway: cation and ligand requirements,” *Biochemistry*, vol. 50, no. 13, pp. 2424–2433, 2011.

[87] N. G. Holm, “The significance of Mg in prebiotic geochemistry,” *Geobiology*, vol. 10, no. 4, pp. 269–279, 2012.

[88] G. E. Fox, “Origin and evolution of the ribosome,” *Cold Spring Harbor Perspectives in Biology*, vol. 2, no. 9, 2010.

[89] C. Hsiao and L. D. Williams, “A recurrent magnesium-binding motif provides a framework for the ribosomal peptidyl transferase center,” *Nucleic Acids Research*, vol. 37, no. 10, pp. 3134–3142, 2009.

[90] J. B. Murray, A. A. Seyhan, N. G. Walter, J. M. Burke, and W. G. Scott, “The hammerhead, hairpin and VS ribozymes are catalytically proficient in monovalent cations alone,” *Chemistry & Biology*, vol. 5, no. 10, pp. 587–595, 1998.

[91] M. Roychowdhury-Saha and D. H. Burke, "Extraordinary rates of transition metal ion-mediated ribozyme catalysis," *RNA*, vol. 12, no. 10, pp. 1846–1852, 2006.

[92] K. Salehi-Ashtiani, A. Lupták, A. Litovchick, and J. W. Szostak, "A genomewide search for ribozymes reveals an HDV-like sequence in the human CPEB3 gene," *Science*, vol. 313, no. 5794, pp. 1788 –1792, 2006.

[93] K. Klawuhn, J. A. Jansen, J. Souchek, G. A. Soukup, and J. K. Soukup, "Analysis of metal ion dependence in *glmS* ribozyme self-cleavage and coenzyme binding," *ChemBioChem*, vol. 11, no. 18, pp. 2567–2571, 2010.

[94] T. Pan and O. C. Uhlenbeck, "In vitro selection of RNAs that undergo autolytic cleavage with Pb^{2+}," *Biochemistry*, vol. 31, no. 16, pp. 3887–3895, 1992.

[95] S. Fusz, A. Eisenführ, S. G. Srivatsan, A. Heckel, and M. Famulok, "A ribozyme for the aldol reaction," *Chemistry & Biology*, vol. 12, no. 8, pp. 941–950, 2005.

[96] A. R. Ferré-D'Amaré and W. G. Scott, "Small self-cleaving ribozymes," *Cold Spring Harbor Perspectives in Biology*, vol. 2, no. 10, 2010.

[97] G. Bruening, "Replication of a plant virus satellite RNA: evidence favors transcription of circular templates of both polarities," *Molecular Plant-Microbe Interactions*, vol. 4, no. 3, p. 219, 1991.

[98] J. C. Kennell, B. J. Saville, S. Mohr, M. T. Kuiper, J. R. Sabourin, R. A. Collins, and A. M. Lambowitz, "The VS catalytic RNA replicates by reverse transcription as a satellite of a retroplasmid.," *Genes & Development*, vol. 9, no. 3, pp. 294–303, 1995.

[99] R. Flores, C. Hernandez, M. de la Peña, A. Vera, and J.-A. Daros, "Hammerhead ribozyme structure and function in plant RNA replication," *Methods in Enzymology*, vol. Volume 341, pp. 540–552, 2001.

[100] T. B. Macnaughton, Y. J. Wang, and M. M. Lai, "Replication of hepatitis delta virus RNA: effect of mutations of the autocatalytic cleavage sites," *Journal of Virology*, vol. 67, no. 4, pp. 2228–2234, 1993.

[101] K. S. Jeng, A. Daniel, and M. M. Lai, "A pseudoknot ribozyme structure is active in vivo and required for hepatitis delta virus RNA replication.," *Journal of Virology*, vol. 70, no. 4, pp. 2403–2410, 1996.

[102] A. D. Branch and H. D. Robertson, "A replication cycle for viroids and other small infectious RNA's," *Science*, vol. 223, no. 4635, pp. 450–455, 1984.

[103] G. A. Prody, J. T. Bakos, J. M. Buzayan, I. R. Schneider, and G. Bruening, "Autolytic processing of dimeric plant virus satellite RNA," *Science*, vol. 231, no. 4745, pp. 1577–1580, 1986.

[104] J. M. Buzayan, W. L. Gerlach, and G. Bruening, "Non-enzymatic cleavage and ligation of RNAs complementary to a plant virus satellite RNA," *Nature*, vol. 323, no. 6086, pp. 349–353, 1986.

[105] M. Martick and W. G. Scott, "Tertiary contacts distant from the active site prime a ribozyme for catalysis," *Cell*, vol. 126, no. 2, pp. 309–320, 2006.

[106] L. Sharmeen, M. Y. Kuo, G. Dinter-Gottlieb, and J. Taylor, "Antigenomic RNA of human hepatitis delta virus can undergo self-cleavage.," *Journal of Virology*, vol. 62, no. 8, pp. 2674–2679, 1988.

[107] A. T. Perrotta and M. D. Been, "A pseudoknot-like structure required for efficient self-cleavage of hepatitis delta virus RNA," *Nature*, vol. 350, no. 6317, pp. 434–436, 1991.

[108] C.-H. T. Webb and A. Lupták, "HDV-like self-cleaving ribozymes," *RNA Biology*, vol. 8, no. 5, pp. 719–727, 2011.

[109] C. Hammann, A. Luptak, J. Perreault, and M. d. l. Peña, "The ubiquitous hammerhead ribozyme," *RNA*, vol. 18, no. 5, pp. 871–885, 2012.

[110] P. B. Rupert and A. R. Ferré-D'Amaré, "Crystal structure of a hairpin ribozyme-inhibitor complex with implications for catalysis," *Nature*, vol. 410, no. 6830, pp. 780–786, 2001.

[111] B. J. Saville and R. A. Collins, "A site-specific self-cleavage reaction performed by a novel RNA in *Neurospora* mitochondria," *Cell*, vol. 61, no. 4, pp. 685–696, 1990.

[112] T. L. Beattie, J. E. Olive, and R. A. Collins, "A secondary-structure model for the self-cleaving region of *Neurospora* VS RNA," *Proceedings of the National Academy of Sciences*, vol. 92, no. 10, pp. 4686–4690, 1995.

[113] J. E. Barrick, K. A. Corbino, W. C. Winkler, A. Nahvi, M. Mandal, J. Collins, M. Lee, A. Roth, N. Sudarsan, I. Jona, J. K. Wickiser, and R. R. Breaker, "New RNA motifs suggest an expanded scope for riboswitches in bacterial genetic control," *Proceedings of the National Academy of Sciences of the United States of America*, vol. 101, no. 17, pp. 6421–6426, 2004.

[114] W. C. Winkler, A. Nahvi, A. Roth, J. A. Collins, and R. R. Breaker, "Control of gene expression by a natural metabolite-responsive ribozyme," *Nature*, vol. 428, no. 6980, pp. 281–286, 2004.

[115] A. Teixeira, A. Tahiri-Alaoui, S. West, B. Thomas, A. Ramadass, I. Martianov, M. Dye, W. James, N. J. Proudfoot, and A. Akoulitchev, "Autocatalytic RNA cleavage in the human β-globin pre-mRNA promotes transcription termination," *Nature*, vol. 432, no. 7016, pp. 526–530, 2004.

[116] A. Roth, Z. Weinberg, A. G. Y. Chen, P. B. Kim, T. D. Ames, and R. R. Breaker, “A widespread self-cleaving ribozyme class is revealed by bioinformatics,” *Nature Chemical Biology*, vol. 10, no. 1, pp. 56–60, 2014.

[117] C. Tuerk and L. Gold, “Systematic evolution of ligands by exponential enrichment: RNA ligands to bacteriophage T4 DNA polymerase,” *Science*, vol. 249, no. 4968, pp. 505–510, 1990.

[118] A. D. Ellington and J. W. Szostak, “In vitro selection of RNA molecules that bind specific ligands,” *Nature*, vol. 346, no. 6287, pp. 818–822, 1990.

[119] B. S. Singer, T. Shtatland, D. Brown, and L. Gold, “Libraries for genomic SELEX,” *Nucleic Acids Research*, vol. 25, no. 4, pp. 781–786, 1997.

[120] S. L. Daubendiek and E. T. Kool, “Generation of catalytic RNAs by rolling transcription of synthetic DNA nanocircles,” *Nature Biotechnology*, vol. 15, no. 3, pp. 273–277, 1997.

[121] S. K. Silverman, “*In vitro* selection, characterization, and application of deoxyribozymes that cleave RNA,” *Nucleic Acids Research*, vol. 33, no. 19, pp. 6151–6163, 2005.

[122] E. Rivas and S. R. Eddy, “Noncoding RNA gene detection using comparative sequence analysis,” *BMC Bioinformatics*, vol. 2, no. 1, p. 8, 2001.

[123] Z. Weinberg, J. E. Barrick, Z. Yao, A. Roth, J. N. Kim, J. Gore, J. X. Wang, E. R. Lee, K. F. Block, N. Sudarsan, S. Neph, M. Tompa, W. L. Ruzzo, and R. R. Breaker, “Identification of 22 candidate structured RNAs in bacteria using the CMfinder comparative genomics pipeline,” *Nucleic Acids Research*, vol. 35, no. 14, pp. 4809–4819, 2007.

[124] M. M. Meyer, T. D. Ames, D. P. Smith, Z. Weinberg, M. S. Schwalbach, S. J. Giovannoni, and R. R. Breaker, “Identification of candidate structured RNAs in the marine organism ’*Candidatus Pelagibacter ubique*’,” *BMC Genomics*, vol. 10, no. 1, p. 268, 2009.

[125] H. D. Robertson, S. Altman, and J. D. Smith, “Purification and properties of a specific *Escherichia coli* ribonuclease which cleaves a tyrosine transfer ribonucleic acid precursor,” *Journal of Biological Chemistry*, vol. 247, no. 16, pp. 5243–5251, 1972.

[126] S. C. Walker and D. R. Engelke, “Ribonuclease P: the evolution of an ancient RNA enzyme,” *Critical Reviews in Biochemistry and Molecular Biology*, vol. 41, no. 2, pp. 77–102, 2006.

[127] S. V. Lipchock and S. A. Strobel, “A relaxed active site after exon ligation by the group I intron,” *Proceedings of the National Academy of Sciences*, vol. 105, no. 15, pp. 5699–5704, 2008.

[128] R. van der Veen, A. Arnberg, G. van der Horst, L. Bonen, H. Tabak, and L. Grivell, “Excised group II introns in yeast mitochondria are lariats and can be formed by self-splicing in vitro,” *Cell*, vol. 44, no. 2, pp. 225–234, 1986.

[129] C. L. Peebles, P. S. Perlman, K. L. Mecklenburg, M. L. Petrillo, J. H. Tabor, K. A. Jarrell, and H. L. Cheng, “A self-splicing RNA excises an intron lariat,” *Cell*, vol. 44, no. 2, pp. 213–223, 1986.

[130] C. Schmelzer and R. J. Schweyen, “Self-splicing of group II introns in vitro: Mapping of the branch point and mutational inhibition of lariat formation,” *Cell*, vol. 46, no. 4, pp. 557–565, 1986.

[131] A. M. Lambowitz and S. Zimmerly, “Group II introns: Mobile ribozymes that invade DNA,” *Cold Spring Harbor Perspectives in Biology*, vol. 3, no. 8, 2011.

[132] E. J. Sontheimer, P. M. Gordon, and J. A. Piccirilli, “Metal ion catalysis during group II intron self-splicing: parallels with the spliceosome,” *Genes & Development*, vol. 13, no. 13, pp. 1729–1741, 1999.

[133] P. M. Gordon, E. J. Sontheimer, and J. A. Piccirilli, “Metal ion catalysis during the exon-ligation step of nuclear pre-mRNA splicing: extending the parallels between the spliceosome and group II introns,” *RNA*, vol. 6, no. 2, pp. 199–205, 2000.

[134] S. Valadkhan, A. Mohammadi, Y. Jaladat, and S. Geisler, “Protein-free small nuclear RNAs catalyze a two-step splicing reaction,” *Proceedings of the National Academy of Sciences of the United States of America*, vol. 106, no. 29, pp. 11901–11906, 2009.

[135] P. A. Sharp, “On the origin of RNA splicing and introns,” *Cell*, vol. 42, no. 2, pp. 397–400, 1985.

[136] T. R. Cech, “The generality of self-splicing RNA: relationship to nuclear mRNA splicing,” *Cell*, vol. 44, no. 2, pp. 207–210, 1986.

[137] S. E. Butcher, “The spliceosome as ribozyme hypothesis takes a second step,” *Proceedings of the National Academy of Sciences of the United States of America*, vol. 106, no. 30, pp. 12211–12212, 2009.

[138] I. B. Rogozin, L. Carmel, M. Csuros, and E. V. Koonin, “Origin and evolution of spliceosomal introns,” *Biology Direct*, vol. 7, p. 11, 2012.

[139] P. Nissen, J. Hansen, N. Ban, P. B. Moore, and T. A. Steitz, “The structural basis of ribosome activity in peptide bond synthesis,” *Science*, vol. 289, no. 5481, pp. 920–930, 2000.

[140] M. Simonović and T. A. Steitz, “A structural view on the mechanism of the ribosome-catalyzed peptide bond formation,” *Biochimica et Biophysica Acta (BBA) - Gene Regulatory Mechanisms*, vol. 1789, no. 9–10, pp. 612–623, 2009.

[141] K. Trappl and N. Polacek, “The ribosome: a molecular machine powered by RNA,” *Metal Ions in Life Sciences*, vol. 9, pp. 253–275, 2011.

[142] C. Guerrier-Takada, K. Haydock, L. Allen, and S. Altman, “Metal ion requirements and other aspects of the reaction catalyzed by M1 RNA, the RNA subunit of ribonuclease P from *Escherichia coli*,” *Biochemistry*, vol. 25, no. 7, pp. 1509–1515, 1986.

[143] D. Smith and N. R. Pace, “Multiple magnesium ions in the ribonuclease P reaction mechanism,” *Biochemistry*, vol. 32, no. 20, pp. 5273–5281, 1993.

[144] K. A. Jarrell, C. L. Peebles, R. C. Dietrich, S. L. Romiti, and P. S. Perlman, “Group II intron self-splicing. Alternative reaction conditions yield novel products.,” *Journal of Biological Chemistry*, vol. 263, no. 7, pp. 3432–3439, 1988.

[145] B. Ruskin, A. R. Krainer, T. Maniatis, and M. R. Green, “Excision of an intact intron as a novel lariat structure during pre-mRNA splicing in vitro,” *Cell*, vol. 38, no. 1, pp. 317–331, 1984.

[146] R. A. Padgett, M. M. Konarska, P. J. Grabowski, S. F. Hardy, and P. A. Sharp, “Lariat RNA’s as intermediates and products in the splicing of messenger RNA precursors,” *Science*, vol. 225, no. 4665, pp. 898–903, 1984.

[147] E. K. Y. Leung, N. Suslov, N. Tuttle, R. Sengupta, and J. A. Piccirilli, “The mechanism of peptidyl transfer catalysis by the ribosome,” *Annual Review of Biochemistry*, vol. 80, no. 1, pp. 527–555, 2011.

[148] A. Jäschke, “Artificial ribozymes and deoxyribozymes,” *Current Opinion in Structural Biology*, vol. 11, no. 3, pp. 321–326, 2001.

[149] A. Bax and S. Grzesiek, “Methodological advances in protein NMR,” *Accounts of Chemical Research*, vol. 26, no. 4, pp. 131–138, 1993.

[150] K. Pervushin, R. Riek, G. Wider, and K. Wüthrich, “Transverse relaxation-optimized spectroscopy (TROSY) for NMR studies of aromatic spin systems in ^{13}C-labeled proteins,” *Journal of the American Chemical Society*, vol. 120, no. 25, pp. 6394–6400, 1998.

[151] K. Pervushin, “Impact of transverse relaxation optimized spectroscopy (TROSY) on NMR as a technique in structural biology,” *Quarterly Reviews of Biophysics*, vol. 33, no. 02, pp. 161–197, 2000.

[152] R. Riek, “TROSY: transverse relaxation-optimized spectroscopy,” in *BioNMR in Drug Research* (O. Zerbe, ed.), pp. 227–241, Wiley-VCH Verlag GmbH & Co. KGaA, 2002.

[153] J. H. Prestegard, H. M. al Hashimi, and J. R. Tolman, “NMR structures of biomolecules using field oriented media and residual dipolar couplings,” *Quarterly Reviews of Biophysics*, vol. 33, no. 4, pp. 371–424, 2000.

[154] R. S. Lipsitz and N. Tjandra, “Residual dipolar couplings in NMR structure analysis,” *Annual Review of Biophysics and Biomolecular Structure*, vol. 33, no. 1, pp. 387–413, 2004.

[155] I. Kim, P. J. Lukavsky, and J. D. Puglisi, “NMR study of 100 kDa HCV IRES RNA using segmental isotope labeling,” *Journal of the American Chemical Society*, vol. 124, no. 32, pp. 9338–9339, 2002.

[156] O. Duss, C. Maris, C. von Schroetter, and F. H.-T. Allain, “A fast, efficient and sequence-independent method for flexible multiple segmental isotope labeling of RNA using ribozyme and RNase H cleavage,” *Nucleic Acids Research*, vol. 38, no. 20, p. e188, 2010.

[157] G. Varani, F. Aboul-ela, and F. H.-T. Allain, “NMR investigation of RNA structure,” *Progress in Nuclear Magnetic Resonance Spectroscopy*, vol. 29, no. 1-2, pp. 51–127, 1996.

[158] A. T. Brünger, P. D. Adams, G. M. Clore, W. L. DeLano, P. Gros, R. W. Grosse-Kunstleve, J. S. Jiang, J. Kuszewski, M. Nilges, N. S. Pannu, R. J. Read, L. M. Rice, T. Simonson, and G. L. Warren, “Crystallography & NMR system: A new software suite for macromolecular structure determination,” *Acta Crystallographica Section D Biological Crystallography*, vol. 54, no. 5, pp. 905–921, 1998.

[159] C. D. Schwieters, J. J. Kuszewski, N. Tjandra, and G. Marius Clore, “The Xplor-NIH NMR molecular structure determination package,” *Journal of Magnetic Resonance*, vol. 160, no. 1, pp. 65–73, 2003.

[160] C. D. Schwieters, J. J. Kuszewski, and G. Marius Clore, “Using Xplor–NIH for NMR molecular structure determination,” *Progress in Nuclear Magnetic Resonance Spectroscopy*, vol. 48, no. 1, pp. 47–62, 2006.

[161] A. J. Dingley and S. Grzesiek, “Direct observation of hydrogen bonds in nucleic acid base pairs by internucleotide $^2J_{NN}$ couplings,” *Journal of the American Chemical Society*, vol. 120, no. 33, pp. 8293–8297, 1998.

[162] H. Zhou, A. Vermeulen, F. M. Jucker, and A. Pardi, “Incorporating residual dipolar couplings into the NMR solution structure determination of nucleic acids,” *Biopolymers*, vol. 52, no. 4, pp. 168–180, 1999.

[163] A. L. Breeze, “Isotope-filtered NMR methods for the study of biomolecular structure and interactions,” *Progress in Nuclear Magnetic Resonance Spectroscopy*, vol. 36, no. 4, pp. 323–372, 2000.

[164] B. Ivarsson, U. Joensson, H. Sjoedin, S. Sjoelander, and R. Staahlberg, “Optical biosensor system,” 1990. IPC: G01N 21/17; G01N 33/53.

[165] U. Jönsson, L. Fägerstam, B. Ivarsson, B. Johnsson, R. Karlsson, K. Lundh, S. Löfås, B. Persson, H. Roos, and I. Rönnberg, "Real-time biospecific interaction analysis using surface plasmon resonance and a sensor chip technology," *BioTechniques*, vol. 11, no. 5, pp. 620–627, 1991.

[166] S. Zeng, D. Baillargeat, H.-P. Ho, and K.-T. Yong, "Nanomaterials enhanced surface plasmon resonance for biological and chemical sensing applications," *Chemical Society Reviews*, vol. 43, no. 10, pp. 3426–3452, 2014.

[167] H. Raether, *Surface plasmons on smooth and rough surfaces and on gratings.* Springer, 1988.

[168] A. Otto, "Excitation of nonradiative surface plasma waves in silver by the method of frustrated total reflection," *Zeitschrift für Physik*, vol. 216, no. 4, pp. 398–410, 1968.

[169] E. Kretschmann and H. Raether, "Radiative decay of nonradiative surface plasmons excited by light," *Zeitschrift für Naturforschung A*, vol. 23, p. 2135, 1968.

[170] R. Breslow and D. L. Huang, "Effects of metal ions, including Mg^{2+} and lanthanides, on the cleavage of ribonucleotides and RNA model compounds," *Proceedings of the National Academy of Sciences of the United States of America*, vol. 88, no. 10, pp. 4080–4083, 1991.

[171] N. G. Walter, N. Yang, and J. M. Burke, "Probing non-selective cation binding in the hairpin ribozyme with Tb(III)," *Journal of Molecular Biology*, vol. 298, no. 3, pp. 539–555, 2000.

[172] R. K. O. Sigel and A. M. Pyle, "Lanthanide ions as probes for metal ions in the structure and catalytic mechanism of ribozymes," *Metal Ions in Biological Systems*, vol. 40, pp. 477–512, 2003.

[173] G. Gish and F. Eckstein, "DNA and RNA sequence determination based on phosphorothioate chemistry," *Science*, vol. 240, no. 4858, pp. 1520–1522, 1988.

[174] R. K. Gaur and G. Krupp, "Modification interference approach to detect ribose moieties important for the optimal activity of a ribozyme," *Nucleic Acids Research*, vol. 21, no. 1, pp. 21–26, 1993.

[175] S. A. Strobel and K. Shetty, "Defining the chemical groups essential for *Tetrahymena* group I intron function by nucleotide analog interference mapping," *Proceedings of the National Academy of Sciences*, vol. 94, no. 7, pp. 2903–2908, 1997.

[176] M. Boudvillain and A. M. Pyle, "Defining functional groups, core structural features and inter-domain tertiary contacts essential for group II intron self-splicing: a NAIM analysis," *The EMBO Journal*, vol. 17, no. 23, pp. 7091–7104, 1998.

[177] J. K. Frederiksen, N.-S. Li, R. Das, D. Herschlag, and J. A. Piccirilli, "Metal-ion rescue revisited: Biochemical detection of site-bound metal ions important for RNA folding," *RNA*, vol. 18, no. 6, pp. 1123–1141, 2012.

[178] M. L. Gill, S. A. Strobel, and J. P. Loria, "^{205}Tl NMR methods for the characterization of monovalent cation binding to nucleic acids," *Journal of the American Chemical Society*, vol. 127, no. 47, pp. 16723–16732, 2005.

[179] S. Johannsen, N. Megger, D. Böhme, R. K. O. Sigel, and J. Müller, "Solution structure of a DNA double helix with consecutive metal-mediated base pairs," *Nature Chemistry*, vol. 2, no. 3, pp. 229–234, 2010.

[180] R. E. Hurd, E. Azhderian, and B. R. Reid, "Paramagnetic ion effects on the nuclear magnetic resonance spectrum of transfer ribonucleic acid: assignment of the 15-48 tertiary resonance," *Biochemistry*, vol. 18, no. 18, pp. 4012–4017, 1979.

[181] H. P. Hofmann, S. Limmer, V. Hornung, and M. Sprinzl, "Ni^{2+}-binding RNA motifs with an asymmetric purine-rich internal loop and a G-A base pair," *RNA*, vol. 3, no. 11, pp. 1289–1300, 1997.

[182] J. S. Kieft and I. Tinoco Jr, "Solution structure of a metal-binding site in the major groove of RNA complexed with cobalt (III) hexammine," *Structure*, vol. 5, no. 5, pp. 713–721, 1997.

[183] M. Rowińska-Żyrek, M. Skilandat, and R. K. O. Sigel, "Hexaamminecobalt(III) – probing metal ion binding sites in nucleic acids by NMR spectroscopy," *Zeitschrift für anorganische und allgemeine Chemie*, vol. 639, no. 8-9, pp. 1313–1320, 2013.

[184] J. Feigon, S. E. Butcher, L. D. Finger, and N. V. Hud, "Solution nuclear magnetic resonance probing of cation binding sites on nucleic acids," *Methods in Enzymology*, vol. 338, pp. 400–420, 2001.

[185] M. C. Erat and R. K. O. Sigel, "Determination of the intrinsic affinities of multiple site-specific Mg^{2+} ions coordinated to domain 6 of a group II intron ribozyme," *Inorganic Chemistry*, vol. 46, no. 26, pp. 11224–11234, 2007.

[186] M. C. Erat, H. Kovacs, and R. K. O. Sigel, "Metal ion-N7 coordination in a ribozyme branch domain by NMR," *Journal of Inorganic Biochemistry*, vol. 104, no. 5, pp. 611–613, 2010.

[187] S. Augustin, M. W. Müller, and R. J. Schweyen, "Reverse self-splicing of group II intron RNAs in vitro," *Nature*, vol. 343, no. 6256, pp. 383–386, 1990.

[188] M. Mörl, I. Niemer, and C. Schmelzer, "New reactions catalyzed by a group II intron ribozyme with RNA and DNA substrates," *Cell*, vol. 70, no. 5, pp. 803–810, 1992.

[189] B. Séraphin, G. Faye, D. Hatat, and C. Jacq, "The yeast mitochondrial intron aI5α: associated endonuclease activity and in vivo mobility," *Gene*, vol. 113, no. 1, pp. 1–8, 1992.

[190] J. Yang, S. Zimmerly, P. S. Perlman, and A. M. Lambowitz, "Efficient integration of an intron RNA into double-stranded DNA by reverse splicing," *Nature*, vol. 381, no. 6580, pp. 332–335, 1996.

[191] M. Matsuura, R. Saldanha, H. Ma, H. Wank, J. Yang, G. Mohr, S. Cavanagh, G. M. Dunny, M. Belfort, and A. M. Lambowitz, “A bacterial group II intron encoding reverse transcriptase, maturase, and DNA endonuclease activities: Biochemical demonstration of maturase activity and insertion of new genetic information within the intron,” *Genes & Development*, vol. 11, no. 21, pp. 2910–2924, 1997.

[192] R. Saldanha, B. Chen, H. Wank, M. Matsuura, J. Edwards, and A. M. Lambowitz, “RNA and protein catalysis in group II intron splicing and mobility reactions using purified components,” *Biochemistry*, vol. 38, no. 28, pp. 9069–9083, 1999.

[193] M. Curcio and M. Belfort, “Retrohoming: cDNA-mediated mobility of group II introns requires a catalytic RNA,” *Cell*, vol. 84, no. 1, pp. 9–12, 1996.

[194] T. Cavalier-Smith, “Intron phylogeny: a new hypothesis,” *Trends in Genetics*, vol. 7, no. 5, pp. 145–148, 1991.

[195] J. S. Mattick and M. J. Gagen, “The evolution of controlled multitasked gene networks: the role of introns and other noncoding RNAs in the development of complex organisms,” *Molecular Biology and Evolution*, vol. 18, no. 9, pp. 1611–1630, 2001.

[196] W. Martin and E. V. Koonin, “Introns and the origin of nucleus–cytosol compartmentalization,” *Nature*, vol. 440, no. 7080, pp. 41–45, 2006.

[197] F. Michel and J. Feral, “Structure and activities of group II introns,” *Annual Review of Biochemistry*, vol. 64, no. 1, pp. 435–461, 1995.

[198] A. Jacquier and F. Michel, “Multiple exon-binding sites in class II self-splicing introns,” *Cell*, vol. 50, no. 1, pp. 17–29, 1987.

[199] M. Costa, F. Michel, and E. Westhof, “A three-dimensional perspective on exon binding by a group II self-splicing intron,” *The EMBO Journal*, vol. 19, no. 18, pp. 5007–5018, 2000.

[200] A. de Lencastre, S. Hamill, and A. M. Pyle, “A single active-site region for a group II intron,” *Nature Structural & Molecular Biology*, vol. 12, no. 7, pp. 626–627, 2005.

[201] F. Michel, U. Kazuhiko, and O. Haruo, “Comparative and functional anatomy of group II catalytic introns – a review,” *Gene*, vol. 82, no. 1, pp. 5–30, 1989.

[202] P. Z. Qin and A. M. Pyle, “The architectural organization and mechanistic function of group II intron structural elements,” *Current Opinion in Structural Biology*, vol. 8, no. 3, pp. 301–308, 1998.

[203] Q. Xiang, P. Z. Qin, W. J. Michels, K. Freeland, and A. M. Pyle, “Sequence specificity of a group II intron ribozyme: Multiple mechanisms for promoting unusually high discrimination against mismatched targets,” *Biochemistry*, vol. 37, no. 11, pp. 3839–3849, 1998.

[204] P. Z. Qin and A. M. Pyle, "Antagonistic substrate binding by a group II intron ribozyme," *Journal of Molecular Biology*, vol. 291, no. 1, pp. 15–27, 1999.

[205] H. Guo, M. Karberg, M. Long, J. P. Jones, B. Sullenger, and A. M. Lambowitz, "Group II introns designed to insert into therapeutically relevant DNA target sites in human cells," *Science*, vol. 289, no. 5478, pp. 452–457, 2000.

[206] G. Mohr, D. Smith, M. Belfort, and A. M. Lambowitz, "Rules for DNA target-site recognition by a lactococcal group II intron enable retargeting of the intron to specific DNA sequences," *Genes & Development*, vol. 14, no. 5, pp. 559–573, 2000.

[207] J. Perutka, W. Wang, D. Goerlitz, and A. M. Lambowitz, "Use of computer-designed group II introns to disrupt *Escherichia coli* DExH/D-box protein and DNA helicase genes," *Journal of Molecular Biology*, vol. 336, no. 2, pp. 421–439, 2004.

[208] D. Kruschel and R. K. O. Sigel, "Divalent metal ions promote the formation of the 5'-splice site recognition complex in a self-splicing group II intron," *Journal of Inorganic Biochemistry*, vol. 102, no. 12, pp. 2147–2154, 2008.

[209] P. Z. Qin and A. M. Pyle, "Stopped-flow fluorescence spectroscopy of a group II intron ribozyme reveals that domain 1 is an independent folding unit with a requirement for specific Mg^{2+} ions in the tertiary structure," *Biochemistry*, vol. 36, no. 16, pp. 4718–4730, 1997.

[210] L. J. Su, C. Waldsich, and A. M. Pyle, "An obligate intermediate along the slow folding pathway of a group II intron ribozyme," *Nucleic Acids Research*, vol. 33, no. 21, pp. 6674–6687, 2005.

[211] A. M. Pyle, O. Fedorova, and C. Waldsich, "Folding of group II introns: a model system for large, multidomain RNAs?," *Trends in Biochemical Sciences*, vol. 32, no. 3, pp. 138–145, 2007.

[212] J. L. Koch, S. C. Boulanger, S. D. Dib-Hajj, S. K. Hebbar, and P. S. Perlman, "Group II introns deleted for multiple substructures retain self-splicing activity.," *Molecular and Cellular Biology*, vol. 12, no. 5, pp. 1950–1958, 1992.

[213] W. J. J. Michels and A. M. Pyle, "Conversion of a group II intron into a new multiple-turnover ribozyme that selectively cleaves oligonucleotides: elucidation of reaction mechanism and structure/function relationships," *Biochemistry*, vol. 34, no. 9, pp. 2965–2977, 1995.

[214] R. K. O. Sigel, "Group II intron ribozymes and metal ions – a delicate relationship," *European Journal of Inorganic Chemistry*, vol. 2005, no. 12, pp. 2281, 2281–2292, 2292, 2005.

[215] D. Donghi and J. Schnabl, "Multiple roles of metal ions in large ribozymes," *Metal Ions in Life Sciences*, vol. 9, pp. 197–234, 2011.

[216] J. F. Swisher, L. J. Su, M. Brenowitz, V. E. Anderson, and A. M. Pyle, "Productive folding to the native state by a group II intron ribozyme," *Journal of Molecular Biology*, vol. 315, no. 3, pp. 297–310, 2002.

[217] R. K. O. Sigel, A. Vaidya, and A. M. Pyle, "Metal ion binding sites in a group II intron core," *Nature Structural & Molecular Biology*, vol. 7, no. 12, pp. 1111–1116, 2000.

[218] M. C. Erat, O. Zerbe, T. Fox, and R. K. O. Sigel, "Solution structure of domain 6 from a self-splicing group II intron ribozyme: A Mg^{2+} binding site is located close to the stacked branch adenosine," *ChemBioChem*, vol. 8, no. 3, pp. 306–314, 2007.

[219] D. Donghi, M. Pechlaner, C. Finazzo, B. Knobloch, and R. K. O. Sigel, "The structural stabilization of the κ three-way junction by Mg(II) represents the first step in the folding of a group II intron," *Nucleic Acids Research*, vol. 41, no. 4, pp. 2489–2504, 2013.

[220] T. A. Steitz and J. A. Steitz, "A general two-metal-ion mechanism for catalytic RNA," *Proceedings of the National Academy of Sciences*, vol. 90, no. 14, pp. 6498 –6502, 1993.

[221] H. Sigel, "Mechanistic aspects of the metal ion promoted hydrolysis of nucleoside 5'-triphosphates (NTPs)," *Coordination Chemistry Reviews*, vol. 100, pp. 453–539, 1990.

[222] P. M. Gordon, R. Fong, and J. A. Piccirilli, "A second divalent metal ion in the group II intron reaction center," *Chemistry & Biology*, vol. 14, no. 6, pp. 607–612, 2007.

[223] N. Toor, K. Rajashankar, K. S. Keating, and A. M. Pyle, "Structural basis for exon recognition by a group II intron," *Nature Structural & Molecular Biology*, vol. 15, no. 11, pp. 1221–1222, 2008.

[224] G. Wiesenberger, M. Waldherr, and R. J. Schweyen, "The nuclear gene MRS2 is essential for the excision of group II introns from yeast mitochondrial transcripts in vivo.," *Journal of Biological Chemistry*, vol. 267, no. 10, pp. 6963–6969, 1992.

[225] J. Gregan, D. M. Bui, R. Pillich, M. Fink, G. Zsurka, and R. J. Schweyen, "The mitochondrial inner membrane protein Lpe10p, a homologue of Mrs2p, is essential for magnesium homeostasis and group II intron splicing in yeast," *Molecular & General Genetics*, vol. 264, no. 6, pp. 773–781, 2001.

[226] M. Mastroianni, K. Watanabe, T. B. White, F. Zhuang, J. Vernon, M. Matsuura, J. Wallingford, and A. M. Lambowitz, "Group II intron-based gene targeting reactions in eukaryotes," *PLoS ONE*, vol. 3, no. 9, 2008.

[227] D. M. Truong, D. J. Sidote, R. Russell, and A. M. Lambowitz, "Enhanced group II intron retrohoming in magnesium-deficient *Escherichia coli* via selection of mutations in the ribozyme core," *Proceedings of the National Academy of Sciences*, vol. 110, no. 40, pp. E3800–E3809, 2013.

[228] L. J. Su, P. Z. Qin, W. J. Michels, and A. M. Pyle, "Guiding ribozyme cleavage through motif recognition: the mechanism of cleavage site selection by a group II intron ribozyme," *Journal of Molecular Biology*, vol. 306, no. 4, pp. 655–668, 2001.

[229] M. C. Erat and R. K. O. Sigel, "Divalent metal ions tune the self-splicing reaction of the yeast mitochondrial group II intron *Sc*.ai5γ," *Journal of Biological Inorganic Chemistry*, vol. 13, no. 6, pp. 1025–1036, 2008.

[230] R. T. Chan, A. R. Robart, K. R. Rajashankar, A. M. Pyle, and N. Toor, "Crystal structure of a group II intron in the pre-catalytic state," *Nature Structural & Molecular Biology*, vol. 19, no. 5, pp. 555–557, 2012.

[231] M. Marcia and A. M. Pyle, "Visualizing group II intron catalysis through the stages of splicing," *Cell*, vol. 151, no. 3, pp. 497–507, 2012.

[232] J. F. Milligan and O. C. Uhlenbeck, "Synthesis of small RNAs using T7 RNA polymerase," *Methods in Enzymology*, vol. Volume 180, pp. 51–62, 1989.

[233] O. Y. Fedoroff, M. Salazar, and B. R. Reid, "Structure of a DNA:RNA hybrid duplex: Why RNase H does not cleave pure RNA," *Journal of Molecular Biology*, vol. 233, no. 3, pp. 509–523, 1993.

[234] N. C. Horton and B. C. Finzel, "The structure of an RNA/DNA hybrid: A substrate of the ribonuclease activity of HIV-1 reverse transcriptase," *Journal of Molecular Biology*, vol. 264, no. 3, pp. 521–533, 1996.

[235] Y. Xiong and M. Sundaralingam, "Crystal structure of a DNA·RNA hybrid duplex with a polypurine RNA r(gaagaagag) and a complementary polypyrimidine DNA d(CTCTTCTTC)," *Nucleic Acids Research*, vol. 28, no. 10, pp. 2171–2176, 2000.

[236] R. W. Roberts and D. M. Crothers, "Stability and properties of double and triple helices: dramatic effects of RNA or DNA backbone composition," *Science*, vol. 258, no. 5087, pp. 1463–1466, 1992.

[237] S. H. Hung, Q. Yu, D. M. Gray, and R. L. Ratliff, "Evidence from CD spectra that d(purine)·r(pyrimidine) and r(purine)·d(pyrimidine) hybrids are in different structural classes," *Nucleic Acids Research*, vol. 22, no. 20, pp. 4326–4334, 1994.

[238] C. W. Cross, J. S. Rice, and X. Gao, "Solution structure of an RNA·DNA hybrid duplex containing a 3'-thioformacetal linker and an RNA A-tract," *Biochemistry*, vol. 36, no. 14, pp. 4096–4107, 1997.

[239] P. C. Bradshaw and D. R. Pfeiffer, "Release of Ca^{2+} and Mg^{2+} from yeast mitochondria is stimulated by increased ionic strength," *BMC Biochemistry*, vol. 7, p. 4, 2006.

[240] R. D. Grubbs, "Intracellular magnesium and magnesium buffering," *BioMetals*, vol. 15, no. 3, pp. 251–259, 2002.

[241] K. J. Hampel, N. G. Walter, and J. M. Burke, “The solvent-protected core of the hairpin ribozyme–substrate complex,” *Biochemistry*, vol. 37, no. 42, pp. 14672–14682, 1998.

[242] J. C. Kurz and C. A. Fierke, “The affinity of magnesium binding sites in the *Bacillus subtilis* RNase P·Pre-tRNA complex is enhanced by the protein subunit,” *Biochemistry*, vol. 41, no. 30, pp. 9545–9558, 2002.

[243] F. H.-T. Allain and G. Varani, “Divalent metal ion binding to a conserved wobble pair defining the upstream site of cleavage of group I self-splicing introns,” *Nucleic Acids Research*, vol. 23, no. 3, pp. 341–350, 1995.

[244] M. C. Erat and R. K. O. Sigel, “Methods to detect and characterize metal ion binding sites in RNA,” *Metal Ions in Life Sciences*, vol. 9, pp. 37–100, 2011.

[245] H. Robinson and A. H.-J. Wang, “Neomycin, spermine and hexaamminecobalt(III) share common structural motifs in converting B- to A-DNA,” *Nucleic Acids Research*, vol. 24, no. 4, pp. 676–682, 1996.

[246] M. Costa and F. Michel, “Tight binding of the 5’ exon to domain I of a group II self-splicing intron requires completion of the intron active site,” *The EMBO Journal*, vol. 18, no. 4, pp. 1025–1037, 1999.

[247] K. B. Hall and L. W. McLaughlin, “Thermodynamic and structural properties of pentamer DNA·DNA, RNA·RNA and DNA·RNA duplexes of identical sequence,” *Biochemistry*, vol. 30, no. 44, pp. 10606–10613, 1991.

[248] L. Ratmeyer, R. Vinayak, Y. Y. Zhong, G. Zon, and W. D. Wilson, “Sequence specific thermodynamic and structural properties for DNA·RNA duplexes,” *Biochemistry*, vol. 33, no. 17, pp. 5298–5304, 1994.

[249] E. A. Lesnik and S. M. Freier, “Relative thermodynamic stability of DNA, RNA, and DNA:RNA hybrid duplexes: Relationship with base composition and structure,” *Biochemistry*, vol. 34, no. 34, pp. 10807–10815, 1995.

[250] Y. Bai, M. Greenfeld, K. J. Travers, V. B. Chu, J. Lipfert, S. Doniach, and D. Herschlag, “Quantitative and comprehensive decomposition of the ion atmosphere around nucleic acids,” *Journal of the American Chemical Society*, vol. 129, no. 48, pp. 14981–14988, 2007.

[251] J. Schnabl, P. Suter, and R. K. O. Sigel, “MINAS–a database of Metal Ions in Nucleic AcidS,” *Nucleic Acids Research*, vol. 40, no. D1, pp. D434–D438, 2012.

[252] A. Barrientos-Durán, I. Chillón, F. Martínez-Abarca, and N. Toro, “Exon sequence requirements for excision in vivo of the bacterial group II intron RmInt1,” *BMC Molecular Biology*, vol. 12, no. 1, p. 24, 2011.

[253] F. Zhuang, M. Karberg, J. Perutka, and A. M. Lambowitz, "EcI5, a group IIB intron with high retrohoming frequency: DNA target site recognition and use in gene targeting," *RNA*, vol. 15, no. 3, pp. 432 –449, 2009.

[254] M. Costa, E. L. Christian, and F. Michel, "Differential chemical probing of a group II self-splicing intron identifies bases involved in tertiary interactions and supports an alternative secondary structure model of domain V.," *RNA*, vol. 4, no. 9, pp. 1055–1068, 1998.

[255] D. A. Mills, L. L. McKay, and G. M. Dunny, "Splicing of a group II intron involved in the conjugative transfer of pRS01 in lactococci," *Journal of Bacteriology*, vol. 178, no. 12, pp. 3531–3538, 1996.

[256] M. Martick, L. H. Horan, H. F. Noller, and W. G. Scott, "A discontinuous hammerhead ribozyme embedded in a mammalian messenger RNA," *Nature*, vol. 454, no. 7206, pp. 899–902, 2008.

[257] M. de la Peña and I. García-Robles, "Intronic hammerhead ribozymes are ultraconserved in the human genome," *EMBO reports*, vol. 11, no. 9, pp. 711–716, 2010.

[258] R. Mendez and J. D. Richter, "Translational control by CPEB: a means to the end," *Nature Reviews Molecular Cell Biology*, vol. 2, no. 7, pp. 521–529, 2001.

[259] L. E. Hake and J. D. Richter, "CPEB is a specificity factor that mediates cytoplasmic polyadenylation during *Xenopus* oocyte maturation," *Cell*, vol. 79, no. 4, pp. 617–627, 1994.

[260] L. B. Christerson and D. M. McKearin, "*orb* is required for anteroposterior and dorsoventral patterning during *Drosophila* oogenesis.," *Genes & Development*, vol. 8, no. 5, pp. 614–628, 1994.

[261] V. Lantz, J. S. Chang, J. I. Horabin, D. Bopp, and P. Schedl, "The *Drosophila orb* RNA-binding protein is required for the formation of the egg chamber and establishment of polarity.," *Genes & Development*, vol. 8, no. 5, pp. 598–613, 1994.

[262] C. Luitjens, M. Gallegos, B. Kraemer, J. Kimble, and M. Wickens, "CPEB proteins control two key steps in spermatogenesis in *C. elegans*," *Genes & Development*, vol. 14, no. 20, pp. 2596–2609, 2000.

[263] J. C. Darnell and J. D. Richter, "Cytoplasmic RNA-Binding proteins and the control of complex brain function," *Cold Spring Harbor Perspectives in Biology*, vol. 4, no. 8, p. a012344, 2012.

[264] K. Keleman, S. Krüttner, M. Alenius, and B. J. Dickson, "Function of the *Drosophila* CPEB protein Orb2 in long-term courtship memory," *Nature Neuroscience*, vol. 10, no. 12, pp. 1587–1593, 2007.

[265] K. Si, S. Lindquist, and E. R. Kandel, "A neuronal isoform of the *Aplysia* CPEB has prion-like properties," *Cell*, vol. 115, no. 7, pp. 879–891, 2003.

[266] D. M. J. Lilley and F. Eckstein, *Ribozymes and RNA Catalysis*. Royal Society of Chemistry, 2008.

[267] C. Vogler, K. Spalek, A. Aerni, P. Demougin, A. Müller, K.-D. Huynh, A. Papassotiropoulos, and D. J.-F. de Quervain, "CPEB3 is associated with human episodic memory," *Frontiers in Behavioral Neuroscience*, vol. 3, 2009.

[268] D. M. Chadalavada, E. A. Gratton, and P. C. Bevilacqua, "The human HDV-like CPEB3 ribozyme is intrinsically fast-reacting," *Biochemistry*, vol. 49, no. 25, pp. 5321–5330, 2010.

[269] B. L. Golden, S. Hammes-Schiffer, P. R. Carey, and P. C. Bevilacqua, "An integrated picture of HDV ribozyme catalysis," in *Biophysics of RNA Folding* (R. Russell, ed.), no. 3 in Biophysics for the Life Sciences, pp. 135–167, Springer New York, 2013.

[270] S. Nakano, D. M. Chadalavada, and P. C. Bevilacqua, "General acid-base catalysis in the mechanism of a hepatitis delta virus ribozyme," *Science*, vol. 287, no. 5457, pp. 1493–1497, 2000.

[271] J.-H. Chen, R. Yajima, D. M. Chadalavada, E. Chase, P. C. Bevilacqua, and B. L. Golden, "A 1.9 å crystal structure of the HDV ribozyme precleavage suggests both lewis acid and general acid mechanisms contribute to phosphodiester cleavage," *Biochemistry*, vol. 49, no. 31, pp. 6508–6518, 2010.

[272] I. H. Shih and M. D. Been, "Involvement of a cytosine side chain in proton transfer in the rate-determining step of ribozyme self-cleavage," *Proceedings of the National Academy of Sciences*, vol. 98, no. 4, pp. 1489–1494, 2001.

[273] S. R. Das and J. A. Piccirilli, "General acid catalysis by the hepatitis delta virus ribozyme," *Nature Chemical Biology*, vol. 1, no. 1, pp. 45–52, 2005.

[274] A. T. Perrotta, T. S. Wadkins, and M. D. Been, "Chemical rescue, multiple ionizable groups, and general acid-base catalysis in the HDV genomic ribozyme," *RNA*, vol. 12, no. 7, pp. 1282–1291, 2006.

[275] S. Nakano, D. J. Proctor, and P. C. Bevilacqua, "Mechanistic characterization of the HDV genomic ribozyme: Assessing the catalytic and structural contributions of divalent metal ions within a multichannel reaction mechanism," *Biochemistry*, vol. 40, no. 40, pp. 12022–12038, 2001.

[276] B. Gong, J.-H. Chen, P. C. Bevilacqua, B. L. Golden, and P. R. Carey, "Competition between $Co(NH_3)_6{}^{3+}$ and inner sphere Mg^{2+} ions in the HDV ribozyme," *Biochemistry*, vol. 48, no. 50, pp. 11961–11970, 2009.

[277] T. S. Wadkins, A. T. Perrotta, A. R. Ferré-D'Amaré, J. A. Doudna, and M. D. Been, "A nested double pseudoknot is required for self-cleavage activity of both the genomic and antigenomic hepatitis delta virus ribozymes.," *RNA*, vol. 5, no. 6, pp. 720–727, 1999.

[278] M. V. Krasovska, J. Sefcikova, N. Špačková, J. Šponer, and N. G. Walter, “Structural dynamics of precursor and product of the RNA enzyme from the hepatitis delta virus as revealed by molecular dynamics simulations,” *Journal of Molecular Biology*, vol. 351, no. 4, pp. 731–748, 2005.

[279] N. Veeraraghavan, A. Ganguly, J.-H. Chen, P. C. Bevilacqua, S. Hammes-Schiffer, and B. L. Golden, “Metal binding motif in the active site of the HDV ribozyme binds divalent and monovalent ions,” *Biochemistry*, vol. 50, no. 13, pp. 2672–2682, 2011.

[280] N. J. Riccitelli, E. Delwart, and A. Lupták, “Identification of minimal HDV-like ribozymes with unique divalent metal ion dependence in the human microbiome,” *Biochemistry*, vol. 53, no. 10, pp. 1616–1626, 2014.

[281] N. S. Prabhu, G. Dinter-Gottlieb, and P. A. Gottlieb, “Single substitutions of phosphorothioates in the HDV ribozyme G73 define regions necessary for optimal self-cleaving activity,” *Nucleic Acids Research*, vol. 25, no. 24, pp. 5119–5124, 1997.

[282] C.-H. T. Webb, N. J. Riccitelli, D. J. Ruminski, and A. Lupták, “Widespread occurrence of self-cleaving ribozymes,” *Science*, vol. 326, no. 5955, p. 953, 2009.

[283] D. S. Wilson and J. W. Szostak, “In vitro selection of functional nucleic acids,” *Annual Review of Biochemistry*, vol. 68, no. 1, pp. 611–647, 1999.

[284] A. Nehdi and J.-P. Perreault, “Unbiased in vitro selection reveals the unique character of the self-cleaving antigenomic HDV RNA sequence,” *Nucleic Acids Research*, vol. 34, no. 2, pp. 584–592, 2006.

[285] H. Karimata, S. Nakano, and N. Sugimoto, “The roles of cosolutes on the hammerhead ribozyme activity,” *Nucleic Acids Symposium Series*, vol. 50, no. 1, pp. 81–82, 2006.

[286] D. Kilburn, J. H. Roh, L. Guo, R. M. Briber, and S. A. Woodson, “Molecular crowding stabilizes folded RNA structure by the excluded volume effect,” *Journal of the American Chemical Society*, vol. 132, no. 25, pp. 8690–8696, 2010.

[287] R. Desai, D. Kilburn, H.-T. Lee, and S. A. Woodson, “Increased ribozyme activity in crowded solutions,” *Journal of Biological Chemistry*, vol. 289, no. 5, pp. 2972–2977, 2013.

[288] C. F. G. C. Geraldes and C. Luchinat, “Lanthanides as shift and relaxation agents in elucidating the structure of proteins and nucleic acids,” *Metal Ions in Biological Systems*, vol. 40, pp. 513–588, 2003.

[289] H. A. Heus and A. Pardi, “Structural features that give rise to the unusual stability of RNA hairpins containing GNRA loops,” *Science*, vol. 253, no. 5016, pp. 191–194, 1991.

[290] A. A. Szewczak, P. B. Moore, Y. L. Chang, and I. G. Wool, "The conformation of the sarcin/ricin loop from 28S ribosomal RNA," *Proceedings of the National Academy of Sciences*, vol. 90, no. 20, pp. 9581–9585, 1993.

[291] M. Orita, F. Nishikawa, T. Shimayama, K. Taira, Y. Endo, and S. Nishikawa, "High-resolution NMR study of a synthetic oligoribonucleotide with a tetranucleotide GAGA loop that is a substrate for the cytotoxic protein, ricin," *Nucleic Acids Research*, vol. 21, no. 24, pp. 5670–5678, 1993.

[292] A. Ke, K. Zhou, F. Ding, J. H. D. Cate, and J. A. Doudna, "A conformational switch controls hepatitis delta virus ribozyme catalysis," *Nature*, vol. 429, no. 6988, pp. 201–205, 2004.

[293] M. D. Been and G. S. Wickham, "Self-cleaving ribozymes of hepatitis delta virus RNA," *European Journal of Biochemistry*, vol. 247, no. 3, pp. 741–753, 1997.

[294] R. Thapar, A. P. Denmon, and E. P. Nikonowicz, "Recognition modes of RNA tetraloops and tetraloop-like motifs by RNA-binding proteins," *Wiley Interdisciplinary Reviews: RNA*, vol. 5, no. 1, pp. 49–67, 2014.

[295] H. Wu, P. K. Yang, S. E. Butcher, S. Kang, G. Chanfreau, and J. Feigon, "A novel family of RNA tetraloop structure forms the recognition site for *Saccharomyces cerevisiae* RNase III," *The EMBO Journal*, vol. 20, no. 24, pp. 7240–7249, 2001.

[296] F. H.-T. Allain and G. Varani, "Structure of the P1 helix from group I self-splicing introns," *Journal of Molecular Biology*, vol. 250, no. 3, pp. 333–353, 1995.

[297] F. M. Jucker, H. A. Heus, P. F. Yip, E. H. Moors, and A. Pardi, "A network of heterogeneous hydrogen bonds in GNRA tetraloops," *Journal of Molecular Biology*, vol. 264, no. 5, pp. 968–980, 1996.

[298] S. Rüdisser and I. Tinoco Jr, "Solution structure of cobalt(III)hexammine complexed to the GAAA tetraloop, and metal-ion binding to G·A mismatches," *Journal of Molecular Biology*, vol. 295, no. 5, pp. 1211–1223, 2000.

[299] M. Maderia, T. E. Horton, and V. J. DeRose, "Metal interactions with a GAAA RNA tetraloop characterized by ^{31}P NMR and phosphorothioate substitutions," *Biochemistry*, vol. 39, no. 28, pp. 8193–8200, 2000.

[300] H. Sigel, E. M. Bianchi, N. A. Corfù, Y. Kinjo, R. Tribolet, and R. B. Martin, "Stabilities and isomeric equilibria in solutions of monomeric metal-ion complexes of guanosine 5'-triphosphate (GTP4-) and inosine 5'-triphosphate (ITP4-) in comparison with those of adenosine 5'-triphosphate (ATP4-)," *Chemistry - A European Journal*, vol. 7, no. 17, pp. 3729–3737, 2001.

[301] H. Sigel and R. Griesser, "Nucleoside 5'-triphosphates: self-association, acid-base, and metal ion-binding properties in solution," *Chemical Society Reviews*, vol. 34, no. 10, pp. 875–900, 2005.

[302] J. A. Cowan, "Metallobiochemistry of RNA. $Co(NH_3)_6^{3+}$ as a probe for $Mg^{2+}(aq)$ binding sites," *Journal of Inorganic Biochemistry*, vol. 49, no. 3, pp. 171–175, 1993.

[303] M. S. Kayne and M. Cohn, "Enhancement of terbium(III) and europium(III) fluorescence in complexes with *Escherichia coli* tRNA," *Biochemistry*, vol. 13, no. 20, pp. 4159–4165, 1974.

[304] J. M. Wolfson and D. R. Kearns, "Europium as a fluorescent probe of transfer RNA structure," *Biochemistry*, vol. 14, no. 7, pp. 1436–1444, 1975.

[305] J. Ciesiołka, T. Marciniec, and W. J. Krzyżosiak, "Probing the environment of lanthanide binding sites in yeast tRNAPhe by specific metal-ion-promoted cleavages," *European Journal of Biochemistry*, vol. 182, no. 2, pp. 445–450, 1989.

[306] W. D. Horrocks, G. F. Schmidt, D. R. Sudnick, C. Kittrell, and R. A. Bernheim, "Laser-induced lanthanide ion luminescence lifetime measurements by direct excitation of metal ion levels. A new class of structural probe for calcium-binding proteins and nucleic acids," *Journal of the American Chemical Society*, vol. 99, no. 7, pp. 2378–2380, 1977.

[307] M. R. Hargittai and K. Musier-Forsyth, "Use of terbium as a probe of tRNA tertiary structure and folding," *RNA*, vol. 6, no. 11, pp. 1672–1680, 2000.

[308] G. A. Soukup and R. R. Breaker, "Relationship between internucleotide linkage geometry and the stability of RNA," *RNA*, vol. 5, no. 10, pp. 1308–1325, 1999.

[309] D. Leipply, D. Lambert, and D. E. Draper, "Ion-RNA interactions thermodynamic analysis of the effects of mono- and divalent ions on RNA conformational equilibria," *Methods in Enzymology*, vol. 469, pp. 433–463, 2009.

[310] S. Johannsen, S. Paulus, N. Düpre, J. Müller, and R. K. O. Sigel, "Using *in vitro* transcription to construct scaffolds for one-dimensional arrays of mercuric ions," *Journal of Inorganic Biochemistry*, vol. 102, no. 5-6, pp. 1141–1151, 2008.

[311] W. Eimer, J. R. Williamson, S. G. Boxer, and R. Pecora, "Characterization of the overall and internal dynamics of short oligonucleotides by depolarized dynamic light scattering and NMR relaxation measurements," *Biochemistry*, vol. 29, no. 3, pp. 799–811, 1990.

[312] J. Lapham, J. P. Rife, P. B. Moore, and D. M. Crothers, "Measurement of diffusion constants for nucleic acids by NMR," *Journal of Biomolecular NMR*, vol. 10, no. 3, pp. 255–262, 1997.

[313] C. A. Strulson, N. H. Yennawar, R. P. Rambo, and P. C. Bevilacqua, "Molecular crowding favors reactivity of a human ribozyme under physiological ionic conditions," *Biochemistry*, vol. 52, no. 46, pp. 8187–8197, 2013.

[314] D. M. Chadalavada, S. E. Senchak, and P. C. Bevilacqua, "The folding pathway of the genomic hepatitis delta virus ribozyme is dominated by slow folding of the pseudoknots," *Journal of Molecular Biology*, vol. 317, no. 4, pp. 559–575, 2002.

[315] T. S. Brown, D. M. Chadalavada, and P. C. Bevilacqua, "Design of a highly reactive HDV ribozyme sequence uncovers facilitation of RNA folding by alternative pairings and physiological ionic strength," *Journal of Molecular Biology*, vol. 341, no. 3, pp. 695–712, 2004.

[316] N. Veeraraghavan, A. Ganguly, B. L. Golden, P. C. Bevilacqua, and S. Hammes-Schiffer, "Mechanistic strategies in the HDV ribozyme: Chelated and diffuse metal ion interactions and active site protonation," *Journal of Physical Chemistry B*, vol. 115, no. 25, pp. 8346–8357, 2011.

[317] R. Das, K. J. Travers, Y. Bai, and D. Herschlag, "Determining the Mg^{2+} stoichiometry for folding an RNA metal ion core," *Journal of the American Chemical Society*, vol. 127, no. 23, pp. 8272–8273, 2005.

[318] S. P. Rosenstein and M. D. Been, "Self-cleavage of hepatitis delta virus genomic strand RNA is enhanced under partially denaturing conditions," *Biochemistry*, vol. 29, no. 35, pp. 8011–8016, 1990.

[319] J. B. Smith and G. Dinter-Gottlieb, "Antigenomic hepatitis delta virus ribozymes self-cleave in 18 M formamide," *Nucleic Acids Research*, vol. 19, no. 6, pp. 1285–1289, 1991.

[320] R. L. Seipelt, B. Zheng, A. Asuru, and B. C. Rymond, "U1 snRNA is cleaved by RNase III and processed through an Sm site-dependent pathway," *Nucleic Acids Research*, vol. 27, no. 2, pp. 587–595, 1999.

[321] G. Chanfreau, M. Buckle, and A. Jacquier, "Recognition of a conserved class of RNA tetraloops by *Saccharomyces cerevisiae* RNase III," *Proceedings of the National Academy of Sciences*, vol. 97, no. 7, pp. 3142–3147, 2000.

[322] I. Lebars, B. Lamontagne, S. Yoshizawa, S. A. Elela, and D. Fourmy, "Solution structure of conserved AGNN tetraloops: insights into Rnt1p RNA processing," *The EMBO Journal*, vol. 20, no. 24, pp. 7250–7258, 2001.

[323] H. Wu, A. Henras, G. Chanfreau, and J. Feigon, "Structural basis for recognition of the AGNN tetraloop RNA fold by the double-stranded RNA-binding domain of Rnt1p RNase III," *Proceedings of the National Academy of Sciences of the United States of America*, vol. 101, no. 22, pp. 8307–8312, 2004.

[324] F. C. Girard, O. M. Ottink, K. A. M. Ampt, M. Tessari, and S. S. Wijmenga, "Thermodynamics and NMR studies on duck, heron and human HBV encapsidation signals," *Nucleic Acids Research*, vol. 35, no. 8, pp. 2800–2811, 2007.

[325] M. Nassal and H. Schaller, "Hepatitis B virus replication – an update," *Journal of Viral Hepatitis*, vol. 3, no. 5, pp. 217–226, 1996.

[326] S. Gallo, M. Furler, and R. K. O. Sigel, "In vitro transcription and purification of RNAs of different size," *CHIMIA International Journal for Chemistry*, vol. 59, no. 11, pp. 812–816, 2005.

[327] P. K. Glasoe and F. A. Long, "Use of glass electrodes to measure acidities in deuterium oxide," *The Journal of Physical Chemistry*, vol. 64, no. 1, pp. 188–190, 1960.

[328] J. L. Markley, A. Bax, Y. Arata, C. W. Hilbers, R. Kaptein, B. D. Sykes, P. E. Wright, and K. Wüthrich, "Recommendations for the presentation of NMR structures of proteins and nucleic acids. IUPAC-IUBMB-IUPAB inter-union task group on the standardization of data bases of protein and nucleic acid structures determined by NMR spectroscopy," *Journal of Biomolecular NMR*, vol. 12, no. 1, pp. 1–23, 1998.

[329] N. Tjandra and A. Bax, "Measurement of dipolar contributions to $^1J_{CH}$ splittings from magnetic-field dependence of J modulation in two-dimensional NMR spectra," *Journal of Magnetic Resonance*, vol. 124, no. 2, pp. 512–515, 1997.

[330] W. F. Vranken, W. Boucher, T. J. Stevens, R. H. Fogh, A. Pajon, M. Llinas, E. L. Ulrich, J. L. Markley, J. Ionides, and E. D. Laue, "The CCPN data model for NMR spectroscopy: Development of a software pipeline," *Proteins: Structure, Function, and Bioinformatics*, vol. 59, no. 4, pp. 687–696, 2005.

[331] P. Güntert, C. Mumenthaler, and K. Wüthrich, "Torsion angle dynamics for NMR structure calculation with the new program DYANA," *Journal of Molecular Biology*, vol. 273, no. 1, pp. 283–298, 1997.

[332] A. T. Brunger, "Version 1.2 of the crystallography and NMR system," *Nature Protocols*, vol. 2, no. 11, pp. 2728–2733, 2007.

[333] M. Zweckstetter, "NMR: prediction of molecular alignment from structure using the PALES software," *Nature Protocols*, vol. 3, no. 4, pp. 679–690, 2008.

[334] G. M. Clore, A. M. Gronenborn, and N. Tjandra, "Direct structure refinement against residual dipolar couplings in the presence of rhombicity of unknown magnitude," *Journal of Magnetic Resonance*, vol. 131, no. 1, pp. 159–162, 1998.

[335] R. Koradi, M. Billeter, and K. Wüthrich, "MOLMOL: a program for display and analysis of macromolecular structures," *Journal of Molecular Graphics*, vol. 14, no. 1, pp. 51–55, 1996.

[336] T. J. Dolinsky, J. E. Nielsen, J. A. McCammon, and N. A. Baker, "PDB2PQR: an automated pipeline for the setup of Poisson-Boltzmann electrostatics calculations," *Nucleic Acids Research*, vol. 32, no. Web Server, pp. W665–W667, 2004.

[337] T. J. Dolinsky, P. Czodrowski, H. Li, J. E. Nielsen, J. H. Jensen, G. Klebe, and N. A. Baker, “PDB2PQR: expanding and upgrading automated preparation of biomolecular structures for molecular simulations,” *Nucleic Acids Research*, vol. 35, no. Web Server, pp. W522–W525, 2007.

[338] X.-J. Lu and W. K. Olson, “3DNA: a software package for the analysis, rebuilding and visualization of three-dimensional nucleic acid structures,” *Nucleic Acids Research*, vol. 31, no. 17, pp. 5108–5121, 2003.

[339] G. Zheng, X.-J. Lu, and W. K. Olson, “Web 3DNA – a web server for the analysis, reconstruction, and visualization of three-dimensional nucleic-acid structures,” *Nucleic Acids Research*, vol. 37, no. Web Server, pp. W240–W246, 2009.

[340] D. A. Harris and N. G. Walter, “Probing RNA structure and metal-binding sites using terbium(III) footprinting,” in *Current Protocols in Nucleic Acid Chemistry*, John Wiley & Sons, Inc., 2001.

[341] R. Römer and R. Hach, “tRNA conformation and magnesium binding,” *European Journal of Biochemistry*, vol. 55, no. 1, pp. 271–284, 1975.

[342] D. Grilley, A. M. Soto, and D. E. Draper, “Direct quantitation of Mg^{2+}–RNA interactions by use of a fluorescent dye,” *Methods in Enzymology*, vol. Volume 455, pp. 71–94, 2009.

[343] M. Bina-Stein and A. Stein, “Allosteric interpretation of Mg^{2+} ion binding to the denaturable *Escherichia coli* tRNAGlu2,” *Biochemistry*, vol. 15, no. 18, pp. 3912–3917, 1976.

Curriculum Vitae

Personal data

Name	Miriam Skilandat
Date of Birth	1985/02/17
Place of Birth	Berlin, Germany
Nationality	German

Education

1997 - 2004	high school education at Immanuel Kant Gymansium, Berlin, Germany
2004 - 2007	B. Sc. studies in Molecular Life Science (grade 1.6) at the University of Lübeck, Germany; thesis: “Optimisation of isotope-labelling and purification of recombinant ubiquitin for NMR-spectroscopy” in the group of Prof. Thomas Peters
2007-2008	studies in the M. Sc. programme “Systems Biology of Brains and Behaviour” University of Bielefeld, Germany
2008-2010	M. Sc. studies In Molecular Life Science (grade 1.1) at the University of Lübeck, Germany; thesis: “Single-molecule fluorescence studies on conformational flexibility of adrenodoxin reductase” in the group of Prof. Christian Hübner
2010-2014	PhD studies in the group of Prof. Roland Sigel, University of Zurich, Switzerland. Joined the program “Biomolecular Structure and Mechanism” of the Life Science Zurich Graduate School

Practical Experience and Teaching

2005	teaching assistant in the laboratory course ’chemistry for medical students’ at the University of Lübeck
2007	teaching assistant in the laboratory course ’physics: radioactivity’ and laboratory assistant at the Institute of Chemistry, University of Lübeck

2008	eight-week internship in the Molecular Biophysics group, Humboldt Universität Berlin, Germany conducting fluorescence studies on the interaction of alpha-synuclein with large unilamellar vesicles
2009	twelve-week internship in the SWITCH laboratory, Vrije Universiteit Brussel, Belgium working on prediction algorithms of amyloidogenic peptide sequences in proteins
2011	attended the FEBS Advanced Course "Chemistry of metals in biological systems" in Louvain-la-Neuve; Belgium
2011	teaching assistant at the laboratory course for general chemistry for biology and biochemistry students, University of Zurich
2012	attended the EMBO Practical Course Course "Multidimensional NMR in structural biology" in Joachimsthal, Germany
2012	teaching assistant at the laboratory course in general chemistry for biology and biochemistry students, University of Zurich
2013	attended the EMBO Practical Course Course "Structure determination of biological macromolecules by solution NMR" in Basel, Switzerland
2013	teaching assistant at the laboratory course for general chemistry for biology and biochemistry students, University of Zurich

Awards and Honors

award for the best graduation in the class of 2004, Immanuel Kant Gymnasium
award for best M. Sc. graduation of the year 2010, University of Lübeck
poster prize at the Dorothy Crowfoot Hodgkin symposium, University of Zurich
1st poster prize at the ISABC 2011 conference, Barcelona

Publications

M. Skilandat, R. K. O. Sigel, Ribozymes. Brenner's Online Encyclopedia of Genetics 2E, S. Maloy and K. Hughes (eds.), Academic Press, 254-258, 2013

R. K. O. Sigel, M. Skilandat, A. Sigel, B. P. Operschall and H. Sigel, Complex formation of cadmium with sugar residues, nucleobases, phosphates, nucleotides, and nucleic acids. *Metal Ions in Life Sciences*, vol. 11, pp. 191-274, 2013

M. Rowińska-Żyrek, M. Skilandat, R.K.O. Sigel, Hexaamminecobalt(III) – Probing metal ion binding sites in nucleic acids by NMR, *Zeitschrift für anorganische und allgemeine Chemie*, vol. 639, pp. 1313-1320, 2013

D. Kruschel, M. Skilandat, R. K. O. Sigel, NMR structure of the 5' splice site in the group IIB intron *Sc.*ai5γ – conformational requirements for exon–intron recognition. *RNA*, vol. 3, pp. 295-307, 2014

M. Skilandat & M. Rowińska-Żyrek, R. K. O. Sigel, Solution structure and metal ion binding sites of the human CPEB3 ribozyme's P4 domain, *Journal of Biological Inorganic Chemistry*, 2014, vol. 19, pp. 903-912
M. Skilandat, R. K. O. Sigel, The Role of Magnesium(II) for DNA cleavage site recognition in group II intron ribozymes – solution structure and metal ion binding sites of the RNA·DNA complex. *Journal of Biological Chemistry*, 2014, vol. 289, pp. 20650-20663

Invited talks & talks at scientific meetings

M. Skilandat, R. K. O. Sigel, "RNA-DNA contact formation in group II intron retrohoming – solution structure and role of metal ions." Institute of Physics, University of Lübeck, Lübeck, Jun. 7, 2012
M. Skilandat, D. Kruschel, R. K. O. Sigel, "Structural studies on RNA- and DNA-cleavage site formation in group II intron ribozymes" Swiss NMR Symposium, Basel, Jan. 14, 2014

Posters at scientific meetings

M. Skilandat, D. Kruschel, R. K. O. Sigel, "Structural studies on splice site formation during group II intron retrohoming" *Fall Meeting of the Swiss Chemical Society*, Lausanne, Sep. 9, 2011
M. Skilandat, R. K. O. Sigel, "Solution structure and metal ion-binding properties of the 5' splice site in group II intron retrohoming" *International Symposium of Applied Bioinorganic Chemistry (ISABC)*, Barcelona, Dec. 2-5, 2012
M. Skilandat, R. K. O. Sigel, "The reverse splice site in group II intron retrohoming: Solution structure and metal ion binding properties" *Swiss RNA Workshop*, Bern, Feb. 3, 2012
M. Skilandat, R. K. O. Sigel, "Splice site formation in group II intron retrohoming: solution structure and metal ion binding" International *Conference on Magnetic Resonance in Biological Systems (ICMRBSXXV)*, Lyon, Aug. 19-24, 2012
M. Skilandat, R. K. O. Sigel, "Formation of the reverse splice site in group II intron retrohoming" *Fall Meeting of the Swiss Chemical Society*, Zurich, Sep. 13, 2012
M. Skilandat, M. & Rowińska-Żyrek, R. K. O. Sigel, "The influence of metal-ions on the structure of the CPEB3 ribozyme's P4 region" *RNA society meeting, Davos*, Jun. 11-16, 2013
M. Skilandat, M. & Rowińska-Żyrek, R. K. O. Sigel, "First insight into the structure and metal-ion binding sites of the human CPEB3 ribozyme" *Fall Meeting of the Swiss Chemical Society*, Lausanne, Sep. 6, 2013